Predictive modelling of bifacial PV plants performance and diagnostic

Francisco Araya Rojas

THÈSE

Pour obtenir le grade de

DOCTEUR DE L'UNIVERSITÉ GRENOBLE ALPES

Spécialité : GENIE ELECTRIQUE

Arrêté ministériel : 25 mai 2016

Présentée par

Francisco ARAYA ROJAS

Thèse dirigée par **Quoc Tuan TRAN**,Professeur, Université Grenoble Alpes
et co-encadrée par **Hervé COLIN**, CEA-INES

préparée au sein du **Laboratoire CEA/LITEN**
dans **l'École Doctorale Electronique, Electrotechnique, Automatique, Traitement du Signal (EEATS)**

Modélisation prédictive des performances de centrales PV bifaciales et diagnostic

Predictive modelling of bifacial PV plants performance and diagnostic

Thèse soutenue publiquement le **20 juin 2022**,
devant le jury composé de :

Monsieur Quoc Tuan TRAN
PROFESSEUR, Université Grenoble Alpes, Directeur de thèse
Monsieur Bruno François
PROFESSEUR, Ecole Centrale de Lille, Rapporteur
Monsieur Mohamed BENBOUZID
PROFESSEUR, Université de Bretagne Occidentale, Rapporteur
Monsieur Yahia BAGHZOUZ
PROFESSEUR, University of Nevada, Las Vegas, USA, Examinateur
Monsieur Yvon BESANGER
PROFESSEUR, G2Elab, Grenoble-INP, UGA, président

" Pour ce qui est de l'avenir, il ne s'agit pas de le prévoir, mais de le rendre possible. "– Antoine de Saint Exupéry, Citadelle, 1948.

Abstract

In spite of a continuous decrease of the cost of photovoltaic cells and modules over the last decades, the PV industry keeps on trying to be more innovative in terms of implementing new cell concepts to improve the efficiency and the productivity. This boosted the development of the bifacial technology while maintaining a low cost of implementation in production lines, previously dedicated to monofacial modules only. Given the ability to produce energy from both sides and a lower thermal coefficient due to the utilization of new topologies for solar cells structure, the implementation of this technology has become bankable and has achieved market prices similar to their monofacial counterparts and is expected to have a significant impact on reducing the cost of solar energy. A bifacial module allows to increase the energy produced normalized to an equivalent monofacial power system by 10 to 20% depending on the configuration.

The bifacial gain is provided by the backside irradiance, whose magnitude depends on many system installation factors unlike monofacial systems. Therefore, in the last years there has been a great interest in developing models to simulate the performance of bifacial systems. However, unlike the well-established models for monofacial modules, the validation of bifacial models remains an ongoing task for the research centers collaborating with the PV industry in order to reduce the uncertainty and increase the reliability of the predictions. Increased uncertainty in the reliability of performance predictions indeed leads to reduced investor confidence in the profitability of the bifacial PV technology, making it difficult to finance and deploy large-scale bifacial PV systems. For this reason, further validation of these simulation models based on long-term field data acquired by monitoring systems in different geographical locations and with different geometrical configurations are necessary to overcome the aforementioned challenges.

The present work proposes the implementation of a comprehensive and proven simulation methodology for the prediction of the energy yield of bifacial photovoltaic systems. As the simulation of a photovoltaic system requires a combination of optical, thermal and electrical modelings, the methodology chains sub models based on the recent literature review and related aspects for an accurate prediction of the energy yield of bifacial PV systems. Two main approaches, ray tracing and view factor, are evaluated for modeling the front and back irradiance on bifacial photovoltaic modules. Coupled to the thermal and electrical model results, a calculation of the energy production and the bifacial gain is achieved.

For the validation of the simulation following this methodology, the results are compared with experimental data acquired on 4 PV systems comprising small and large-scale systems with different mounting configurations, at different locations and based on different bifacial technologies.

The results show an overestimation in the energy yield prediction for an 8-module system of between 3 and 4 percent, and between 2 and 3 percent in the case of a large-scale system.

The results thus demonstrate that the energy yield of bifacial can be modeled with similar accuracy to the monofacial PV systems. Finally, this simulation method is applied to the exploration of fault detection and the diagnosis of a photovoltaic system through the application of neural networks for fault classification by training from a synthetic database. An accurate simulation helps the identification of faults and their location in large photovoltaic systems; this is a key issue to improve the maintenance and the operation of such plants.

Contents

CHAPTER 1

Introduction

1.1 Context

According to the current pace of CO_2 emissions by the year 2050 the world will undergo a global human-induce warming[1] up to 3.5°C above preindustrial levels [2].

The global commitments now aim to limit the rise in global temperature to 1.5° C to avoid the worst effects of climate change. The path to achieve this scenario requires major business, economic, and societal changes. The 1.5°C scenario outlined in the 2021 World Energy Transition Outlook 2021 (WETO) envisions six technological leads of an energy transition compatible with meeting the 1.5°C Paris climate goal [3], including the renewable electricity generation sources such as solar Photovoltaic (PV), wind, etc. and the direct use of clean electricity across all economy sectors and applications.

According to the IEA (International Energy Agency), this energy transition or the path to net zero emissions as a transformation of the global energy sector from fossil-based systems of energy production and consumption to renewable energy sources, requires the massive deployment of all available clean energy technologies. Therefore, a vast annual investment is expected in order to achieve the 2050 targets. A key element of investment to address the net zero emissions is the surge of the share of electricity in total final consumption, in tandem with an increasingly decarbonised power system. Among renewable technologies, solar PV installations have seen the fasted growth, with a 21-fold increase in the 2010-2021 period, as a result of major cost reductions backed by technological advancements, high learning rates, policy support and innovative financing models. At the end of 2021, the cumulative installed capacity of solar PV reached 843 GW globally. To fulfil the 1.5°C scenario wind and solar PV will have to supply 42% of total electricity generation by 2030 (from just over 10% today). The installed generation capacity of renewable power will need to expand to four-fold and ten-fold increase by 2030 and 2050, respectively, over the 2020 level [4] as depicted in Figure

[1] According to the Intergovernmental Panel on Climate Change (IPCC) [1] the global warming is defined as an increase in combined surface air and sea surface temperatures averaged over the globe and over a 30-year period, expressed relatively to the period 1850–1900 used as an approximation of pre-industrial temperatures.

1.1.

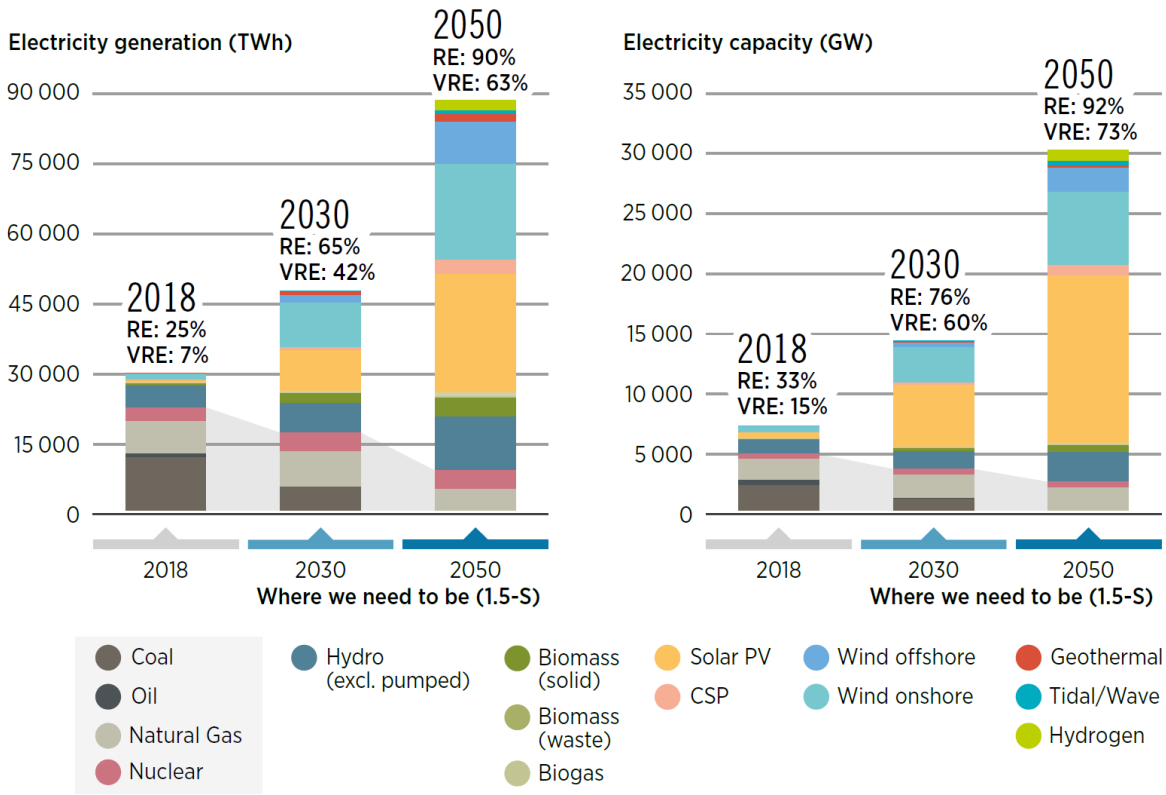

Figure 1.1: Global total power generation and the installed capacity of power generation sources in 1.5°C Scenario in 2018, 2030 and 2050.
1.5-S = 1.5°C Scenario; CSP = concentrated solar power; GW = gigawatts; PV = photovoltaic; RE = renewable energy; TWh/yr = terawatt hours per year; VRE = variable renewable energy. World Energy Transition Outlook 2022 [3]

The covid-19 pandemic have exposed the weaknesses and vulnerabilities of a system heavily dependent on fossil fuels. According to the World Energy Council, in the first year of the pandemic the perception from the policy makers, CEOs and leading industry experts regarding the level of impact and uncertainty of all energy transition issues showed a significant increase in uncertainty. Although the loosening of pandemic restrictions and the re-opening of global trade and in addition to this, the current rising in Ukraine, brings new levels of uncertainty, rising the costs to economies that remain deeply tied to fossil fuels. Nonetheless, renewable energies consolidate their position at the top of the action priority agenda within the queried experts.

Therefore, renewable energies continue to be a long-standing action priority as the energy sector implements established technologies and integrates them within the energy system. To accelerate the capacity of new PV plants and their integration into the grid, the levelized cost of electricity (LCOE) needs to be lower or equal to that of conventional energy sources .

This can be realized by developing high efficiency and cost effective solar PV modules i.e. increasing the generated electricity of the PV system.

1.2 Motivation of this study

As a both side irradiance sensitive device a bifacial photovoltaic (PV) is a promising technology based on the utilization of both front and back sides of solar cells for light absorption. The major advantage of this technology is the increased energy yield per square meter of a PV system as a result of the backside absorption of light and is called bifacial gain.

At the time of starting this work (2018), bifacial technology systems were not yet well spread over the world and experimental data regarding their performance was still scarce. With no standards established yet at that point for measuring and testing bifacial modules, there was no agreement between manufacturers on how to define the bifacial module characteristics. At the same time there were no accurate tools to predict the performance of a bifacial system and thus increase confidence and interest of investors. This has lead to a slow penetration in the market despite good laboratory results and the maturity of bifacial solar cell development. After 2019 the standardization issue was addressed via the IEC[2] norm (60904-1-2)[5] and in terms of market share, according to the International Roadmap of Photovoltaic (ITRPV), bifacial technology implementation was expected to grow from 12% in 2019 to nearly 60% of total global installations by 2029.

Since the bifacial gain is due mainly to the rear active side of the module, this gain strongly depends on the irradiance level, but also on different geometric parameters, unlike a conventional monofacial installation, such as the height of the module above the ground, the shape of the supporting structure, the tilt of the PV array and specially the albedo of the ground. This ability to generate power from the rear side, which seems to add complexity when designing a system, is what gives extraordinary versatility, as now the design of a bifacial power system can be thought of to be incorporated into different structures and shapes such as in a vertical installation or rooftop sheds or simply in a tracking system. Hence, there has been a huge interest in developing models to simulate accurately the performance of bifacial systems, but the validation against high-quality long-term data remains an ongoing task for the research centers and this issue has been overcome in this dissertation. Also, as the installed capacity of photovoltaic systems increases, there is a growing need for models that can be applied to the diagnosis and failure detection of photovoltaic systems in order to further reduce operating and maintenance costs. Accurate model simulations can enable real-time detection or diagnosis from a database of faults from a bifacial PV power plant.

[2]The International Electrotechnical Commission (IEC)

1.3 Objectives of the study

The aim of this thesis is the modeling of bifacial PV systems, the validation of the models and the investigation of the main parameters impacting the performance of bifacial PV systems under different conditions of installations. The objectives of this dissertation are as follows:

- Implementation of a framework for the simulation of bifacial PV plants.
- Estimation of the electrical production of PV systems at the plant scale, under different conditions.
- Ensurance of friendliness, accuracy and computation speed of the simulation tool.
- Validation for bifacial PV systems gain under different configurations.
- Revision on fault detection and diagnosis.

1.4 Dissertation outline

This dissertation consists of 7 chapters, chapter 1 involves the context as a general introduction to the topic, the relevance of renewable energies to the global environmental and energy requirements and the rol of bifacial technology is highlighted. The challenges that bifacial technology is still facing are described, as the motivations and reasons for having this work done. In the end, the main objectives of this work are summarized.

Chapter 2 provides an overview on the solar photovoltaic principles and bifacial PV systems modeling background. Different designs of bifacial PV cells, the main characteristics of a bifacial PV module are presented to then define a bifacial PV system. Differences between bifacial PV and monofacial PV technologies are also discussed. The chapter 3 encompasses the theoretical backgorund with specific regard to the simulation of photovoltaic systems and particularly bifacial systems. The main methods for simulating back incident irradiance are presented here together with the main equations mathematical formulation for the electrical and thermal modeling of bifacial PV systems.

The chapter 4 present the validation of the main methods used for simulation of the incident back irradiance. The photovoltaic systems used for the validation and the measurement equipment are presented. Validations are presented at the level of fixed-angle and tracked test benches as well as at the level of a large-scale power plant.

Chapter 5 presents the validation of the temperature and array models by comparing the main performance indicators, such as normalized power, bifacial gain. These comparisons are carried out using data measured on a large scale system and test benches. For the latter, validation from different state-of-the-art bifacial technologies is presented. The modeling chain developed previous chapter is used as for application of fault detection of a bifacial PV system prsented in chapter 6. Based on syntetic data created from the modeling of a bifacial PV system it is explored the use for training a supervised learning algorithm.

Chapter 7 summarizes the main outcomes of the dissertation and the answers to the main research questions of this work. Besides, suggestions are made for further improvements and remaining research questions for future work.

CHAPTER 2

State of the art of bifacial systems

This chapter describes the basics of photovoltaics related to bifacial systems. Solar radiation and its main characteristics are described at first. The principle of photovoltaic conversion is analyzed as well as the different designs of bifacial PV cells and bifacial solar modules involved in this work. Finally, the parameters that describe bifacial PV systems are introduced.

2.1 Solar radiation

The Sun is the nearest star to the Earth. The main source of energy on Earth is the radiation coming from the Sun. This energy is, among others, the origin of the water cycle, storms and photosynthesis. The photosynthesis is the transformation of photons in organic matter, crucial for the chain of living beings. Thus, the Sun is source of energy and life on Earth. Despite the complex structure of the Sun, a simplified model can be adopted for the applications of the thermal processes derived from it. The Sun can be considered as a black body that radiates energy at a surface temperature of 5778 K [6]. The spectral distribution of extraterrestrial solar irradiance, G_{ext}, i.e., measured outside the Earth's atmosphere, is similar to that of the black body at this temperature.

The Earth, in its motion around the Sun, describes an elliptical orbit, with low eccentricity, so that the distance between the Sun and the Earth varies by about 3% along its path.The radiation emitted by the sun barely varies over time and its value at the top of the Earth's atmosphere is known as the solar constant I_0. It is defined as the solar energy per unit time received on a surface of unit area perpendicular to the radiation. This radiation, as it passes through the atmosphere, is partially absorbed and scattered by the components of the atmosphere; in recent decades, with the availability of artificial satellites, it has been possible to make direct measurements of solar intensity, free from the influence of the Earth's atmosphere. NASA measurements indicate that the value of the solar energy constant is 1367 W/m^2 (1.6%) [7].

As it travels from the sun, the spectral distribution of solar radiation barely changes until it reaches the outer layer of the Earth's atmosphere. However, before reaching the earth's surface it must travel through the atmosphere where it is attenuated by the processes of absorption and scattering due to the interaction with the different atmospheric components (see figure 2.1). The longer the path, the greater the attenuation of solar radiation. These interactions and the angle of incidence of the incoming radiation determine the total amount of power that finally reaches the Earth's ground, as well as its spectral distribution.

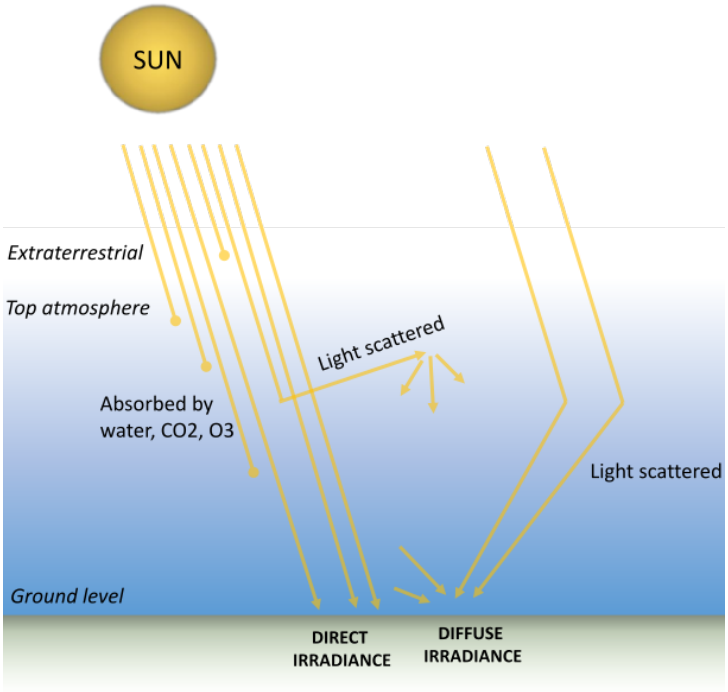

Figure 2.1: Interaction processes between the earth atmosphere and solar radiation, and resulting solar irradiance components.

To calculate the incidence angle of solar radiation, it is mandatory to know the Sun position respect to the reference. The Sun position can be defined by two angles respect the local reference.

- Solar zenith angle θ_z, corresponds to the angular distance between the Sun and the zenith, that is an imaginary point directly above the observer on the blue-vault.
- Sun elevation α_s, is the angular distance from the horizon to the Sun position in the sky. It is the complement of the solar zenith angle.
- Azimuth α_{SAZ}, is the angular displacement of the orthogonal projection of the Sun's position on the horizontal plane. The angular distance is measured from North and clockwise direction i.e. North=0°.

The air mass (AM) is a term related to the length of the path traveled by the direct beam in the Earth's atmosphere relative to a vertical path directly to sea level [8], described as follows,

$$AM = \frac{1}{\cos(\theta_z)} \tag{2.1}$$

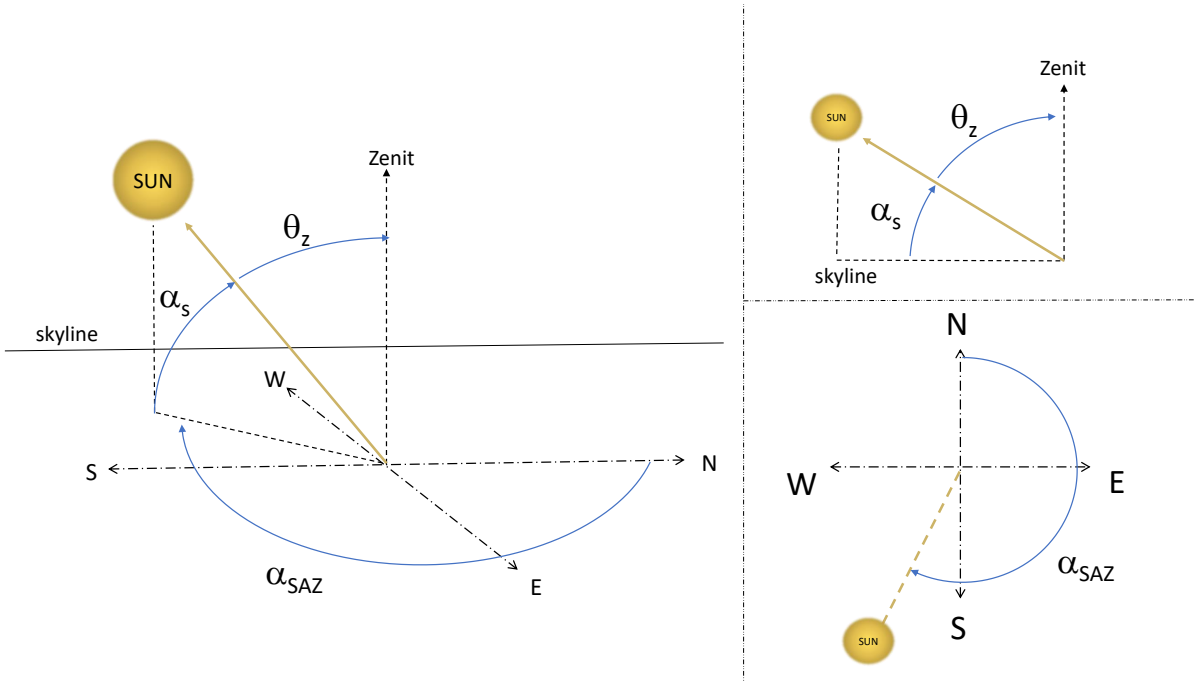

Figure 2.2: Angles for the calculation of sun position. Solar zenith angle θ_z, sun elevation angle α_s and solar azimuth α_{SAZ}

The surface power density of radiation (irradiance) coming from the Sun without suffering the scattering and absorption processes measured in a normal incidence plane is called Direct Normal Irradiance (DNI). Its unit is expressed in W/m².
The irradiance scattered by the atmosphere and received by a horizontal surface is labeled as the diffuse horizontal irradiance (DHI); the DHI is a the fraction of light that does not come directly from the sun (i.e. reflected by the atmosphere, the clouds, the ground and other obstacles).

The global irradiance reaching a horizontal surface (GHI) is expressed as the sum of its two aforementioned components, i.e. the projection of the direct irradiance onto the horizontal surface plus the diffused component.

Consequently, the relationships between GHI, DHI, and DNI on a horizontal surface is expressed as:

$$GHI = DNI\cos(\theta_z) + DHI \tag{2.2}$$

Finally, the DNI and extraterrestrial irradiance are related by the Lambert-Beer law as,

$$DNI = G_{ext} \cdot e^{-k \cdot AM} \tag{2.3}$$

Where k is the extinction coefficient of the atmosphere related to presence of the atmosphere components.

2.2 Albedo

Since the gain of bifacial PV is mainly due to the capacity of power generation from the incident irradiance on the backside of the modules, the amount of reflected radiation from the ground plays a crucial role on the generation surplus in a bifacial PV installation. This will impact the profitability of a PV project.

The albedo is a key parameter that is widely used in land-surface energy balance studies, weather predictions, and global climate change investigation [reference book]. It is defined as the ratio of the surface-reflected irradiance to the incident irradiance, thus it is a dimensionless value and can go from 0 to 1. Accordingly to this definition, the albedo is subjected to the directional distribution of the incident irradiance and is not an intrinsic property of a surface, it depends on the spectral and angular distributions of the incident light, which are linked to the atmospheric composition and the position of the sun. Therefore, albedo changes throughout the days and the seasons. Moreover, since surfaces are not perfectly planar, the reflected irradiance is distributed around a reflection angle in multiple directions according to the roughness of the surface. Thus, reflective materials can be described as being "diffuse" or "specular" where the intensity of reflected radiation can be the same in all directions (isotropic) or vary according to the direction (anisotropic).

The surface underneath the modules in a PV installation can be modified, with natural materials or artificial covers, in order to increase the amount of reflected irradiance incident on the PV modules backside as shown in the following figures.

(a) Enhanced albedo with white gravel (0.4 approx.)

(b) Natural desert albedo at the PSDA, Atacama Desert, Chile. (0.3 approx.)

Figure 2.3: Different albedo due to locally conditions of the ground beneath modules.

Main sources of albedo data are in situ measurements and satellite derived databases. In the last years major efforts were conducted in the development of satellite-derived irradiance databases, this is how public domain gridded ground albedo or reflectance databases are now available [Reference Gueymard]. The validation of albedo databases is mainly done against surface measurements, which can be representative of the area comprehended by the pixel size of the albedo database only if the area is perfectly homogeneous. The latter is often only possible in flat arid areas such as deserts. Some initiatives as the one managed by SURFRAD [1] are looking for providing accurate data of albedo for research. Spectral

[1] The Surface Radiation Budget Network Data (SURFRAD) is currently operating several stations across

effects must be considered in bifacial PV performance estimation and monitoring, due to both the strong impact of ground surface spectral reflectance on the rear sides spectral irradiance available for PV power generation. It has been been found that a thermopile pyranometer and PV reference cell may show deviations on the order of 16.5 W/m^2 and 3.6 W/m^2 respectively, when comparing the rear rearside irradiance measurements to the effective rear side irradiance available for PV power generation [9]. This deviations depends strongly on the ground reflecting materia. An agreement between 2 and 3 W/m^2 have been between a reference cell and module incident irradiance for lightsand and darksand ground, when considering the spectral reflected irradiance. In this work the validations are carried out mainly in desert conditions with albedo mean values between 2 and 3.

In most of the cases the estimation of the albedo is done by considering a constant mean value from long term data measurements. Since over long time periods the albedo might significantly change, a constant value for a one year-period is a poor approximation to be used in modelling of bifacial PV plants. In this dissertation the broadband albedo measurements in-situ are used for performing simulations unless otherwise expressed.

2.3 Ground based instrumentation for solar resource measurement

To measure solar radiation there are two types of instruments based on two different physical principles: thermoelectric and photoelectric. Within the thermoelectrical sensors we classify the pyranometers and pyrheliometers. In general terms, pyranometers and pyrheliometers are sensors based on thermopiles. A thermopile is a set of thermocouples that generate a potential difference from a temperature gradient between the reference and the surface to be measured, which with the appropriate calibration may give the values of solar irradiance incident on an absorbent surface. The absorbent surface is irradiated by the solar radiation rising up its temperature. The absorbent surface is isolated from the environment by a glass, which for a pyranometer has a spherical shape to reduce the losses due to the angular reflections of incident radiation for lower sun elevation angles.

Therefore, the spectral response of thermopile-based sensors is independent of the wavelength and has a flat shape between wavelengths of 310 and 2800 nm in the case of a pyranometer, and between 250 and 4000 nm for a pyrheliometer, as depicted in Figure 2.5.

As mention in the previous section there are three main components of solar radiation. The DNI is normally measured by a pyrheliometer sensor mounted in a sun tracking system as indicated in Figure 2.4. By its side, when horizontally mounted in a sun tracking system, a pyranometer is typically used to measure the DHI assisted by a shading ball as depicted in 2.4, so that the direct solar irradiance is masked. Finally, the GHI, as the sum of the DNI and DHI, is measured by placing a pyranometer in a horizontal plane, and its unit is expressed in W/m^2.

the U.S in order to provide accurate data for climate research and validation of satellite estimations. These data can be found in the DuraMAT Consortium data Hub project

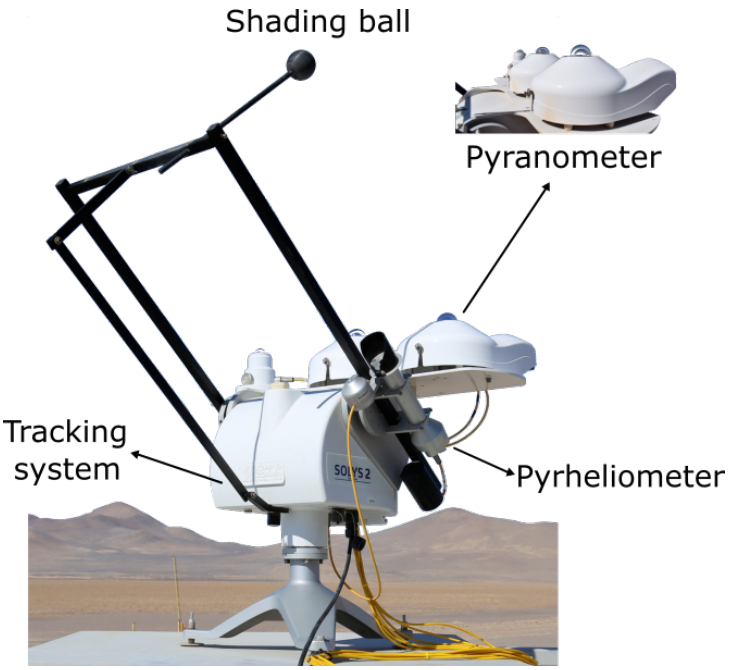

Figure 2.4: Radiometry equipment for in situ irradiation characterization.

Unlike thermopiles based sensors, the solar reference cells are based on the photovoltaic effect. Basically, they are made of a PV cell calibrated to output irradiance values from the generated voltage once its surface is reached by the incoming sunlight. Because of its nature, its spectral response depends on the wavelengths as well as a PV module cell. In fact, a reference cell working spectral range goes from 300 to 1100 nm approximately, similar to the PV module cells.

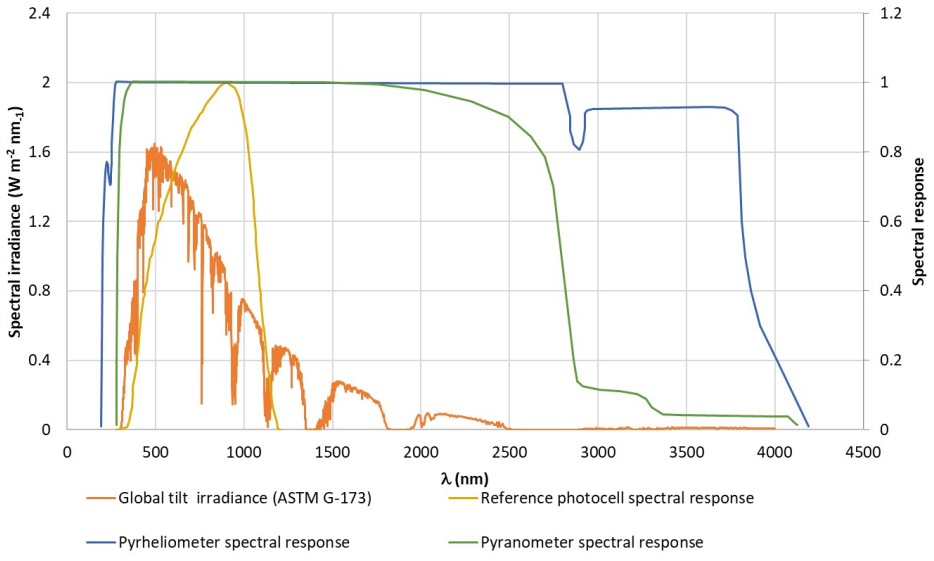

Figure 2.5: Spectral Responsivity (SR) of thermopile based sensors and a reference cell for solar resource characterization.

Due to the difference in spectral response, the thermopile based sensors are typically used for solar resource assessment, while solar reference cells are usually found in PV plants for performance assessment. Thus, reference cells are usually attached to the support structure of a photovoltaic system to quantify the incident solar resource in the plane of the PV array (POA). In the case of a bifacial PV system, they should be located on both sides of the module plane, i.e. to measure the part of irradiance from the sky, as well as the incident irradiance on the back side of the PV module, as illustrated in Figure 2.6.

For measuring the albedo of a ground surface, we can account on an albedometer. Basically, it consists of two horizontal pyranometers: one facing upward i.e towards the sky for measuring the GHI, and another pyranometer facing down for measuring the reflected irradiance from the ground, as shown in Figure 2.6. Some albedometers are using two calibrated reference cells sensors, but it is relatively seldom. The ratio between the reflected and upward incident irradiances defines the albedo of the surface.

(a) Reference cells in the POA of a fix tilted installation at the PSDA.

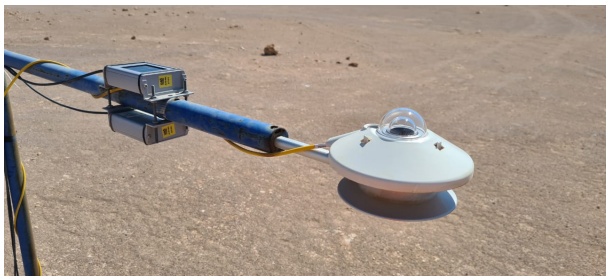

(b) Albedometer sensors made up of reference cells and pyranometers.

(c) Reference cells at the POA of the fix tilted installation at the PSDA for rear irradiance measurement.

(d) Pole for meteorological conditions measurement at CEA-INES.

Figure 2.6: Installed equipment for solar irradiance data measurement at a specific location.

In order to quantify and determine the environmental conditions of operation of a PV system, usually a weather station is placed near the site of evaluation so as to gather periodically the time series from measured wind speed, ambient temperature, wind direction, water precipitation, among others. These measured environmental variables along with the irradiance data from the monitoring station, are essential for the modeling of PV systems. Such time series from measured solar irradiance and environmental variables from in situ monitoring stations are used within this work.

2.4 Photovoltaic solar cells and operation principles

The standard solar cell is based on a semiconductor PN junction as depicted in 2.7. For the construction of a solar cell, an n-type doped region (i.e. doped to have an excess of electrons, e-) is obtained by phosphorus diffusion at the surface of a p-type doped silicon substrate (i.e. doped to have an excess of holes, h+), to form the PN junction. The presence of this junction induces the diffusion of exceeding electrons towards the P substrate and of the exceeding holes towards the N region, thus leaving positive and negative ions at each side of the junction respectively. This creates an electric field across the junction, which opposes the diffusion of charges, until an equilibrium is established, thus maintaining the charge carriers in the region where they are a majority.

The incident photons penetrate the cell through its entire front surface and, depending on their wavelength, are absorbed in the N region and then in the P substrate. The more energetic near-ultraviolet (UV) photons are absorbed in the first micrometers, while the less energetic infrared (IR) photons are absorbed in the substrate and can reach the back face of the cell after a few hundred μm. Photons are absorbed into the silicon releasing electron-hole pairs. The electric field at the PN junction will help to separate these carriers and allow their collection through the corresponding cell terminals into an external circuit, generating an electric current. If the minority carriers (electrons in p-type, holes in n-type) don't reach the electric field after diffusing into the material over an average distance (the diffusion length), they will recombined and the electron-pair is lost for current generation. Note that p-type substrates were the first to be used because they are simpler to implement, while charge carriers have a better ability to diffuse in n-type substrates.

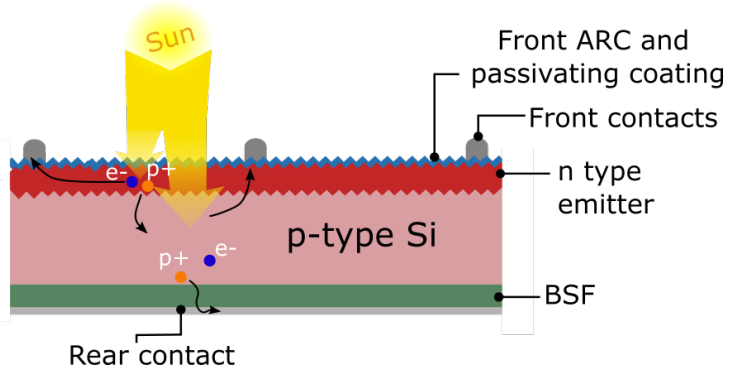

Figure 2.7: Solar cell NP junction.

For the external collection of photogenerated charges, a metal grid (a silver / aluminum alloy in general) is used at the front side to let photons enter the structure, and on the back side, there is a metal coating (aluminum) on the complete surface, opaque to photons but reflective. In a closed circuit, the minority charge carriers generated by the absorption of photons diffuse towards the PN junction where they undergo the action of the electric field, which gives them the necessary impulse to reach the opposite metallic collector (front face grid for the electrons, and back face plate for the holes). At the same time, the majority of carriers participate in an electric current in the external circuit. Note that the thickness and doping of the different layers are optimized to maximize the efficiency of the cell (ratio between electrical power supplied and incident optical power). For example, the N layer is thin and heavily doped (high excess of electrons) to generate a strong electric field, and is therefore generally noted N+.

Thus, the standard monofacial crystalline solar cells follow the structure presented in picture 2.8:

- Screen printed silver paste to form the contacts.
- Anti Reflective Coating.
- Phosphorous diffused emitter and boron doped silicon wafer that form the P-N junction.
- Aluminum Back Surface Field (Al-BSF).
- Screen printed aluminum paste.

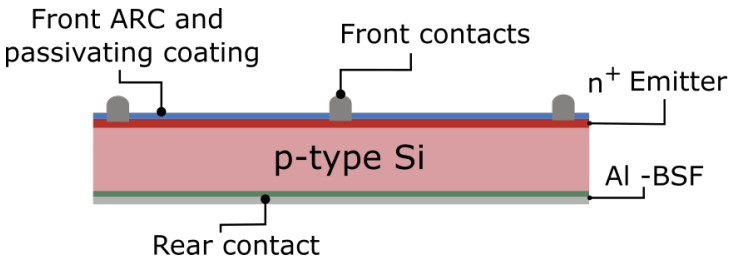

Figure 2.8: Standard p-type Si solar cell. This solar cell receives a homogeneous phosphorus (P) diffusion for p-n junction (n+ means a doping in the order of 10^{20} P atoms/cm^3), a plasma enhanced chemical vapor deposition (PECVD) step to create a silicon nitride (SiNx) passivation layer of around 70 nm that also works as antireflection coating, a screen-printing metallization of silver (Ag) and aluminum (Al) containing pastes and a firing step. An aluminum-silicon (Al-Si) alloy forming a p+ region (the Al-BSF) at the back silicon surface is obtained during firing and covers the full back contact area. Note that Ag busbars are not included in the figure.

2.4.1 Bifacial cell technologies

As well as for a monofacial solar cell, the basic structure of a bifacial solar cell includes in the semiconductor wafer, an emitter, a back surface field (BSF) and anti-reflective passivation coatings at the front and at the back surfaces of the cell (SiNx). In fact, whereas in a monofacial solar cells an aluminum rear contact covers the entire backside surface (Al-BSF),

in bifacial solar cells a metalization grid is printed on the backside to allow the light to penetrate through the back surface of the cell. The standard solar cell architecture has been in use since the last 30 years. The steady incremental improvements brought to the standard (Al-BSF) cell technology (Figure 2.8) were economically and technically feasible. Nonetheless, the standard PV cell structure presented two main drawbacks: a strong rear-side recombination at the full-area aluminum back contact and partial absorption of infrared light at the rear. Promoted by the availability of high-quality low-cost wafers in the market, from mid 2016 the PV industry started to implement new cell concepts such as PERC and nPERT.

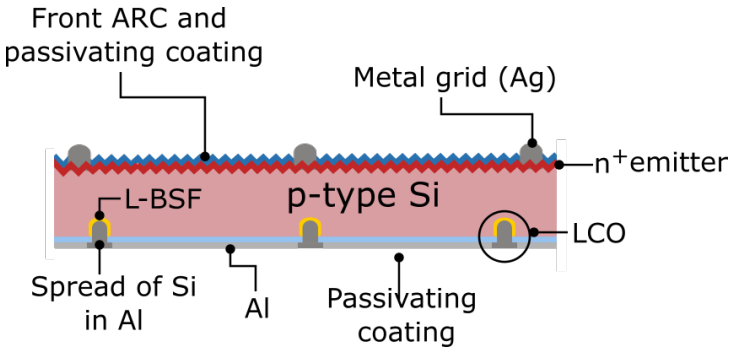

Figure 2.9: Passivated emitter and rear contact (PERC) solar cell. This solar cell receives a homogeneous P doping and PECVD SiNx layer at the front side and local contact openings (LCO) via laser beam at the rear side. Since the interaction between Al and Si occurs locally, delimited sharp-dark lines in the Al layer are created. As a result, the Al-Si alloy and the local back surface field (L-BSF) are formed in the LCOs at the back contact area.

The PERC cell technology defines a solar cell architecture that differs from the standard cell. Indeed, instead of an aluminum-silicon layer covering the the full back contact area, the PERC architecture essentially improves light capture near the rear surface and to optimizes electrons capture. This is achieved by introducing localized metal contacts and partial passivation at the rear side of the cells. By introducing these improvements, the two previous limitations of the standard cell were adressed; this is how monofacial PERC cells rapidly replaced the Al-BSF cells. In fact, the PERC technology represented more than 80% of the bifacial market share in 2020. However, monofacial PERC is near its upper efficiency limit of 22.5%, thus a way to increase its output power is moving PERC cells to a bifacial technology (PERC+) and implementing new topologies as poly-Si of n-type. Due to a lower degradation under space application conditions, p-type solar cells were mainly driving the production of the industry to a fully optimized p-type solar cell and therefore achieved a low cost limit. Up to present days, according to the International Technology Roadmap for PV (ITRPV), the standard mass-produced p-type substrate cells represent more than the 80% of the market share. In 2020 about 10% of PERC cells were produced with p-type multicrystalline silicon (mc-Si) material, and 82% were PERC on p-type monocrystalline silicon (mono-Si). Nonetheless, a strong increase of n-type solar cells in the market share is expected up to 50% during the next ten years. The main advantage of n-type solar cells is a better stability of the cell efficiency since the "Light Induced Degradation" (LID) does not occur in n-type Si. LID is indeed due to the boron-oxygen reactions under illumination in p-type Si substrates that creates a charge recombination. A module of this technology can typically lose up to 2% - 3% of its efficiency in the first weeks after installation [reference]. In order to prolong the p-type

dominance in the PV market, efforts are made on the p-type material quality by Ga-doping instead of B-doping, and increasing the wafer size. Actually, a certified efficiency of 23.39% was obtained for a 252 cm^2 PERC+ cell. These limitations of p-type solar cells are driving the PV industry towards high efficiency n-type solar cells. Figure 2.10 shows the nPERT cell structure. This cell concept extends the range to higher bifaciality, up to 95%.

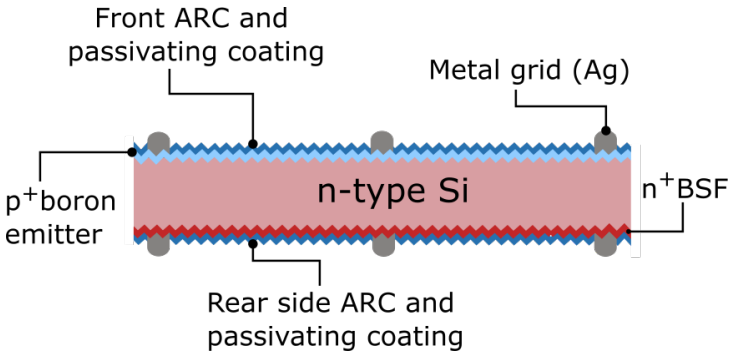

Figure 2.10: Bifacial nPERT structure solar cell. An homogeneous P diffusion creates the BSF at the back side of the wafer while a homogeneous boron (B) diffusion generates a p-type emitter at the front side. During B diffusion, a 15 nm boron silicate glass (BSG) is formed and used as passivation layer. The passivation of the n-type BSF is ensured by a SiNx deposited by means of PECVD that also recovers the p-type emitter resulting in a BSG/SiNx stack system. Screen-printing metallization with an Al and Ag containing paste for the front metal grid and Ag paste for the rear metal grid allow the formation of the contacts.

In heterojunction solar cells (HET), the highly recombination-active contacts are displaced from the crystalline surface by insertion of a thin film with a high band gap (usually hydrogenated amorphous silicon (a-Si:H) films are used in this cell structure). HET solar cells decrease recombination-related losses in conventional solar cells by using carrier-selective passivating contact structures that simultaneously provide surface passivation and carrier selectivity in place of the highly recombination active direct contact regions between the silicon absorber and the metallization [10]. Figure 2.11 presents the typical bifacial HET solar cell structure in front-junction configuration. Generally, HET cells are based on n-type mono-Si wafers because HET production does not include a high-temperature treatment that would aid in impurity gettering and deactivating boron-oxygen defects.

Owing to the high-quality chemical passivation of the silicon substrate surface provided by the hydrogen contained in a-Si:H, HET technology enables very high Voc values: values of up to 750 mV — very close to the theoretical limit—were reported [11]. Thanks to their outstanding Voc level, HET solar cells currently own the world record efficiencies for single-junction solar cell technologies: 26.3% in bifacial configuration and 26.7% in interdigitated back contacted configuration [12].

HET technology offers other significant advantages: lower power losses at high temperatures thanks to a low temperature coefficient, compatibility with thin wafers thanks to their low temperature fabrication process thus enabling lower costs, and a high bifaciality potential. The high efficiencies reported for both configurations (front-junction configuration with p-type layers at the front and rear-junction configuration with n-type layers at the front) confirm the intrinsic bifacial nature of the HET solar cells [13]. Typically, the bifaciality factor of the HET

cells is above 92%. As its most significant limitation, HET solar cells experience parasitic optical absorption in the transparent conductive oxide and a-Si:H layers, which introduces a trade-off between Voc and Jsc of the cells [14]. However, with its high efficiency potential, HET cells are expected to gain significant global photovoltaic market share in the coming years [15].

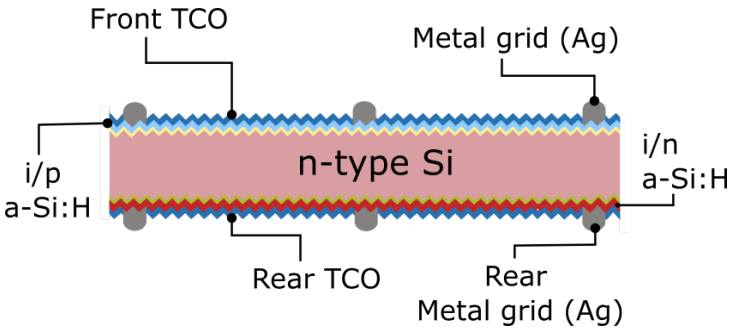

Figure 2.11: In the HJT cell structure, surface passivation is provided by intrinsic amorphous silicon a-Si:H(i) layers deposited by plasma-enhanced chemical vapor deposition (PECVD) on both sides of the wafer, carrier selectivity is provided by in-situ doped a-Si:H layers on top of them. N- and p-type doped a-Si:H layers are applied to opposite sides of the wafer, respectively, to form electrical contacts to the electrons and holes in the wafer. To enhance lateral transport of the collected carriers toward the metallic grids, transparent conductive oxides are sputtered on top of the doped a-Si:H layers on both sides of the wafer. Ag metallic grids are finally screen-printed on both sides of the cell to form the metallic contacts.

Details on PERC, PERC+, nPERT and HJT technologies have been given here as field data used for model validation (see chapter 5) are based on these technologies.

2.4.2 Bifacial PV modules

The main functions of a PV module are to reach useful voltage levels, provide a mechanical rigidity, and isolate the solar cells from the external environment (humidity, UV irradiation). The cells are usually connected in series to achieve the desired voltage level and minimize the current conduction losses. In a conventional electrical module configuration, each cell is connected to its neighbor by tinned copper strips soldered to both the front side busbars of the first cell and the back side contacts of the neighboring cell. Each row forms a string of cells, which is then encapsulated in a transparent resin such as EVA (Ethylene Vinyl Acetate). While an opaque polymer is used on the back face ("backsheet") for a conventional monofacial module, two possibilities are available for bifacial modules:

- with a tempered glass on the front and back faces,
- with a tempered glass on the front face and a transparent polymer on the back face.

Since PV cells are getting closer to the efficiency limits, the c-Si based modules are being the focus of developments in order to increase the module efficiency and reduce the cell to module conversion ratio (or conversion loss). This ratio corresponds to the change in electrical performance of the PV module regarding the initial state of the PV cells, i.e., before being

embedded into the module. The election of the proper configuration of a module can reduce the optical loss due to the encapsulant absorption or aging, reflection of the glass, or ohmic losses due to the series connection of the cells, among others.

The increase of the cells efficiency and bifaciliaty implies an increase of the the current and so of the ohmic losses in the PV cell strings in a PV module. What has been developed in recent years is the use of cells cut in half or even smaller pieces so as to avoid increased resistive power losses in the connecting ribbons. At the same time the number of busbars tends to increase as well as the packaging factor driven mainly by the use of full square wafers and technologies to pack the solar cells closer together. Some producers aim at increasing the cell size from the standard M0 (156×156 mm^2) to even up to M12 (210×210 mm^2) in order to enhance the performance per Wp of the production and further reduce the cost of cell production per Wp. This leads to a greater market share of higher power modules with a larger size. The current outperforming modules with efficiencies from 21.6% up to 22.5% are made up of half cut bifacial cells with output power from 550 up to 700 Wp [reference taityang news list].

In practice, to obtain a bifacial module the glass - EVA - cells - EVA - glass (or backsheet) structure is pressed and heated while evacuated in a laminator. With proper temperature and pressure time profiles, the EVA melts, conforms to the shape of the glass (or backsheet) and hardens.

The module may then be framed or frameless. The typical structure of a bifacial module is made with a frameless glass-glass configuration. Lately, the trend rather goes back to bifacial modules with frames as they are more rigid, less fragile and easier to handle during installation [16] The electrical outputs are driven by means of junction boxes (J-box), where the protecting bypass diodes are placed to every two rows of cells. The junction boxed are designed to be shallow in order not to cause any shadowing on the rear side of the modules. For the traditional laminated 60 full-cells (or 72 full-cells) PV module, one J-box is glued with silicon adhesive to the backside. As for a 120 half-cell module (or 144 half-cells), the connections are made by placing three J-box at the backside. The majority of PV junction boxes have an ingress protection (IP) at least rating of 65 [17].

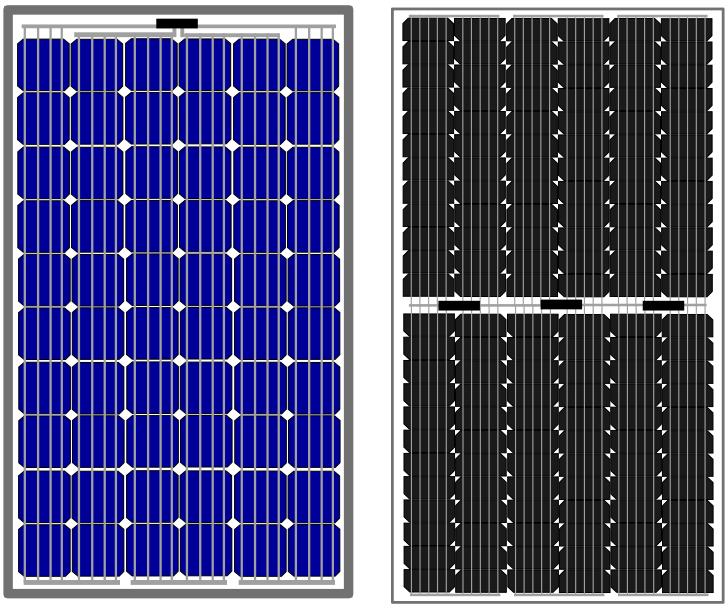

Figure 2.12: Left) Conventional 60 full-cell module structure with a single junction box in the top of the module attached to the backside for bypass diode protection. Right) 144 half-cell module. A half-cell module doubles the number of cells into 120 or 144 cells regarding the full-cell module and so the electrical current through each busbar is halved. Three J-boxes at the center of the module where each 24 half-cells strings of the two twin sections of the modules are connected in parallel to a bypass diode.

2.4.3 IV characterization

The characterization of a PV module is essential for determining its state or assessing its performance. In particular, the specification of the electrical features are needed for product labelling. The key electrical parameters provided by the manufacturer datasheet of the PV module are established by measuring its current-voltage (IV) characteristic curve in reference conditions.

The IV curve is used to specify the main electrical parameters of a PV module or a solar cell, i.e., the voltage at open circuit condition (V_{oc}), the current at short circuit condition (I_{sc}), and, the voltage (V_{mpp}), the current (I_{mpp}) and the power (P_{mpp}) at the maximum power point (mpp). Based on these main parameters, other important variables can be calculated, such as the fill factor (FF) and the efficiency (η). Parameter of the equivalent electrical model, such as the series resistance (R_s), the shunt resistance (R_{sh}) and the photocurrent or light-generated current (I_{ph}), can also be determined from the IV curves [18].

The IV curve is usually measured at laboratory with a solar simulator and under the specific conditions according to the IEC 60904-9[2] or ASTM E927-10[3] standards. These norms state that the lamp's spectrum used for the indoor characterization must be in accordance to the global spectrum AM1.5G described in the ASTM-G173 standard. Where AM stands for the

[2]The International Electrotechnical Commission(IEC) is an international standards organization that prepares and publishes international standards for all electrical, electronic and related technologies

[3]ASTM: the American Society for Testing and Materials is an international standards organization that develops and publishes voluntary consensus technical standards for a wide range of materials, products, systems, and services.

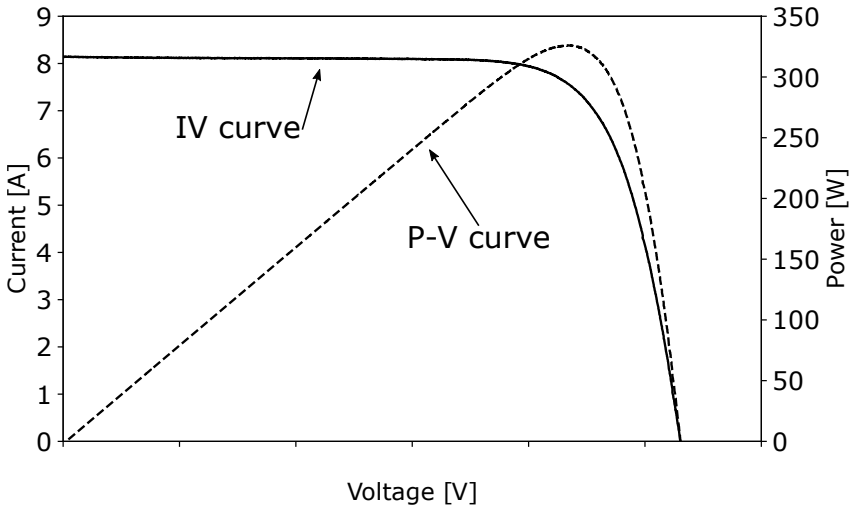

Figure 2.13: Example of I-V (continued line) and P-V (dotted line) curves.

air mass as previously defined. Therefore, to obtain the IV curve, a voltage sweep is applied to the PV device under test whilst illuminated by the solar simulator under an homogeneous light source with an intensity of 1000 W/m². Thus, the standard testing conditions (STC) are defined as [19]:

- AM1.5G spectral distribution.
- Total irradiance of 1000 W/m² (or 100 mW/cm², also called 1-sun).
- Device temperature of 25°C.

Particularly, for bifacial PV modules there was no standard for indoor characterization, and thus neither for power rating, until the IEC 60904-1-2 standard for the IV characterization of bifacial devices was published in 2019. This time, the power of the PV module is established when irradiated at 200 W/m² ($Pmax_{BiFi20}$) and 100 W/m² ($Pmax_{BiFi10}$) on the back side, keeping the 1000 W/m² on the front side.

Two methods of measuring the $Pmax_{BiFi10}$ and $Pmax_{BiFi20}$ are described in the standard: a double side illumination measurement, normally not available in laboratories since a dedicated solar simulator is needed; and single side only illumination. The latter is the most simple to be performed since it only requires a regular solar simulator. The incident frontside irradiance (G_{Ei}) needed for an equivalent double side illumination is determined as follows,

$$G_{Ei} = 1000W/m + \varphi \times G_{Ri} \tag{2.4}$$

Where G_{Ri} is defined by G_{R1}= 100 W/m² and G_{R2}= 200 W/m² to determine $Pmax_{BiFi10}$ and $Pmax_{BiFi20}$ respectively. φ is the bifacial factor.

2.5 Bifacial PV systems

In order to obtain powers of a few kW, under a suitable voltage, it is necessary to group the PV modules in series, and in parallel for an specific range of current. This grouping forms

a PV array or a PV plant. There are several possible configurations for interconnecting the modules of a PV array but the economic feasibility precludes the use of some of them. In this work, we only focus on the simple parallel series connection.

According to the components of a photovoltaic plant, we can distinguish different levels. From the PV cells, as the basic unit of a PV plant, we form a PV module and, from such PV modules in turn, we form a PV string, which is a chain of series connected modules. The number of modules in the string determines the voltage level, at which it is going to operate. Strings of same length are then connected in parallel in order to comply with the current limits established for the operation of a power inverter. The voltage has also to comply with the input voltage range for the converter. An inverter (or group of inverters) in a PV power plant has the role of extracting the maximum power from the PV generator and converting it into alternating current before injecting it into the electrical grid.

During its operation, the PV array works normally at the point of maximum power point (MPP), with the aid of an mpp tracker (MPPT) algorithm. The role of MPPT is to operate the PV generator at this MPP point constantly, as it may vary according to the environmental conditions. Accordingly, the strings must be formed by considering the expected conditions of operation, and particularly of illumination. Modules at the same position along the array's width should be connected together in order to reduce the power mismatch owing the connection of different operation points. For instance modules can be installed in portrait or landscape positions in a PV system. This will affect the operation under different conditions of shading due to surrounding obstacles or soiling. In this regard, half-cell modules are claimed to have advantages over full cell modules not only due to a reduced resistive loss but also for a better compliance with shading because of the use of two strings of cells connected in parallel within the group of cells instead of one [reference Hanifi]. Nonetheless, the configuration of installation could limit these advantages as in the case of a landscape orientation [Reference chiodetti].

Given the versatility of a device that generates energy on both sides, bifacial modules can be installed in different ways: vertically, horizontally, in a tracking system or tilted. This leads to a daily energy generation profile from a bifacial PV installation quite different to that of monofacial equivalents. The world's first large-scale bifacial system was built in the city of Hokuto, Japan, in 2013 [reference], and since then many bifacial systems have been installed in different locations. By 2020 the accumulated power of bifacial systems reached nearly 20 GWp.

For the modelling of a bifacial PV system the rear irradiance received on the back side needs to be calculated and thus the degree of complexity increases drastically compared to the modelling of monofacial based PV systems. The irradiance incident in the plane of the array on the rear side of a bifacial module is affected by several geometrical factors that might not necessarily impact the energy yield of monofacial modules, such as:

- Array's tilt and azimuth.
- Module layout (landscape or portrait).
- Clearance above the ground.
- Number of modules in a row.
- Albedo of the underlying surface.

- Shading/reflections from mounting structure.
- Shading from neighboring obstacles.

The main geometrical parameters of a bifacial PV system are described in Figure 2.14.

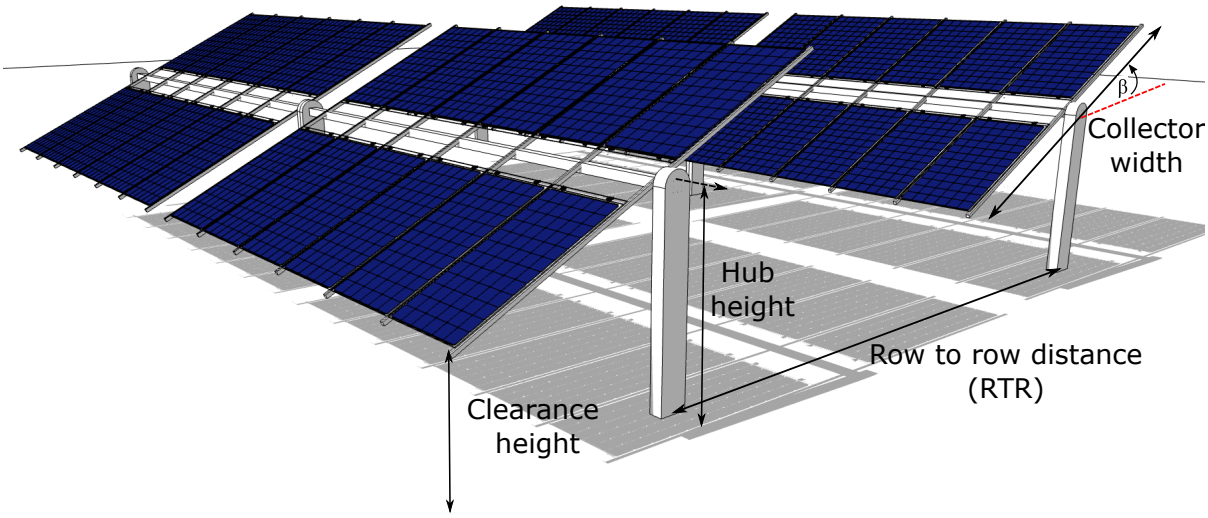

Figure 2.14: Modules mounted in a 2-up portrait configuration. Collector width (CW) equals the length of the row, i.e.,the module widths plus the intermodule space.The angle between the module and the horizontal is the module tilt β, in degrees (°). For a tracking system, β varies along the day.

The rear incident irradiance in a bifacial PV plant depends on the main parameters outlined in Figure 2.14 and on the global irradiance level. It is possible to compare different bifacial installations when normalizing some of these geometrical parameters. In a fixed tilt PV system, the clearance height is defined as the height from the ground to the lowest part of the module. The height of the PV array above the ground will impact the produced energy as it determines the quantity of light rays passing under the modules and thus taking part to the reflective irradiance. Therefore, the energy produced will be related with the ratio between the height above the ground of the PV array and the collector width (CW). In the case of a tracking system the clearance height changes due to tracking. Hence, normally the height from the axis (hub height) is used. Thus, comparisons can be made by normalizing the clearance height or the hub height in the case of a tracking system, respect to CW:

$$h = \frac{H}{CW} \tag{2.5}$$

The ground coverage ratio (GCR) is is the ratio of module area to land area, or the ratio of array length to row-to-row pitch. It is especially important for tracking systems due to the backtracking algorithms that corrects the tilt of the trackers in order to minimize shading from neighboring rows. A HSAT system requires a rather high row-to-row distance and the modules have to be relatively high above the ground compared to a fixed system, thus using bifacial modules may lead to a smaller GCR and so to a lower levelized cost of energy (LCOE). The ground coverage ratio is defined as the collector width (CW) over the distance between rows.

$$GCR = \frac{CW}{RTR} \tag{2.6}$$

Bifacial PV systems performance can be evaluated by the produced energy (E) relative to its nameplate power. The specific energy yield or simply energy yield (kWh/kWp) is defined as the generated energy (DC or AC) over a period of time ΔT divided by the front side Watt peak of the system (or module) measured in STC conditions ($P_{mpp,STC}$). The produced energy (E) of a PV system can be obtained by integrating the power production ($P_{mpp,out}$) over time. Thus, the specific yield is given by equation 2.7.

$$Yf = \frac{\int_0^T P_{mpp,out}\, dt}{P_{mpp,STC}} \left(\frac{kWh}{kWp}\right) \tag{2.7}$$

The overall energy gain of a bifacial system (bifacial gain) can be quantified by comparing the ratio of the energy yield Yf of a monofacial to that of a bifacial system. It is important to highlight that when the monofacial reference system uses a different cell or module technology, it introduces a bias and we don't strictly evaluate the bifaciality of the module. In this dissertation we will compare the results of different bifacial technologies with a monofacial reference laminated with the same module structure but a different technology. The bifacial gain (BG) is given by equation 2.8.

$$BG(\%) = \frac{Yf_{bi} - Yf_{mono}}{Yf_{mono}} \tag{2.8}$$

Where,
Yf_{bi} is the specific energy yield (kWh/kWp) of a bifacial PV system.
Yf_{mono} is the specific energy yield (kWh/kWp) of a monofacial PV system.

The first standard for establishing a bifacial module's nameplate rated power was finally released in January 2019. Before that date, bifacial technology was missing a standard for power rating. The detailed procedure of indoor and outdoor characterization of bifacial PV devices is given in the IEC 60904-1-2 standard [5]. According to the topology of the bifacial PV cell, the efficiency of the rear and front side will be different. Different metallization grid and semiconductor properties condition the amount of power produced by front and rear sides, making backside efficiency lower than the frontside efficiency. From the parameters of the IV curve measured at the front and rear irradiance levels, a ratio can be established to describe the relative efficiency. Nonetheless, in the IEC 60904-1-2 the overall bifaciality factor to be used is defined as the lowest ratio between the short circuit current bifaciality factor and the maximum power bifaciality factor measured at STC, as given in equation 2.11

$$\phi_{ISC} = \frac{Isc_{rear}}{Isc_{front}} \tag{2.9}$$

$$\phi_{Pmpp} = \frac{Pmpp_{rear}}{Pmpp_{front}} \tag{2.10}$$

$$\phi = min(\phi_{ISC}, \phi_{Pmpp}) \tag{2.11}$$

CHAPTER 3

Bifacial PV systems modeling

In recent years, due to the increasing development of bifacial technology, several institutions have undertaken the challenge of modeling PV systems through different strategies and thus demonstrate the bankability of this technology used on a commercial scale. It has not be different at CEA-INES, and in 2017, the development of the first tool to achieve the simulation of bifacial systems was carried out. Simulation of bifacial systems performance involves the integration of optical, electrical, and thermal models. Climatic parameters such as irradiance, ambient temperature, and wind speed serve as input to the thermal and optical models that, in turn, deliver the inputs for the electrical model as described by the flowchart in figure 3.1. The output from the electrical model can then be used to quantify the energy output from the system and to be input to a fault detection algorithm. The main difference between monofacial and bifacial simulation resides in the optical model. In this dissertation, the submodels previously implemented in TriFactors, precisely the temperature and the 3D view factor (or configuration factors) based optical model, are evaluated and further developed. Furthermore, in this dissertation, two optical models based on 2D VF and ray tracing are evaluated and added to the simulation chain.

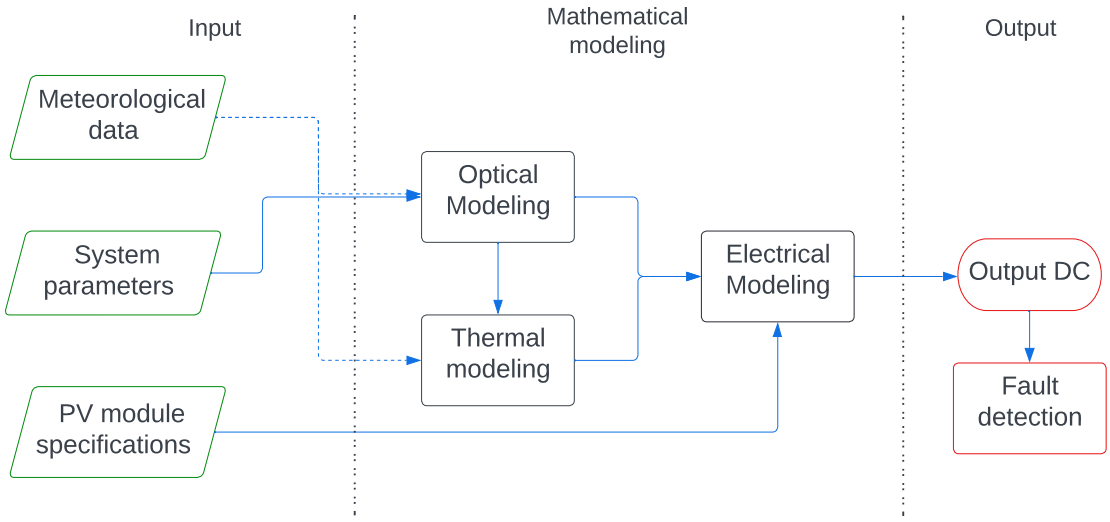

Figure 3.1: Flowchart for bifacial system modeling. The left side outlines the inputs defined by the user, right side describes the main sub-models and final output.

As shown in figure 3.1 for simulating the energy output of a bifacial PV system, the in-field measured data such as the horizontal irradiance, ambient temperature, wind speed, and ground albedo are input to the optical and thermal model. Accordingly, the optical submodel manages the calculation of the plane of array (POA) irradiance, particularly for bifacial systems, not only for the frontside but also on the rear side. However, since the rear incident irradiance depends on several factors, its calculation is not straightforward. Therefore, this dissertation evaluates two main methods based on view factors and ray tracing. If DHI and DNI are not available different models implemented in TriFactors can be used for deriving each component from GHI input data.
Since photovoltaic modules are semiconductor-based devices, the operation temperature will depend on the temperature coefficients determined by its composition and on the ambient temperature. Therefore, for calculating the module temperature, the measured ambient temperature and the thermal parameters of the PV modules are input to an experimental-based thermal submodel, as presented in section 3.2. The measured data timestamps will define the output timestamp, which can be hourly or sub-hourly.

3.1 Plane of array incident irradiance modeling

To simulate the power output from a PV system, we need to calculate the global incident irradiance on the surface(s) of the modules or PV cells, i.e., the plane of array (POA). For quantifying the POA irradiance, we have to consider the contribution of its components, such as the direct, the sky diffuse, and the reflected from the ground (see figure 3.4) components as:

$$E_{POA} = E_{dir} + E_{diff} + E_{ground,refl} \tag{3.1}$$

The DNI is converted to the beam radiation on the tilted surface simply by a geometrical

relationship once the angle of incidence (θ_{AOI}) is known.

$$E_{dir} = DNIcos(\theta_{AOI}) \tag{3.2}$$

From the figure 3.2 the angle of incidence can be derived as the angle between the beam radiation (collinear with the sun) incident onto the PV array surface and the normal of the array surface, as indicated in the following equation 3.3.

$$\cos(\theta_{AOI}) = \sin(\theta_z)cos(\alpha_{SAZ} - \alpha_{SurfAZ})\sin(\beta) + \cos(\theta_z)\cos(\beta) \tag{3.3}$$

where θ_z is the sun's zenith angle, α_{SAZ} is the sun's azimuth angle, α_{SurfAZ} is the surface azimuth of the PV-array (from north = 0°), and β is the surface tilt of the PV array.

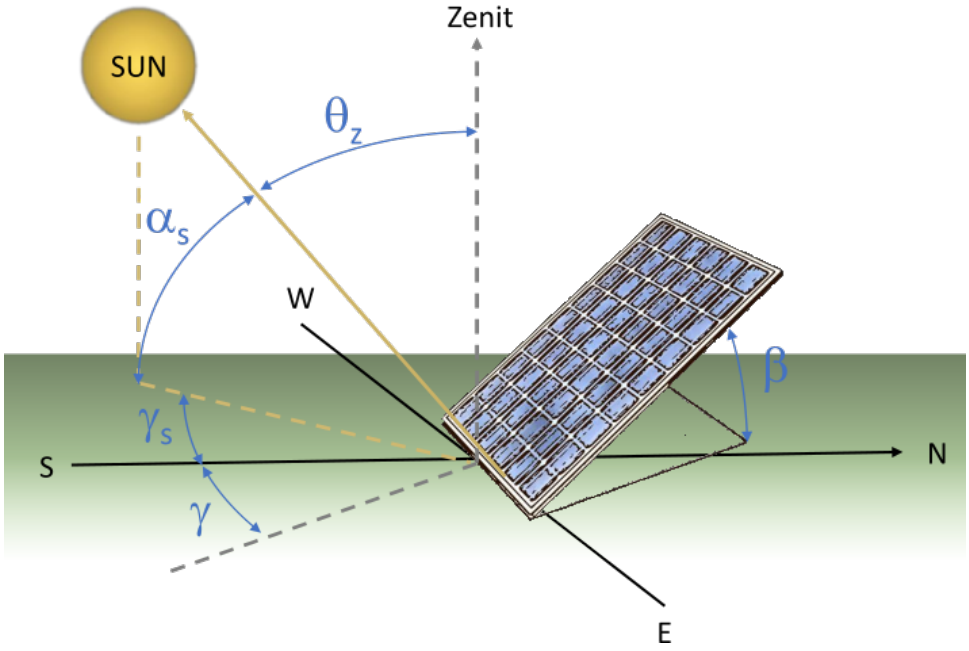

Figure 3.2: Angles involved in the calculation of incident irradiance into a tilted surface.

The general problem of calculation of the radiation on tilted surfaces has been addressed by several authors since a long time and has been thoroughly reported in several proposed models [20][8][21][22]. The differences resides mainly in the way the diffuse terms are treated.

E_{diff} corresponds to the diffuse sky irradiance. Simplified models consider the sky as an isotropic source with a 180° divergence angle to calculate the POA contribution of diffuse sunlight. However, diffuse radiation is not uniform over the sky, particularly in the regions near the solar disk and near the horizon, which are brighter. As a more complex model, the Perez Sky divides the diffuse radiation into isotropic, circumsolar and horizon brightening diffuse components [23], and it estimates the POA diffuse irradiance as a combination of these components:

$$E_{diff} = DHI \times \left(\frac{1+\cos\beta}{2}\right)(1-F_1) + F_1\frac{cos\theta}{cos\theta_z} + F_2 sin\beta \tag{3.4}$$

F1 and F2 are related to sky irradiance conditions, which are described using three variables: 1) the sun position (θ_z) 2) the sky clearness index ϵ, and 3) the brightness index Δ.The sky clearness index ϵ is defined as,

$$\epsilon = \frac{(DHI + DNI)/DHI + k \times \theta_z^3}{1 + k \times \theta_z^3} \tag{3.5}$$

ϵ expresses the transition from totally overcast sky (ϵ =1) to low turbidity (ϵ >6). For the model ϵ is separated into eight bins. To represent the opacity (thickness) of the clouds the sky brightening index Δ is defined as:

$$\Delta = \frac{DHI \times AM}{G_{ext}} \tag{3.6}$$

Where AM is the air mass and G_{ext} is the extraterrestrial irradiance [W/m²].

For different bins of ϵ (found in [24]), the brightness coefficients F1 and F2 are considered linear functions of θ_z and Δ

$$F_1 = f_{11}(\epsilon) + \Delta f_{12}(\epsilon) + \theta_z f_{13}(\epsilon) \tag{3.7}$$

$$F_2 = f_{21}(\epsilon) + \Delta f_{22}(\epsilon) + \theta_z f_{23}(\epsilon) \tag{3.8}$$

This diffuse model has become the standard model for the calculation of the diffuse daylighting contribution to the POA incident irradiance. Its accuracy has been previously compared [23].

According to an isotropic model, the ground reflected irradiance component $E_{ground,refl}$ can be calculated as a function of the GHI incident on a diffuse reflective ground (assumed as GHI for an unshaded area), the albedo coefficient of the ground ρ and the view factor assuming a infinitely long array surface.

$$E_{ground,refl} = GHI \times \rho \times \frac{1 - cos(\theta_\beta)}{2} \tag{3.9}$$

For the calculation of the incident rear irradiance, the $E_{ground,refl}$ component considers the shaded and unshaded areas of the ground between arrays by discretizing (meshing) the ground and PV modules of the array.

3.1.1 Bifacial rear irradiance models

The gain from a bifacial installation comes mainly from the capacity to produce electrical power from the back side of the PV module. Consequently, the calculation of the rear incident irradiance is of significant relevance. The rear irradiance on a bifacial PV module is obtained by calculating the three main irradiance components contributing to the total incident sunlight as described in equation 3.1 in the previous section, i.e., the direct, diffuse, and ground reflected irradiances reaching the backside. Two principal methodologies address the rear side irradiance modeling: view factors and ray tracing.

View Factor Models

Regarding view factors (VF), two-dimension (2D) and three-dimension (3D) approaches are possible.

3DVF

The view factor is defined as the fraction of the radiation that leaves a surface A_1 and is intercepted by another surface A_2. Consequently, this proportion is used to calculate the fraction of irradiance reflected from the surrounding surfaces to a collection point on a bifacial PV module. From the thermal radiation heat transfer theory, it can be derived the equation to calculate the view factor as in equation 3.10 [25] .

$$VF_{A_1 \to A_2} = \frac{1}{A_1} \int_{A_1} \int_{A_2} \frac{\cos(\theta_1)\cos(\theta_2)}{\pi R^2} \, dA_1 \, dA_2 \tag{3.10}$$

Where R is the distance from the center of A1 to the center of A2. θ_1 and θ_2 are the angles between R and the normal vectors n_1 and n_2 respectively as shown in Figure 3.3

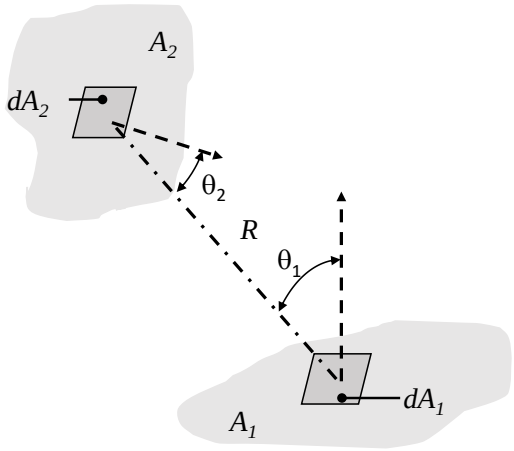

Figure 3.3: Representation of elemental areas and angles implicated in the calculation of a view factor between two surfaces.

The view factors, also called configuration factors, have been applied to model the irradiance at the rear surface of solar modules as in [26][27][28], and they also have been implemented in the PVsyst software [29]. View factors have two important relationships, known as the summation and reciprocity rules.

The summation rule states that the view factor between surface element dA_1 and the surface A_2 ($VF_{dA_1 \to A_2}$) is equal to the sum of all view factors between dA_1 and each surface element dA_2 of A_2. In the case the surface A_2 constitutes the whole field of view of the surface element dA_1, then $VF_{dA_1 \to A_2}$ is equal to one. The reciprocity rule states that the view factor between A_1 and A_2 ($VF_{A_1 \to A_2}$) is equal to the view factor between A_2 and A_1 ($VF_{A_2 \to A_1}$).

As mentioned in the previous section, the irradiance received by a photovoltaic module surface is composed of the beam, direct and ground-reflected irradiances. The backside incident irradiance is calculated by equation 3.2 considering θ_{AOI} from the backside surface as follows:

$$I_{beam} = DNI \times \cos(\theta_{AOI}) or I_{beam} = B_h \times \frac{\cos(\theta_{AOI})}{\cos\theta_z} \tag{3.11}$$

Being B_h, the direct irradiance component over a horizontal surface.

The contribution of the diffuse solar irradiance in the total incident solar irradiance on the rear POA will be equal to the diffuse irradiance coming from the sky that has not been obstructed by any obstacle. Thus, solar diffuse irradiance reaching the back side of the PV arrays depends of the surroundings. For a non edge located PV array, the diffuse incident irradiance is calculated according to the summation rule by,

$$I_{diff} = DHI \times \left(\frac{1 - cos(\theta_\beta)}{2} - \sum VF_{obstacle_i} \right) \tag{3.12}$$

Where, I_{diff} is the contribution of diffuse irradiance to the total incident rear POA, $1 - cos(\theta_\beta)/2$ is the sky VF relative to the tilted angle, and the summation term references the obstacles over the horizon that obstruct the diffuse irradiance from the point of view of the considered rear surface of the PV array (accounted by the $VF_{obstacles}$).

The irradiance reflected by the ground incident on the rear surface of the PV array, is determined by the conditions of illumination of the ground, i.e. the DHI component reflected from shaded areas and the DNI plus the DHI from non shaded areas. In this way, the incident irradiance can be calculated according to the following equation:

$$I_{refl} = VF_{ground\_to\_module} \times (DHI + Bh) \times \rho \tag{3.13}$$

Where ρ being the albedo of the ground surface, GHI, the global horizontal irradiance, $VF_{gtomodule}$ the ground to module view factor and DHI, the diffuse horizontal irradiance.

As a geometrical relationship, the VF is calculated between all the elements of each implicated surface. In the INES-TriFactors tool, the rear irradiance is calculated for each element along the row length of the bifacial PV array by using the equation 3.13. This way, the spatial distribution of irradiance is inherently obtained along a finite PV array surface for a defined timestamp. This enables to consider the edge effect, which occurs when the bifacial PV cells at the edge of a bifacial module have higher rear irradiance than the ones in the center. Nevertheless, the calculation of VF has to be done every time the geometry is defined, i.e. for a tracking system simulation the VF must be calculated for every inclination or timestamp. Depending on the system and meshing size of the surfaces, the simulation time can last several hours on a standard computer to achieve a hourly annual simulation, making it impractical or inconvenient for daily use or for sensitivity studies.Thus, when simulating large scale PV plants with a large number of rows and a simple geometry (i.e. where edge effects will have a low weight in the irradiance calculation), a simplified optical model based on a 2D view factor may be preferred for being implemented along with the TriFactors tool. This is the method that is implemented in PVsyst tool.

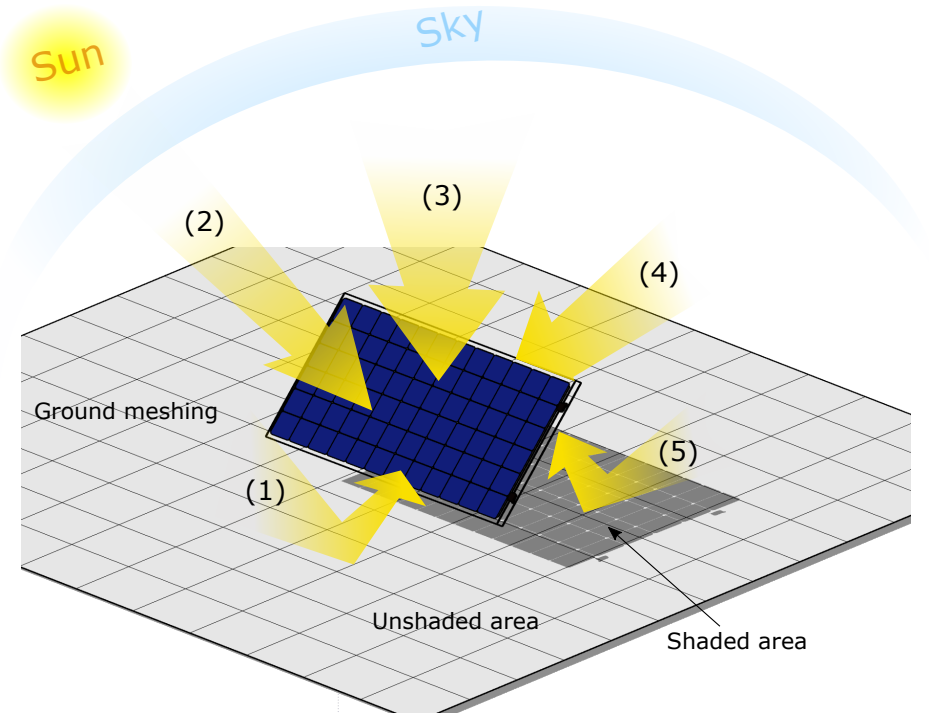

Figure 3.4: Representation of the scene for 3D view factors and outline of calculated irradiance components incident over the PV module surface. (1) ground reflected irradiance, (2) Direct irradiance, (3) isotropic sky diffuse irradiance, (4) backside incident irradiance, (5) shaded ground reflected irradiance. The meshing of the ground surface is represented by the grid on surface beneath the PV module.

2D View Factor

In the simplified 2D model the PV arrays are fully described in a two-dimensional cross section of the rows, as shown in figure XX. The rows of PV modules have all the same orientation and are equally spaced but unlike a 3DVF approach no interspace between modules is possible, and thus no edge effect is possible to take into account. This approximation offers a better response for long regular rows as in large scale ground mounted PV installations, or flat rooftop commercial installations. This make this method very efficient in terms of the computation cost due to its simplicity. In fact, annual simulations can be run in a few seconds. This method has been used by other authors [30],[31],[32] and PVsyst[29]. Nonetheless, these assumptions cast some doubt on their applicability for certain system types. The inability to model the third dimension, means a consistent irradiance along the PV rows, this might be a fair assumption for large PV plants, but it has been assumed that it may induce higher errors for smaller system, this will be discussed in 5.

From the definition of the radiosity, in [28] a linear system of equations, is proposed to calculate the incident irradiance on each surface i of the enclosure system to be modeled. The dimension of the system of equations is given by the number of surfaces n. As a radiative flux, the termed radiosity accounts for all the radiant energy leaving a surface. It accounts for radiation leaving in all directions, and is related to the emitted and reflected radiation, $q_{e,i}$ and $q_{r,i}$ respectively, by the equation 3.14

$$q_{o,i} = q_{e,i} + q_{r,i} \tag{3.14}$$

In a practical case, the $q_{e,i}$ can be neglected for the spectral range of interest for the PV devices operation [300-1100]nm. Additionaly, considering the albedo ρ_i of the surface i, $q_{r,i}$ can be determined as,

$$q_{r,i} = \rho_i \times q_{in,i} \tag{3.15}$$

Where $q_{in,i}$ is the incident irradiance on surface i. Thus, the radiative flux outgoing from surface i is represented by,

$$q_{r,i} = \rho_i \times \left(\sum_j q_{o,j} \times VF_{i,j} + Irr_i \right) \tag{3.16}$$

The first term of the addition in equation 3.16, represents the irradiance contribution from all the surfaces j surrounding i incident onto surface i, i.e., the contributions of the sky dome, the ground surfaces and the others PV rows to the front of the next one. $VF_{i,j}$ stands for the view factor between surface i and j.

The second term corresponds to irradiance from sources not considered to be surfaces. In this thesis, this will be equal to the sum of direct, circumsolar, and horizon light components incident on the front surface of the modeled PV modules.

If accounting on the radiosity of all elements in the system to be modeled, we can get the matrix system of equations given in 3.17, in order to calculate the irradiance incident over all surfaces.

$$(\mathbf{R}^{-1} - \mathbf{F}) \times \mathbf{q_o} = \mathbf{Irr} \tag{3.17}$$

From here, it can be inferred that the irradiance $(\mathbf{Irr})$ is the difference between the overall incident irradiance on the surface, and the contribution of radiation from the surrounding surfaces.

As mentioned previously, in bifacial PV systems the modules on the edges usually receive more irradiance due to larger unshaded areas (edge effect), therefore since 2D models assume to have the same ground shading impact for all the modules along the rows, this effect cannot be captured. Similar to the 3D VF approach, another downside of this model is the difficulty in modeling the supporting structure and the irregular geometries, which could impact the incident backside irradiance.

Ray Tracing

Ray tracing is a technique commonly used in computer graphics for rendering images. The core of a ray tracer is to project a certain number of rays through pixels into a computer-generated scene and compute what is seen in the direction of those rays. There are two ways for implementing ray tracing: forward ray tracing and backward ray tracing. Forward ray tracing is the most common method. In this method, the rays are traced in a way the photons will travel from the origin of the light source into the scene until reaching the point of view. Since a small fraction of the traced rays contributes to the final rendered image this method can be very inefficient although very accurate. In the other hand, in backward ray

tracing, the path of rays is traced from the objects in the scene to find any interaction with a light source. This method can reduce the simulation time significantly, because only the contributing rays are computed.

The 3D nature of ray tracing methods allows to reproduce complex scenes so that the non-uniformity and the impact of racking on the rear irradiance as well as the edge effects can be taken into account when simulating a PV plant.

The main disadvantage of the ray tracing method is the cost in terms of computational resources. Depending on the amount of rays and scene complexity, it may take from some minutes to several hours to recreate the real illumination conditions for a given duration simulation.

Ray tracing engines have been implemented and utilized for irradiance modeling in several softwares such as Comsol Multiphysics, Honeybee under Rhino and Grasshopper functionalities, but some of them have been developed specifically for photovoltaic systems modeling, such as:

- SunSolve by PV Lighthouse [33]
- EDF ray tracing model [34]

Radiance is an open-source software tool kit developed by Ward and Shakespeare [35] to render physically based computer images by backward ray-tracing algorithm. The software was originally developed for a use in architectural lighting analyses. Different material properties can be defined within scene elements in order to better represent the light interactions in the scene.

To recreate a real scene using the Radiance ray tracing tool, it is necessary to understand various complex commands and operations [36]. The National Renewable Energy Laboratory (NREL) has developed a bifacial specific wrapper functions based on the python language programming, to assist the use of Radiance found in a package called Bifacial_Radiance and has been previously benchmarked [37],[38]. In this thesis, we adapted some of these functions in order to simulate a PV plant on a high-performance computer. The simulation flow is described as follows:

First, the geometries representing the objects within the scene describing the PV plant are created using the built in tool and converted to a readable Radiance .rad files.

The calculation of the sky distribution is based on an angular distribution of the direct and diffuse lights. In Radiance the sky files (.RAD) can be generated by means of the $gendaylit$ function, which allows the generation of a sky distribution for each timestep of the meteorological year data used as input for the DNI and DHI. Another way to calculate the sky luminance is by means of the "cumulative" sky, where the semi-sphere is divided into several patches, so that each patch gets assigned a radiance value in a way that it can model the sky luminance for a period of time by adding up every timestamp. This method can be utilized to downsize the computation time significantly, but reducing the accuracy of simulation. The diffuse angular distribution is calculated using the Perez All-Weather Sky Model mentioned in the previous section 3.1.

All the previous RAD files are combined to create a mesh octree for each time stamp.

By using the "rtrace" command the rays are now traced from the points or coordinates on the modules previously defined in order to calculate the irradiance incident on them.

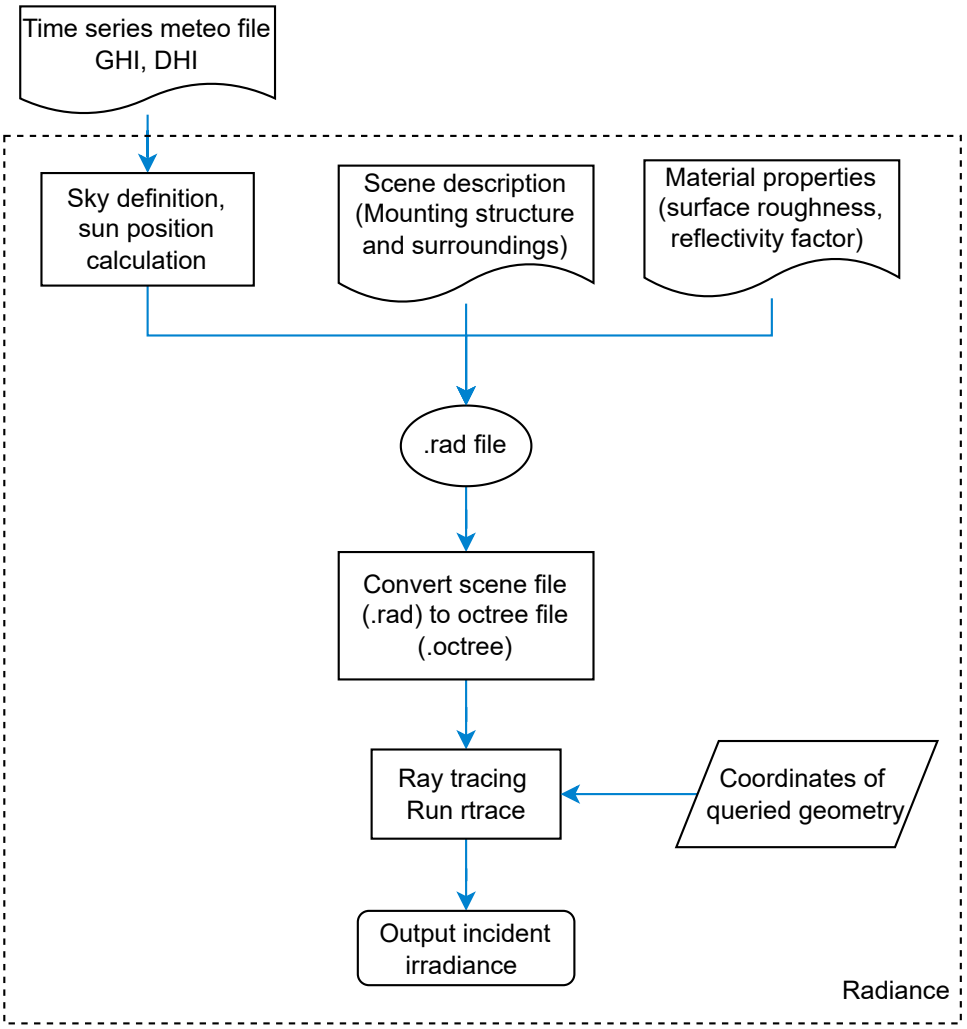

Figure 3.5: Flowchart for running bifacial irradiance simulations using RADIANCE.

3.2 Thermal Model

As based on semiconductors, solar cells performance will be determined by its temperature of operation. The instantaneous module temperature is a function of air temperature, wind speed, incident irradiance, and module materials. Therefore, the installation conditions will determine how these factors will affect the temperature of the modules. The open-circuit voltage of a module decreases significantly with the increasing module temperature and the short circuit current increases slightly with increasing temperature. Nonetheless, as mentioned in section 2.4.1 a solar cell can be a composition of different materials or semiconductors depending on its topology. Thus, the cell temperature may be different from one cell topology to another under the same operating conditions. These differences are demonstrated by the temperature factors calculated under laboratory conditions for each technology in table 3.1.

	PERC+	nPERT	HET	PERC
TkI (%/°C)	0.041	0.048	0.03	0.04
TkU (%/°C)	-0.28	-0.3	-0.23	-0.31

Table 3.1: Temperature coefficients determined at indoor conditions of different bifacial modules technologies and a monofacial module introduced in section 2.4.1.

As previously mentioned some technologies may have lower coefficients of temperature, as the case of HJT technology, so this have to be taken into account when modeling a specific bifacial module temperature. The module temperature is commonly estimated by using a steady state models. These models assume steady state condition and all the parameters related to the thermo-physical properties of the module material are combined together as one or more modelling parameters. The most knwon steady state models are the nominal operating cell temperature (NOCT) [39], the Sandia module temperature model [40] and the Fainman model [41]. The latter two take into account wind speed and the installation conditions by means of experimental factors. In particular, based on the steady state Whillier–Bliss equation used for flat plate solar thermal temperature analysis [reference], the Faiman model has been adapted for modeling the temperature of bifacial modules. It has also been used by PVSyst [29], and has been included in a recent comprehensive study of bifacial modules temperature modeling [42] where the Faiman model showed the lower deviation from measured data compared to other six models. It is based on two heat transfer coefficients to take into account influence of wind speed and mounting. The modeling equation is given as follows:

$$T_m = T_{amb} \frac{E_{POA}}{U_0 + U_1 \times WS} \tag{3.18}$$

Where, the E_{POA} is defined as:

$$E_{POA} = \alpha_f \times E_{front} \times \eta_f + \alpha_r \times E_{rear} \times \eta_f \times \phi_\eta \tag{3.19}$$

α_f: The absorptance of the front module surface.
α_r: The absorptance of the rear module surface.
Some common values are defined for monofacial and bifacial modules [43], for monofacial modules is 0.9 and for bifacial modules is 0.85.
η_f: The front side efficiency of the PV module.
U0: The constant heat transfer component (W/m²K).
U1: The convective heat transfer component (W.s/m^{3}K).
$\phi\eta$: The bifacial factor of the efficiency.
WS: The wind speed (m/s).

Values of U0 and U1 are suggested by Faiman[41]. Nontheless, these values can be also determined for specific mounting and module technology by fitting equation 3.19 to outdoor measured data of module temperature. In this work, by using the temperature measured along one year, this parameters where determined and compared between each bifacial technology as presented in section 5.2

3.3 Electrical Model

As depicted in Figure 3.1 the output from the optical and thermal model are input to the electrical model for finally determining the electrical output parameters of the PV module or system. The electrical characteristics of a PV device (i.e. semiconductor PN junction) can be mathematically represented by its equivalent circuit [44], which outputs the IV curve for given temperature and irradiance conditions of operation. As shown in figure 3.6, the single diode model (SDM) describes the output of a PV module by setting five parameters: the ideality factor n, the photocurrent I_{ph} (A), the diode reverse saturation current I_0 (A), the lumped parasitic series resistance R_s (Ω) and the shunt resistance R_{sh} (Ω). These are temperature dependent parameters.

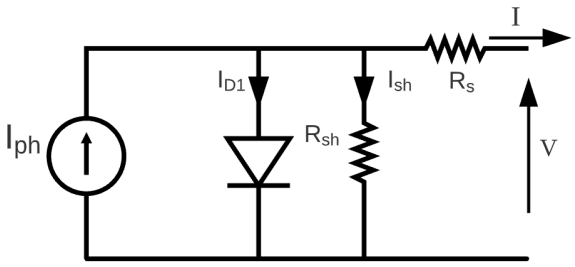

Figure 3.6: Equivalent single diode circuit model schematic based on five parameters.

This way, the PV module output can be expressed as a function $I = f(V)$ as in equation 3.20 or $P = f(V)$, for a given irradiance and temperature.

$$I(V) = I_{ph} - I_0 \left[\exp\left(\frac{V + I(V)R_s}{nV_t} \right) - 1 \right] - \frac{V + I(V)R_s}{R_{sh}} \tag{3.20}$$

Where, V_t is the thermal voltage depending on the cell temperature as $V_t = k \times T/q$, with k as the Boltzmann's constant (1.381×10^{-23} J/K) and q as the electron charge (1.602×10^{-19} C). T is the cell temperature (K).

Now, to find the optimum operating point of a PV system, as the maximum output power, we first need to calculate the characteristic IV curve for each independent PV element simulated in the network.As the in-field operation conditions vary from the STC, at which the manufacturer-provided parameters are established, it is required to determine all modeling electrical parameters simultaneously for the given POA irradiance and module temperature. In this dissertation, the calculation is based on a lumped-element PV model. As an approximation, the calculation of the modeling paremeters can be performed by using constant parameters of the solar cell estimated from the manufacturer's datasheet, which measured at STC, like open circuit voltage V_{oc}, short circuit current I_{sc}, maximum power point voltage V_{mpp}, maximum power point current I_{mpp}, and from the environmental conditions, as done in Bishop [45], Singh, et al. [46], and De Soto et al. [18].

Particularly, Singh et al. proposed the calculation of the IV parameters of bifacial modules by using only front and rear PV module single-sided measurements under STC [46], i.e., by illuminating only one side of the module at a time. This methodology enables the estimation

of the bifacial short circuit current ($I_{sc,bi}$), open circuit voltage ($V_{oc,bi}$) and the fill factor (FF_{bi}) of a bifacial module based on the single-diode model.

In INES-TriFactors simulation tool, the Singh et al. method is implemented and slightly adapted to calculate the bifacial electrical output of a PV system based on the real (simulated) outdoor POA incident irradiance and modules temperature. For this, the single sided indoor measurements $(V_{oc,STC}, FF_{STC}, V_{oc,STC})$ for the front and rear side estimated at STC are firstly normalized to the temperature of operation (T_c) following the equations 3.21,3.22 and 3.23.

$$V_{oc,x} = V_{oc,STC,x}[1 + K_{Voc} \times (T_c - T_{STC})] \tag{3.21}$$

$$I_{sc,x} = I_{sc,STC,x}[1 + K_{Isc} \times (T_c - T_{STC})] \tag{3.22}$$

$$FF_x = FF_{STC,x} \times \frac{1 + K_{Pmpp} \times (T_c - T_{STC})}{(1 + K_{Voc} \times (T_c - T_{STC}))(1 + K_{Isc} \times (T_c - T_{STC}))} \tag{3.23}$$

Where $V_{oc,x}$, $I_{sc,x}$ are the temperature corrected parameters and x stands for front and rear. The bifacial current $(I_{sc,bi})$ is considered linear related to the incident irradiance on both faces, thus the bifacial current under real irradiance conditions can be calculated as a function of front and rear currents as follows,

$$I_{sc,bi} = \frac{Gf}{Gf_{STC}} I_{sc,f} + \frac{Gr}{Gr_{STC}} I_{sc,r} \tag{3.24}$$

Where the front $(I_{sc,f})$ and rear $(I_{sc,r})$ normalized short circuit currents are weighted by the front (Gf) and rear (Gr) incident irradiances respect to the corespondent indoor incident irradiance.

This way the bifacial gain factor to the front side, used for the calculation of the FF parameter, is defined as,

$$R_{Isc} = \frac{I_{sc,bi}}{I_{sc,f}} = \frac{Gf}{Gf_{STC}} + \frac{Gr}{Gr_{STC}} \frac{I_{sc,r}}{I_{sc,f}} \tag{3.25}$$

Accordingly, by using the above equations and following Singh et al., the bifacial output maximum power $(P_{mmp,bi})$ can be expressed by the equation 3.26. Since the Fill Factor (FF) is defined as $(I_{mpp} \times I_{mpp})/(V_{oc} \times I_{sc})$ as a measure of "squearness" of the IV curve, the $(P_{mpp,bi})$ can be determined from the above equations,

$$P_{mpp,bi} = FF_{bi} \times V_{oc,bi} \times I_{sc,bi} \tag{3.26}$$

Where FF_{bi} and $V_{oc,bi}$ are the fill factor and open circuit voltage respectively for a bifacial condition. The sequence for calculation of the $P_{mmp,bi}$ is described in the scheme in figure 3.7.

To avoid inconsistencies on the calculation of the bifacial parameters of the PV model due to the uncertainty of the measurements of single sided parameters used later as inputs, the optimum combination of the single sided (front and rear) measured parameters is evaluated by calculating the RMSE.

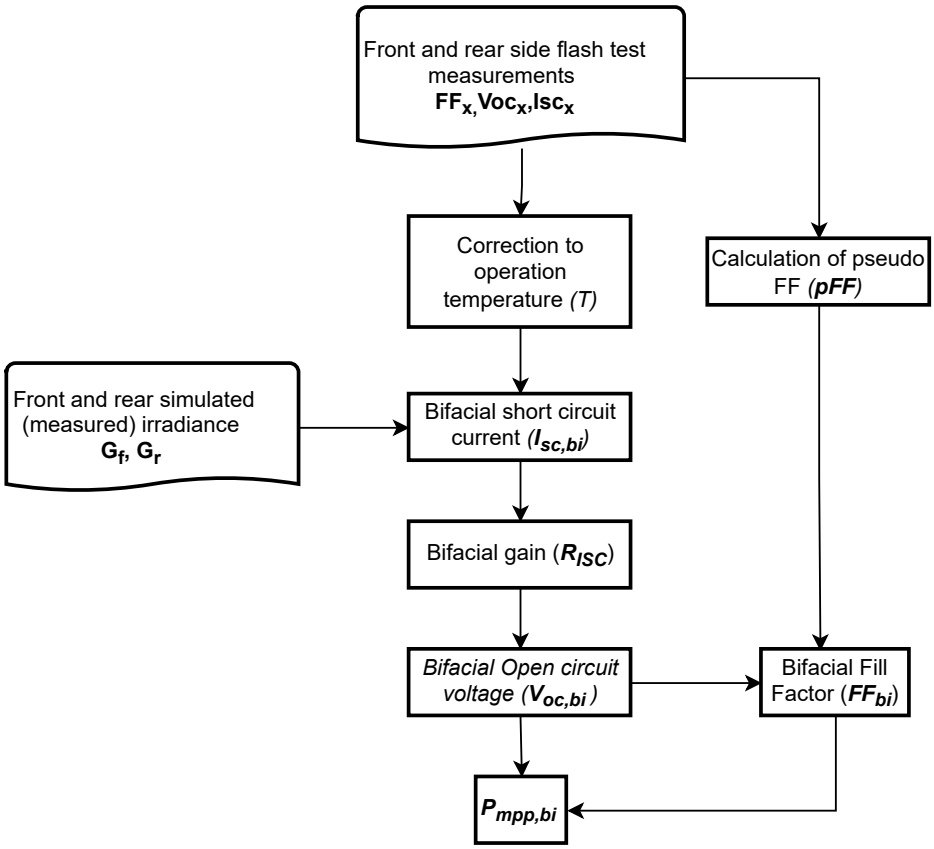

Figure 3.7: Determination of module output maximum power point P_{mpp} from module level single sided measurements at STC.

This methodology was validated by using the measurements from the fixed tilted test bench at the Plataforma Solar del Desierto de Atacama (PSDA), Chile, presented in the section 4.1 and comparing with the measured bifacial output DC power $Pmmp, bi$. The single sided measurements at STC from the PV module installed at the fixed test bench were passed to the algorithm. Five minutes time interval simulations were compared with measured outdoor $Pmmp, bi$.

The results show a strong dependence of the backside irradiance on the predicted power accuracy, as depicted in the Figures A.1.2 and A.1.3 in the Appendix. It was verified that the lower deviations were obtained for simulations with reference cells measurements placed at middle of the PV array. Nonetheless, when the irradiance used in the electrical model is based on the mean measured irradiance along the width of the array, this results in a modeled electrical power output closer to the measured power independently of the modules position on the array.

The accuracy of this method relies on having information of single sided measurements at different irradiances, which is not necessarily available or it cannot be retrieved with accuracy from manufacturer's datasheet.

Further improvements of the SDM are made by taking recombination effects into account. While the first diode models the recombination in the surface and other regions of the cell, the carrier-recombination losses in the depletion region are modeled by a second parallel diode, leading to the double-diode (DDM) equivalent circuit model shown in Figure 3.8. Where

usually the diode ideality factors, n_1 and n_2, are set to the values 1 and 2 respectively [47]. The two-diode model is considered as an accurate model under low irradiance conditions, nonetheless solving the equation of the two-diode defined by 7 unknown parameters is more complex than in case of the one diode model.

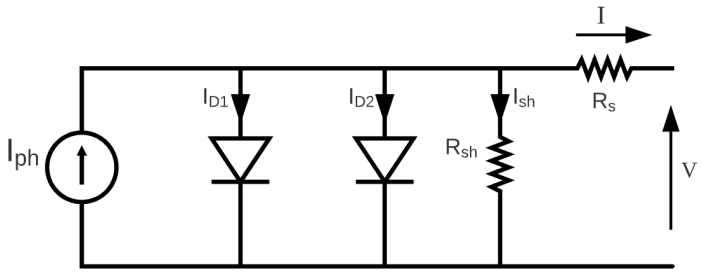

Figure 3.8: Equivalent double diode model schematic.

In Bishop [45] an additional term is introduced to the SDM for describing the operation in the second quadrant of the IV curve. A voltage controlled current generator is added in series to the shunt resistance in the SDM, this way the current through the shunting branch is described as in equation 3.27, thus equation 3.20 is modified as in 3.3.

$$M(V) = \left[1 + \alpha \times \left(1 - \frac{V + I(V) \times R_s}{V_{br}}\right)^{-m}\right] \tag{3.27}$$

Where V_{br} is the junction breakdown voltage (V), α is the fraction of the ohmic current involved in avalanche breakdown, and m is the avalanche breakdown exponent.

$$I(V) = I_{ph} - I_0 \left[\exp\left(\frac{V + I(V)R_s}{nV_t}\right) - 1\right] - \frac{V + I(V)R_s}{R_{sh}} \times \left[1 + \alpha \times \left(1 - \frac{V + I(V) \times R_s}{V_{br}}\right)^{-m}\right] \tag{3.28}$$

Based on the DDM, the PVMismatch [48][49] free open-source software allows for simulation in both forward and reverse bias IV curve regions and is implemented in this work for the electrical modeling of a bifacial system and further validated. As an object-oriented program the granularity level starts in the PV cells, for which its parameters of the cell level DDM are optimized from the initial module values from indoor measurements or manufacturers datasheet. The cells' IV curves are then combined according to Kirchhoff's circuit laws to form modules, strings, and full PV systems by adding either voltages or currents.This enables the calculation of the electrical output of a PV system based on the distribution of irradiance and temperature at cell level thereby to capture the backside non-uniformity in the bifacial PV module system simulation.

In fact, the previous methodology based on Singh method, outlined in the Figure 3.7 assumes that all PV cells within a cells string operate under the same irradiance and temperature. Naturally, under real conditions these assumptions are not hold, especially under inhomogeneous conditions of irradiance.

This inhomogeniety of front/back POA irradiances can be due to shadowing by objects around the PV field, self-shadowing, support structure obstruction of front or rear ground reflected irradiance or simply due to the radiation intensity gradient along the rear surface of a bifacial PV string. Under this mismatched conditions, the cells are driven to work at a negative voltage so it can be subjected to a temperature increase and, if repeated in time, permanent damage of the cell (hot spot). If a solar cell is biased at a strongly negative voltage (<-40V depending on solar cell technology) it can go through breakdown.

Accordingly, for the calculation of the electrical modeling parameters of the DDM and to adapt it for bifacial calculation, the parameters of the modules are used for the optimization algorithm as in implemented as follows. The non-linear functions in 3.29-3.32 give the current-voltage relationship corresponding to equivalent DDM circuit shown in Figure 3.8.

$$I_{ph} = I + I_{D1} + I_{D2} + I_{sh} \tag{3.29}$$

$$I_{D1} = I_{01}\left(\exp\left[\frac{V + R_s I}{n_1 V_t}\right] - 1\right) \tag{3.30}$$

$$I_{D2} = I_{02}\left(\exp\left[\frac{V + R_s I}{n_2 V_t}\right] - 1\right) \tag{3.31}$$

$$I_{sh} = \frac{V + R_s I}{R_{sh}} \tag{3.32}$$

Considering the conditions of operation at open circuit and short circuit voltage the non-linear system of equations in is set for the optimization of the parameters.

$$O = I + I_{D1} + I_{D2} + I_{sh}\Big|_{V=V_{oc};I=0} - I_{ph} \tag{3.33}$$

$$O = I + I_{D1} + I_{D2} + I_{sh}\Big|_{V=V_{mpp};I=I_{mpp}} - I_{ph} \tag{3.34}$$

$$0 = \left(I + \frac{\partial I}{\partial V}\right)\Big|_{V=V_{mpp};I=I_{mpp}} \tag{3.35}$$

$$0 = \frac{\partial I}{\partial V}\Big|_{V=0;I=I_{sc}} - R_{sh} \tag{3.36}$$

From the above equations it is possible to create the jacobian matrix for the optimization programming.

CHAPTER 4

Benchmarking and validation of bifacial PV irradiance models

Up to now, there is a few bifacial irradiance models available. However, the validation of the modeled bifacial performance with regard to the actual performance of fielded systems remains an ongoing task for the research centers collaborating with the PV industry [50]. Most of the validation studies have been conducted mainly in the USA and Europe.
As numerous bifacial model validation studies are published from sites around the globe, the expectations of PV buyers and investors regarding bifacial field performance become in better alignment with actual field performance. If such validations of bifacial simulations are found to be within acceptable agreement, this has the potential to reduce the risk of bifacial PV investments. A key aim of this study is to contribute to this ongoing bifacial performance model validation effort.
In this section, a few of the major bifacial irradiance modeling tools used to model real bifacial PV systems are compared. Irradiance measured by sensors at sites was compared with the simulated irradiance values to validate these models.

4.1 Fixed tilt

As a first study case the fixed installation for bifacial technologies testing at INES, France, was simulated. As shown in figure 4.1, the INES test installation consists of three south oriented rows in a 30° fixed tilted open rack with 0.80 m clearance height. Each row is composed of several small PV systems made up of about 12 modules in series. A reference cell facing ground is placed in the POA, attached at middle height on a tilted main steel supporting bar for every bifacial PV array.

Figure 4.1: INES fixed tilt test bench, France. Left) View of one of the three rows. Right) View from the backside of the first row enhancing the backside reference cell position.

We first performed a cross validation of the main currently available tools for modeling rear irradiance of different complexities. Five bifacial tools were tested (within commercially available and open source), including:

- bifacial_radiance (v0.2.1) as a ray tracing (RT) approach for two cases: with mounting structure or racking, and with no racking simulated (nr).
- bifacialvf (v0.1.7) 2DVF.
- pvfactors (v0.1.4) 2DVF.
- PVsyst (v6.8.1) commercially available 2DVF.
- TriFactors as a 3DVF.

They were used to simulate the back irradiance received by a reference cell placed facing ground at the INES fixed tilt test bench at the position closer to the edge (see figure 4.2), using measured weather data. For a first comparison, the results are presented as monthly accumulated irradiation for discussion in figure 4.3

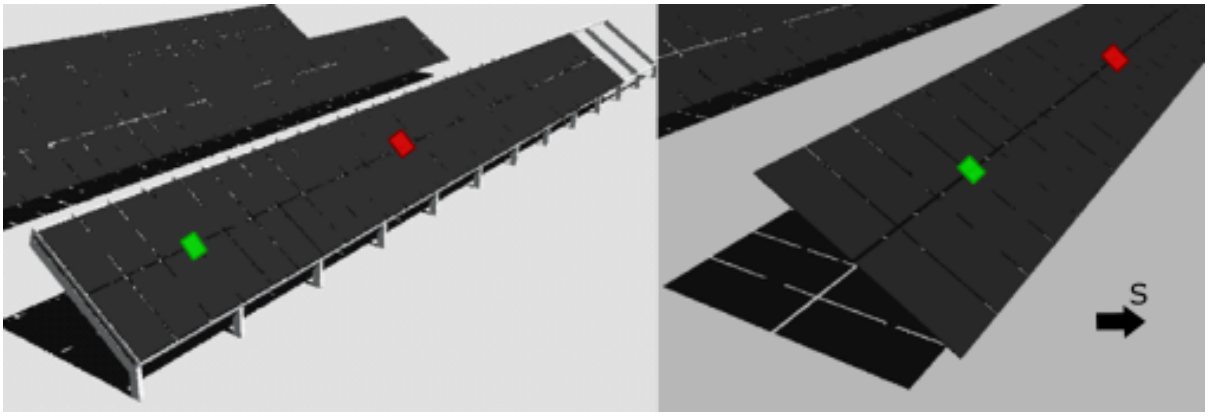

Figure 4.2: Rendered image of the fixed tilt test bench in CEA-INES considering racking (left) and with no racking in simulation (right). Closer to west edge position (green box) and centre position (red box) where measurements and simulation were performed.

As the main error indicators used for comparisons in this analysis, we use the root mean square error (RMSE) and the mean absolute error (NRMSE). The RMSE is an indicator proportional to the size of the squared error, and thus larger errors will have a large effect. A lower RMSE value means a better match to the measured data. Normalizing the RMSE (NRMSE) facilitates the comparison between results with different scales, in this case front and rearside simulations.

$$RMSE = \sqrt{\frac{1}{n}\sum_{i=1}^{n}(sim_i - meas_i)} \tag{4.1}$$

Where sim and $meas$ are the simulated and measured data, and n is the number of samples.

$$NRMSE = \frac{RMSE}{meas_{max} - meas_{min}} \tag{4.2}$$

where $meas_{max}$, $meas_{min}$ are the maximum and minimum value measured from the dataset.

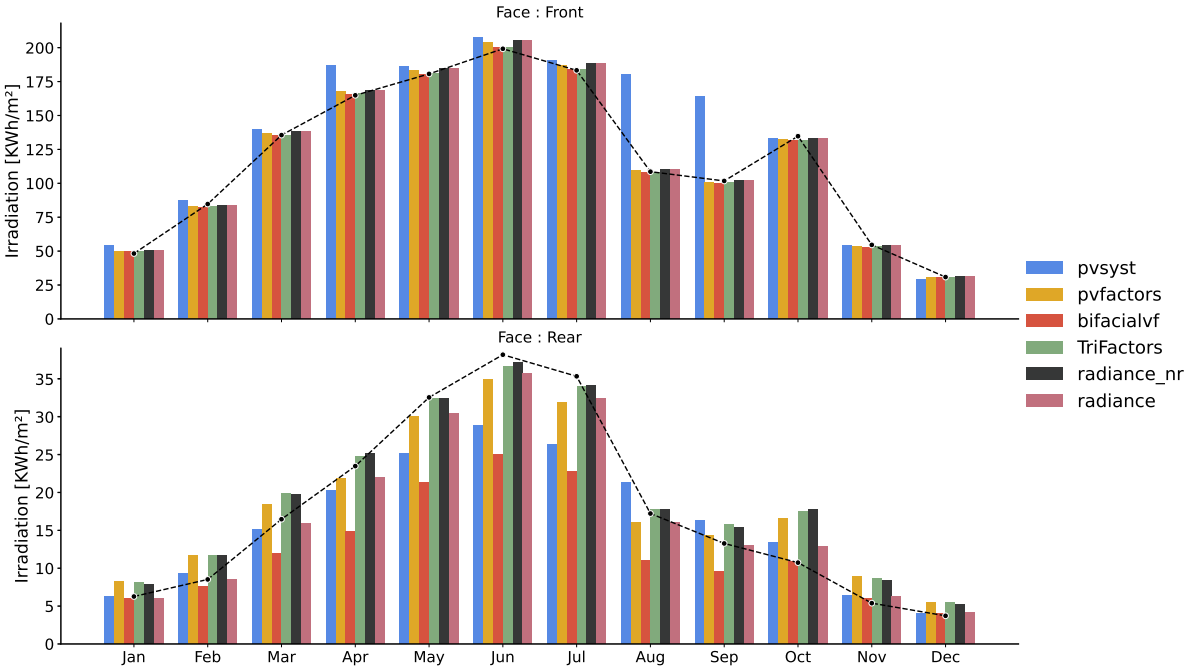

Figure 4.3: Crossvalidation results of the monthly irrradiation simulated by different irradiance models. Top: Front irradiation. Bottom: Backside irradiation. Dotted line: measured irradiation by the reference cell.

As expected, the simulation of the frontside incident irradiance seems to be achieved with almost the same accuracy by all simulation tools. It is worth noting the PVsyst results for the months of April, August and September where the model seems to overestimate the irradiation. However, this is due to the model estimation despite the lack of weather data. In fact, an annual mean deviation of 1.2 kWh/m² is obtained for the monthly frontside irradiation results, a rather low value when compared to the deviation of 2.9 kWh/m² calculated for the

backside irradiation results. Moreover, the larger deviation of simulated back irradiation (excluding months with missing data) was of 5 kWh/m² meaning a value above twice the frontside irradiation deviation found for the same period. These differences are mainly due to the complexity on the simulation of the backside incident irradiance. This is due to the presence of a larger number of surfaces involved in the calculation, such as the floor and other modules, as opposed to the simplicity of the frontside incident irradiance calculation.

Absolute differences of instantaneous irradiance in the order of 10 W/m² can be found even between results from tools using the same approach, as in the case of the 2D VF method. From this evaluation we found very accurate results, with different approaches when comparing simulated irradiation with the measured value throughout the day in a sub-hourly based time intervals, as it is the case for 3D VF and Ray tracing. The table 4.1 summarizes the results of one year comparison with the measured irradiance for a time interval of 5 minute. It shows the errors for the front and rearside simulation. In this analysis, PVsyst results are excluded since it is not possible to simulate with a smaller time step than one hour. Accordingly with the aforementioned, the errors observed for the frontside simulations are similar in each case, around 3.2 % and much lower compared to the rearside modeling results. However, it is for the rearside, due to the complexity of the calculations, where the errors can increase as high as 14.8 %, being the best result the one corresponding to the RT code considering the mounting structure with 4.6 % NRMSE.

From the RMSE values, we can observe that the values for the backside are smaller than the RMSE values for the frontside. Nonetheless, taking into account the amount of incident irradiance on each side, the relative error contribution is higher in the rearside compared to frontside.

On the other hand, it is possible to observe, that the 3D VF method implemented in TriFactors, obtains as good results as the RT method without mounting structure implemented in Radiance (radiance_nr), around 8% NRMSE. The mounting structure will influence the rear irradiance and its uniformity over the entire rear surface of the bifacial PV array. Non-uniformity of the rear irradiance can be a significant loss factor and will be studied in the next sections. The impact of racking on the performance of the simulation of the backside irradiance by each simulation tool, was evaluated at the test bench of CEA-INES by comparing the previous results at the position closer to the west edge of the PV row, with the measured and simulated rear irradiance at the POA in a position at the centre. Using ray tracing, the test bench is simulated with the mounting structure and without any structure, assuming free-floating panels, as shown in Figure 4.2. It was found that the influence of the mounting structure was the largest at the edge position. For the same period the differences between radiance with racking and the 3DVF approach are as similar as when comparing no racking and the 3DVF results, for the simulation at the inner position. This will be analyzed further in this section.

Table 4.1: RMSE of annual simulation validation of rear irradiance measured by a reference cell in a five minute time interval at INCA's platform.

	Front		Back	
	RMSE	NRMSE	RMSE	NRMSE
	W/m²	%	W/m²	%
pvfactors	41.1	3.2	19.9	10.2
bifacialvf	40.4	3.1	28.9	14.8
TriFactors	41.0	3.2	16.8	8.6
radiance_nr	41.0	3.2	16.5	8.4
radiance	41.0	3.2	9.1	4.6

These preliminary results need to be extended to different points over the back side of the PV array (i.e. not only at middle height of the array's width) and under different irradiance conditions. The previous results include seasonal variations as well as both cloudy and clear days. The impact on the accuracy of the simulation results can be subjected by the weather conditions. Accordingly, a further study was carried out considering the outperforming models of each approach: bifacial_radiance (v0.2.1), PVfactors (v0.1.4), and TriFactors. This study was extended by using these models to simulate the irradiance at the backside of the modules placed at the Plataforma Solar del Desierto de Atacama (PSDA), in Antofagasta, Chile.

Figure 4.4 shows the AtaMoS-Tec outdoor characterization test field installed at the PSDA (24.08°S and 69.92°W). Designed by the AtaMoS-Tec consortium and managed by the University of Antofagasta, the platform consists of 11 PV strings and 22 individually monitored modules, distributed along three different configurations: fixed tilt, vertical and tracking system.

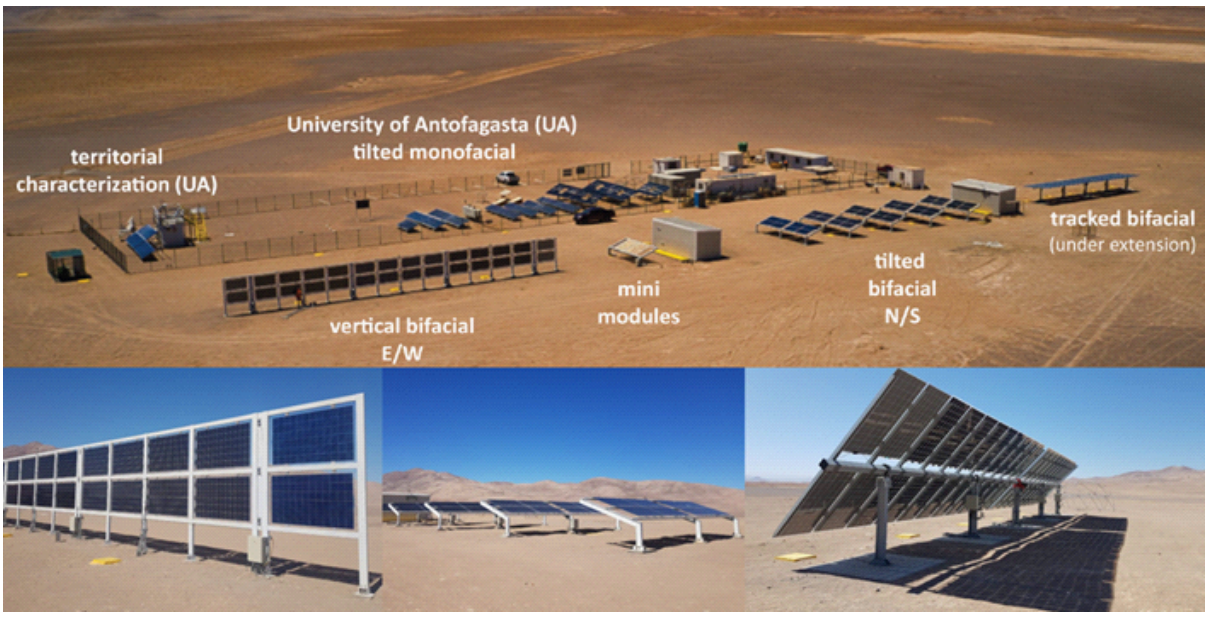

Figure 4.4: Top: Aerial view of the ATAMOS-TEC bifacial systems at the Plataforma Solar del Desierto de Atacama (PSDA) at the forefront. Bottom: left) Vertical PV array, middle) Fixed tilted array, right) single-axis tracker (HSAT)

The fixed tilt installation consists of five structures (see figure 4.5) and each one made of eight modules tilted at 20° facing north placed on 2 rows: each row of four modules long in a 2up landscape configuration, as represented in figure 4.5. In order to better understand the factors that affect bifacial PV systems performance, the testbeds at the PSDA are made up of various bifacial modules laminated with the aforementioned PV solar cell technologies (PERC+, HET, nPERT) spread over as to account with different bifacial technologies at each configuration (e.g. vertical, fixed and tracking). Therefore, at the fixed tilt installation we run three bifacial PV strings, and in addition a reference monofacial (PERC) string at the most southern position and a show-module string at the most northern position in order to account with same conditions of illuminance for the inner bifacial rows. All modules are of the same size and structure (glass-glass).

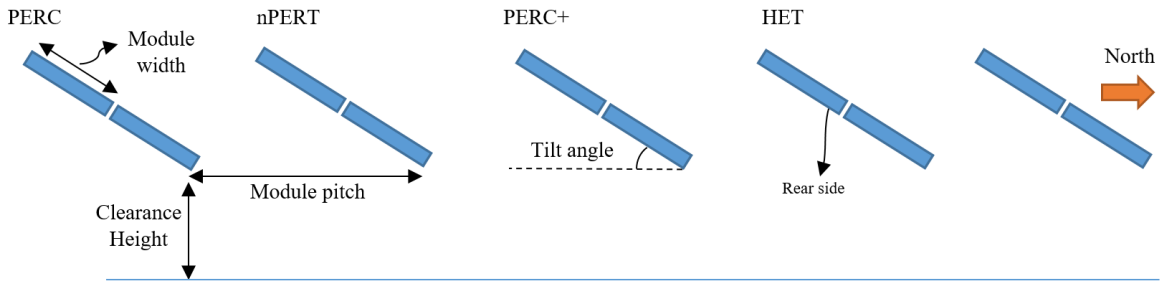

Figure 4.5: Schematic representation of bifacial modules distribution and the main geometrical parameters of the Fixed tilt north oriented ATAMOS-TEC test bench.

For monitoring the back incident irradiance, each row is equipped with three reference cells facing ground attached to the supporting bar in the middle of the row, along three different positions: top, middle and bottom. The front side irradiance was measured by means of three reference cells and a pyranometer.

Some modeling tools are capable of only hourly simulations (i.e. the minimum timestep is equal to 1 hour) like PVsyst, that is the reason why it was not kept in the further benchmark analysis as it might drive to less appropriate comparisons. The simulations shown here were performed by using bifacial radiance (v0.2.1), PVfactors (v0.1.4), and TriFactors with a five minute time step. Broadband measurements of the global horizontal irradiance (GHI), diffuse horizontal irradiance (DHI), direct normal irradiance (DNI) and albedo where collected by Kipp&Zonen thermopiles based sensors. The data were filtered according to the BSRN recommendations and resampled to a 5 minute time interval before input into simulations tools.

The general PV system configuration parameters passed as input to each simulation tool are the tilt angle, azimuth orientation, height, and measured albedo. Particularly for the RT simulations, the dimensions of the main mounting steel bars are considered as well as the thinner bars for mounting the modules.

When using the ray tracing approach it was possible to recreate a highly detailed scene of the tilted PV plant. We simulated the supporting structure and the objects around the installation in order to take into account the influence on the reflected irradiance and shading generated. Then, we calculated the irradiance at the same position as the one where the measurements were performed by simulating the irradiance reference cells at the corresponding

locations. Since a discretization of the PV surface is naturally given in a view factor approach (meshing of the backside module surface), we first compared the calculated rear irradiance at the closest mesh element to the corresponding measurement position.

Fig 4.6 shows the comparison between the measured and simulated irradiances for a five minute time interval on a sunny day like March, 21st 2020 and a partially cloudy day the February, 14th 2020 at each measurement point as a function of time.

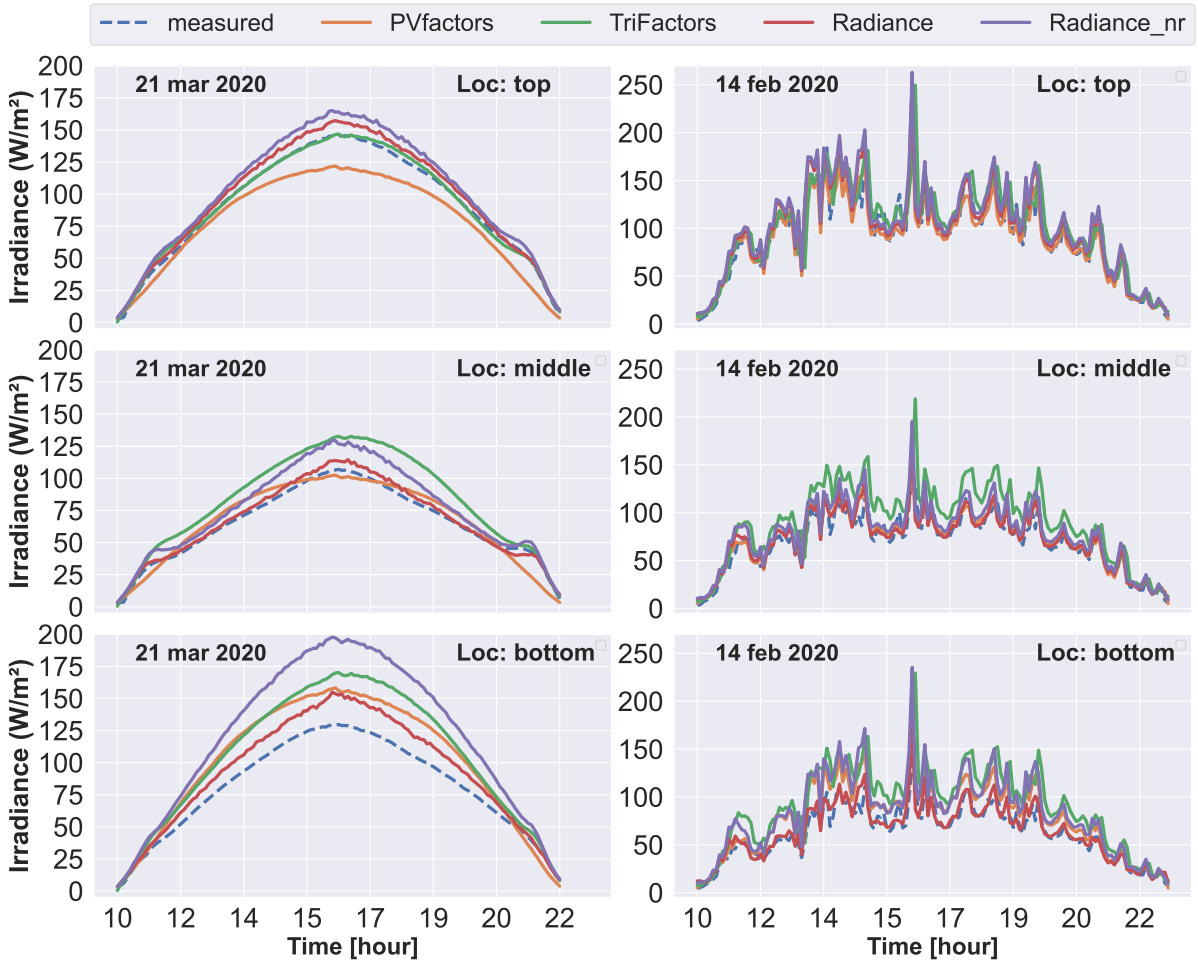

Figure 4.6: Simulated versus measured back irradiances at the top, middle and bottom measurement points.

As can be seen from Figure 4.6, the simulated back irradiance trend is well modeled by VF and RT over the day for both, partially cloudy and sunny day conditions when comparing to the measurements (dotted blue line). The differences between each simulation tool and measurements become more evident during a sunny day. 3DVF models better the back irradiance for a position at the upper extreme of the PV array, than RT. The result obtained through a VF2D approach is distinguished among the others for this position. This can be explained, since given the assumption of an infinite string, a much lower simulated irradiance is observed during midday due to the enhanced ground shading underneath of the infinite string. For this very reason, the RT and 3DVF approaches model better the back irradiance at early hours and at the end of the day (lower sun elevation angles). At these moments the

measured irradiance is boosted by the unshaded ground surface, so that a small hump is seen in the irradiance curve. This is well reproduced by the 3D VF and RT, but cannot be achieved by the infinite string assumption in the 2DVF approach.

When getting closer to the bottom extreme of the array, the difficulty of simulation becomes more evident. For the middle position the comparison between the back irradiance modeled by and RT (red solid line) and 2DVF (orange solid line) have shown a good match during all day long. However, around noon (when the irradiance is the highest) the 3DVF model yields higher back irradiance than the 2DVF and RT. Conversely, regardless of the method employed, an overestimated irradiance is obtained almost throughout the entire day for the bottom position. These results are summarised by the values of NRMSE shown in the table below. The higher discrepancies for the bottom position can be seen.

Table 4.2: Percentage values of NRMSE calculated for top, middle and bottom simulated back irradiance for a clear day (15 march 2020) and partially cloudy day (14 feb 2020).

	Clear day			Partially cloudy day		
	top	middle	bottom	top	middle	bottom
pvfactors	10.7	7.6	18.7	7.7	7.1	15.5
TriFactors	3.5	22.9	26.1	8.4	19.0	24.9
radiance_racktrue	5.1	4.1	10.8	8.6	7.4	7.2
radiance_norack	8.5	13.0	37.2	9.5	10.5	20.9

On the other hand, for a partly cloudy day, a discrepancy trend similar to that of a sunny day is observed. The largest deviations are also found for the bottom position. Nonetheless, the errors are slightly lower for all simulations methods compared to those on a sunny day. From table 4.2, it can be seen that 2DVF and RT approaches show similar performance for the middle and top positions, while the 3DVF approach follows the same discrepancy slope regarding the simulation position as found for the sunny day.

It can also be seen that including the support structure allows to reduce the error significantly. In fact, the error in the simulation for the bottom position is significantly reduced, i.e. 26.4% and 13.7% for a sunny and cloudy day respectively, by using the RT approach. The incident rear irradiance is influenced by light that slips through the supporting bars and is reflected by the ground to finally arrive to the cells on the rear side of the module. The shadow cast by the whole array gets is affected by the seasonal variation due to the maximal sun elevation angle.

When considering the data measured on the rear side, we observe that bottom, top and middle reference cells receive different irradiances and they vary strongly between winter and summer, i.e. the hierarchy between the most and the lowest irradiated position is changed. Somewhat counter-intuitively, the reference cell in the lowest position can measure about twice the irradiance measured by the cell in the top position. This can be explained by the shadow cast on the ground. The shadow gets further way back from the lowest module during winter and beneath the modules during summer for this location.

The extreme values of the sun's elevation are found between summer and winter (upper limit in summer and lower in winter) at the solstices, and in the middle during the equinox.

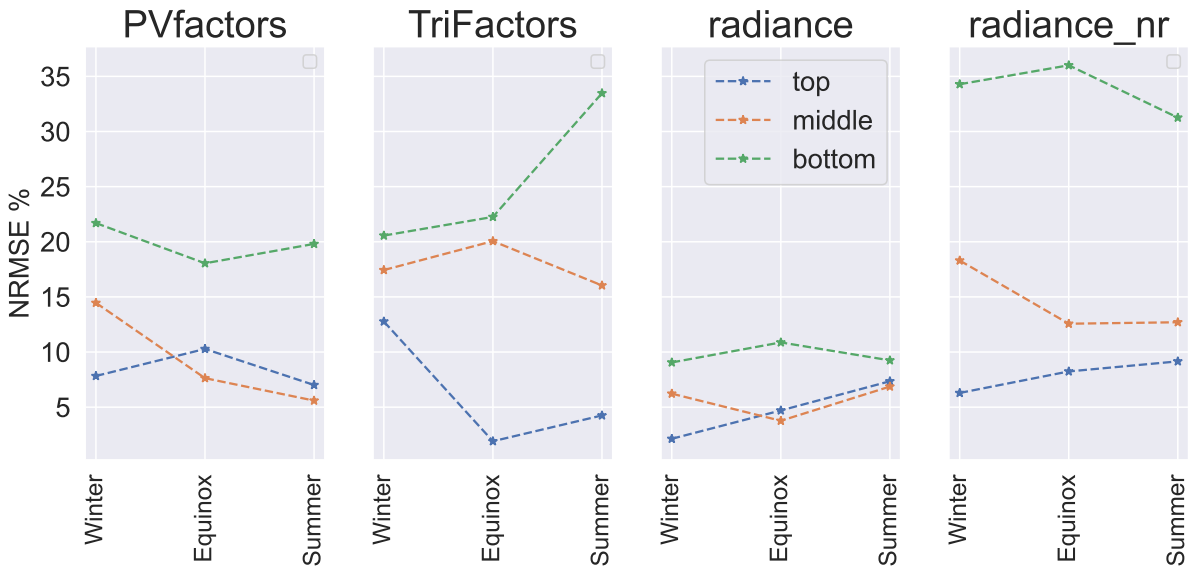

Figure 4.7: NRMSE by seasons

The results obtained for these extreme days are illustrated on Figure 4.7. When we look at the results for a single position we can see that the results will vary even with a 5% NRMSE of difference between seasons. The best results are found for the RT approach considering the supporting structure. The simulation error for the bottom position is the highest for all simulation tools and seasons. In fact, the maximum error value can be as high as 35% when no considering supporting structure, and can be as low as around 10% for all positions when simulating with a RT approach. It is possible to observe also that the results from the 2DVF approach for the top and middle positions are closer to those obtained with the RT considering the structure. These results will be explored further for a longer string as the case of the tracking system in the next section.

When comparing the simulated with locally measured irradiances we found that the precision of the simulation varies along the height (i.e. from bottom to top of structure) of the PV array. In bifacial photovoltaic systems, the irradiance received by the rear side is usually more inhomogeneous than the one on the front side (due to the surrounding environment and the PV array itself). After one year of measurement at the PSDA's fixed tilt test bench, we found that the bottom reference cell measured the highest values of irradiance (W/m^2) during the autumn and winter periods. On sunny days in winter time, the bottom irradiance can be up to 62% higher than the top measured back irradiance. Nonetheless, after one year of measurement, the top position registered the highest accumulated irradiation (Wh/m^2), e.g. 21 % more than the irradiation measured by the bottom reference cell (see Appendix A.2). This backside inhomogeneity effect induces a current mismatch between individual cells of the module increasing the power loss. A current challenge in bifacial modelling is to account for the spatial non-uniformity on the backside of the PV array. This subject will be addressed in the next chapter of this dissertation.

In Figure 4.8 a comparison of the modeled rear irradiance during one year where measured data are available along all the positions (top, middle, bottom) on the fixed tilt system is shown. The black line represent the unity to measurement.

The trend of all simulation tools agree well with the measurement for the top and middle

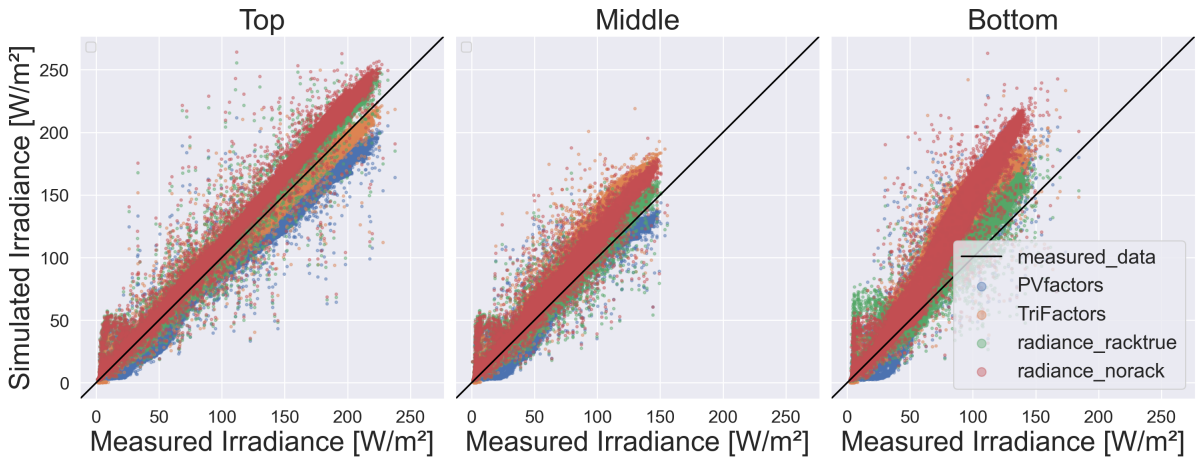

Figure 4.8: Rear simulated irradiance incident on the fixed tilt

position. The mean absolute error for radiance_norack, radiance_racktrue, TriFactors, PVfactors are summarized in Table 4.3. The lower deviations are found for the top and middle position for all the approaches. The 3DVF approach achieves the best results as indicated by the NRMSE value followed by the RT and 2DV methods. However, the error increases rapidly for the 3DVF method when simulating the irradiance at the middle and bottom positions. Although according to the MAE all methods tend to overestimate the measured irradiance, the best results are obtained by the RT and 2DVF methods for the middle and bottom positions.

Table 4.3: Percentage values of NRMSE and MAE calculated for top, middle and bottom simulated back irradiance during one year.

	Top		Middle		Bottom	
	MAE (W/m²)	NRMSE (%)	MAE (W/m²)	NRMSE (%)	MAE (W/m²)	NRMSE (%)
PVfactors	11.39	6.07	8.20	6.59	22.60	14.07
TriFactors	5.94	3.43	18.51	13.97	27.57	17.75
radiance_racktrue	8.00	4.81	5.53	4.89	10.41	7.21
radiance_norack	12.00	6.37	14.03	10.54	37.24	24.13

So far the methods show different values of NRMSE in the estimation of back irradiance depending mainly on the position along the width of the string, i.e. the closer to the ground the more difficult it is to obtain an accurate result regardless of the method used. This suggests that the performance of each approach may vary when considering the displacement of each point of the module with respect to the ground level, as is the case in a tracking system.

In the following section we evaluate the behavior of the irradiance on the backside of an HSAT and evaluate the simulation results with the POA tracking measurement.

4.2 Tracking system

4.2.1 Small Tracking PV system

As part of the first stage of the Atamos Tec project the monitoring of bifacial PV modules installed on a horizontal single axis tracking system (HSAT) was implemented and operated at the PSDA. As shown in figure 4.4, the single axis tracking system, SF7s (Soltec Spain), consists of a single row of 40 PV modules disposed in 2P configuration, i.e. 2 portrait module. The axis of the tracker is in the North-South direction, meaning that the modules are facing East in the morning and West in the afternoon. Given that in this first stage of the project we count only with a single row, there is no impact of neighbouring rows as it would be in a real industrial case. For monitoring the rear incident irradiance in a tracking system configuration, several reference cells are installed on the supporting bars facing the ground. We first evaluated the performance of the different simulations approaches by simulating the irradiance received by the eastmost, westmost and centered reference cells in the center position of the tracker. Figure 4.9 shows the individual reference cell positions and the Radiance rendered image.

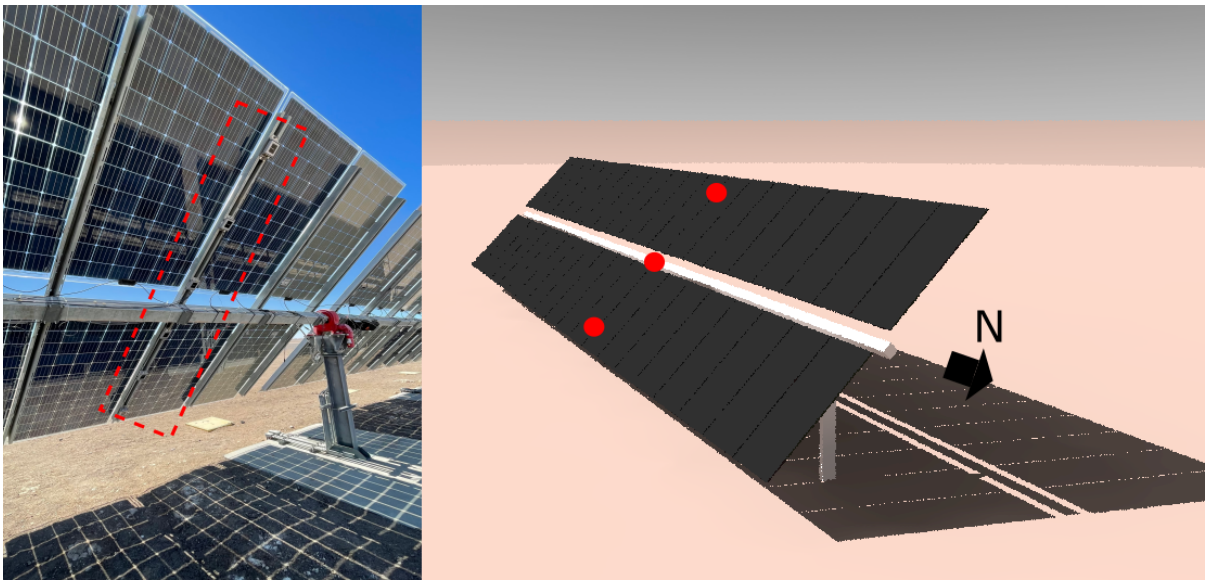

Figure 4.9: View of the reference cells at the single axis tracking system installed at the PSDA (left) and the Radiance rendered image (right). Red points represent the position where reference cells are placed.

First, a single simulation was performed during a sunny day, on February 21st, 2020. Figure 6.6 shows the comparison of the modeled backside irradiance to the reference cell measured data in the center position along the width of the tracker, according to Figure 4.9.

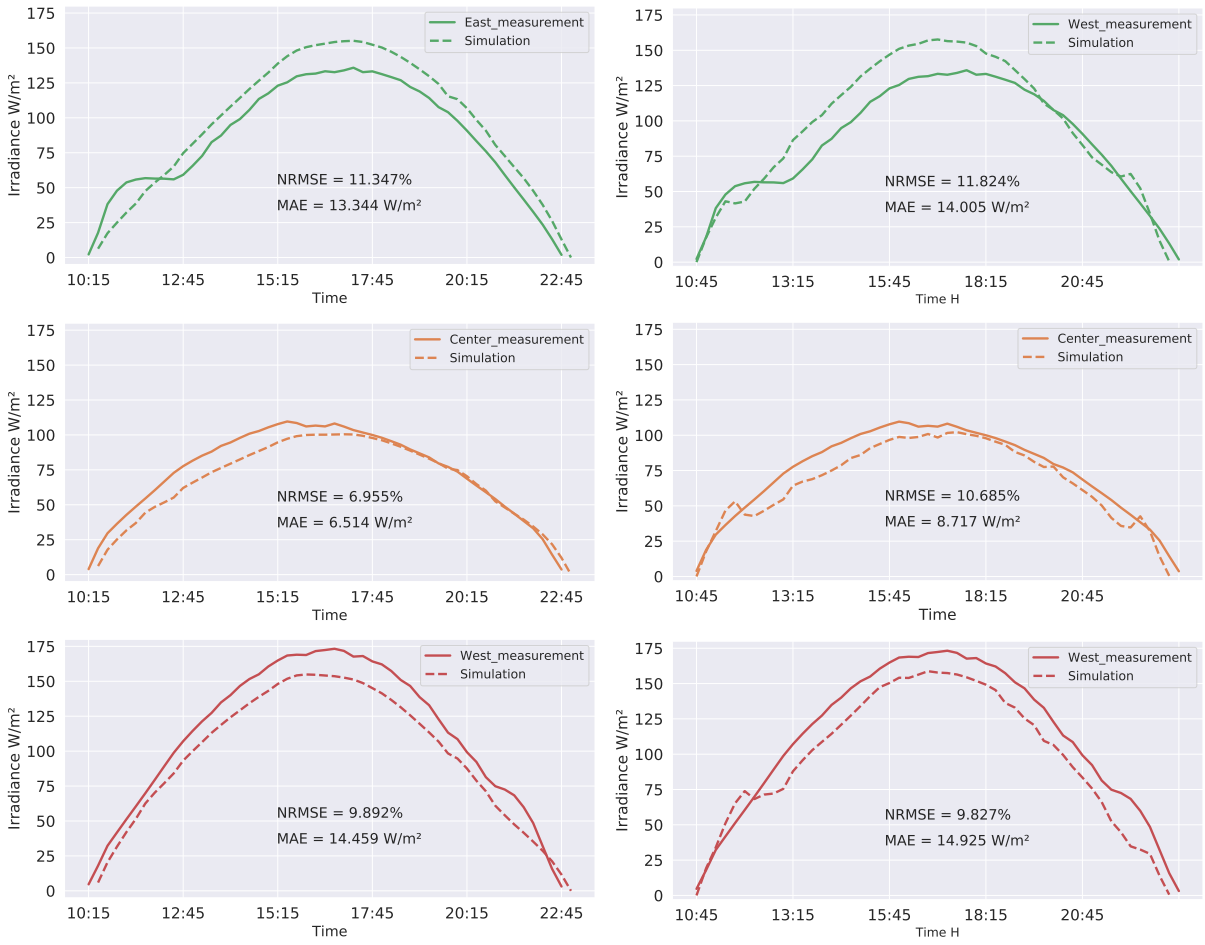

Figure 4.10: Modeled and measured irradiance in three different positions along the width in the center of the single-axis tracking system installed at the PSDA on February 21st, 2020. Left) 2D VF, Right) Ray tracing.

For the 3DVF calculation the time to perform a simulation is determined by the VF calculation, since the VF must be recalculated for each mesh element between ground surface and module for each inclination angle of the tracking system. Given that it is a version under development, the simulation of the tracking system by means of the 3DVF is not feasible and according the previous results the further study focuses on the 2DVF and RT tools. From the above Figure 6.6 it is observed that the localized resolved simulation results of the backside irradiance deviates by at least 7% NRMSE with the measured data curves curves especially for the eastern and western edge positions, where models underestimate or overestimate the irradiance along the day, respectively. These results are visible for both the view factor and ray tracing approaches. However, the VF model shows a lower NRMSE for the three positions simulated. This suggests a better performance of simulations in the center of the tracking systems as expected from an infinite row assumption algorithm for the case of the 2DVF approach, nonetheless a similar trend is obtained by RT.

Three reference cells were placed also at the most north and south positions of the tracking system. The Figure 4.11 shows the irradiance measured at solar noon during the whole year 2020 by the reference cells installed in the middle of each position along the tracker axis, i.e. north, center and south. As can be seen in the extreme north the difference increases

considerably from the summer months to reach a difference of over 20% compared to that measured in the center during the summer. This is mainly due to the southward displacement of the shadow cast by the tracker as the angle of elevation of the sun decreases as winter is attained, where its elevation is the minimum and the shadow cast at noon is the longest.

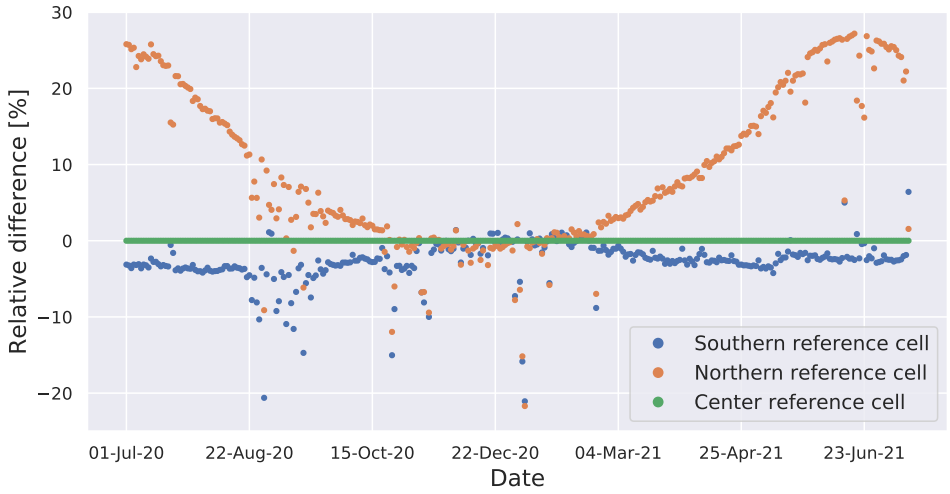

Figure 4.11: Yearly variation of irradiance regarding center position.

A slightly lower performance is observed when displacing the measurements points along the long of the tracking system, and calculating the rear irradiance at these extreme positions (North and South edges) as shown in Table 4.4.

Table 4.4: NRMSE of the single axis tracking system backside irradiance

		Along tracking axis		
	Location	North	Center	South
PVfactors	East	15.8%	11.3%	14.9%
	Center	8.6 %	7.0%	8.9%
	West	11.7%	9.9%	9.8%
Radiance	East	13.9%%	12.3%	11.8%
	Center	11.8%	10.7%	9.8%
	West	14.2%	13.5%	12.0%

Further investigation is required to understand the discrepancy between the modeled and measured data in this study. This difference may be due to the error in modeling reflectivity of the modules, or tracking angle simulation not available for this experiment.

We performed these simulations by considering the supporting structure (RT approach), and it resulted in a negligible impact on the reference cells backside irradiance simulation. In tracking systems, the shadow on the ground from the backside structure (horizontal axis and vertical pillars) is covered by the shadow casted by the modules themselves so there is a lower reduction of the reflected irradiance from the ground. Nonetheless, the supporting bars can reduce the reflected diffuse irradiance on the backside of bifacial modules.

During the year 2020, the rear irradiance was measured every minute while the tracker was operational, nontheless however, there were problems of data corruption and alterations that spanned a large period of the year. This data was filtered in a way to be compared to simulated irradiance. In Figure 4.12 the 2D VF and 3D RT models are compared to the rear irradiance values measured by the the three reference cells.Thus the rear irradiance is evaluated along the tracker width. When modeling with the 2D VF, the collector width of the tracker is meshed into 24 segments as for evaluating the rear irradiance at the position of the reference cells are placed.

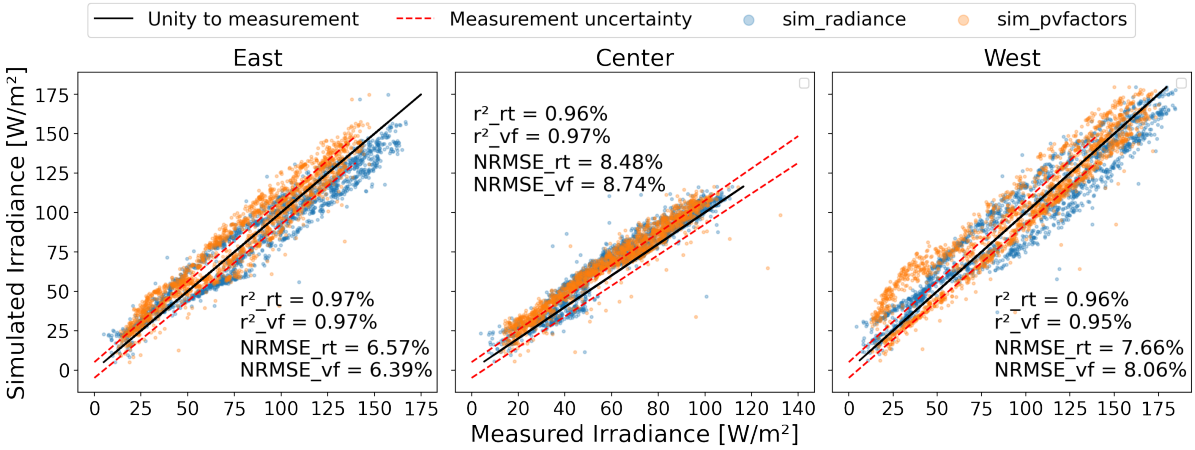

Figure 4.12: Correlation of the hourly measured and modeled irradiance at the three different positions (east, west, middle) in the center of the tracking at the PSDA according to 4.9.

The results shows a good correlation (over 0.96%) between hourly averaged measure and simulate bacside irradiance. Nonetheless, the values of NRMSE shows a similar deviations for the 2DVF and RT. Thus, there is not a significant difference between these method for the estimation of the localized irradiance at the west center and east center position of the tracker.
On the other hand the front irradiance values are mainly concentrated over the 800 W/m², since normally clear days are found at the PSDA. A higher dispersion can be seen for values below the 800 W/m² irradiance. This is due to the subestimation of the irradiance in the early morning and late afternoon mainly by the RT approach. We believe this are due to small differences in the simulated and real rotation angle of the tracker.

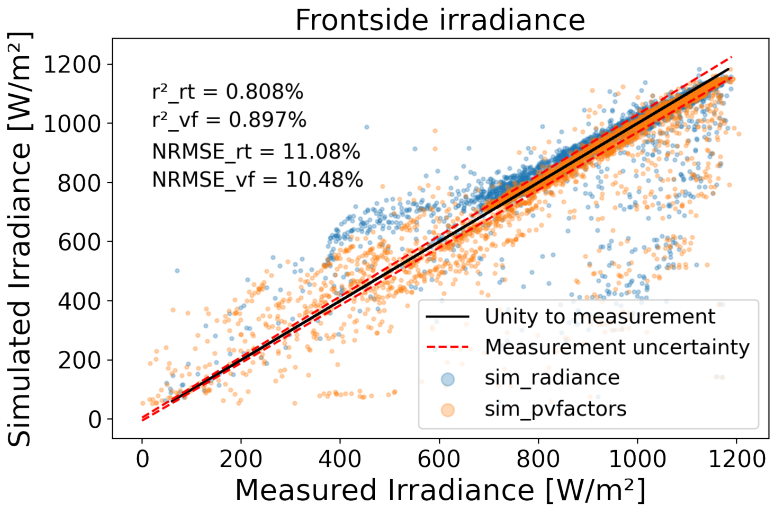

Figure 4.13: Correlation of the hourly measured and modeled frontside irradiance at the PSDA tracker POA.

4.3 Large scale tracking system

Lower values of GCR will imply higher rear irradiances due to a reduced self-shading effect. Since the HSAT installed during the first stage of the Atamos Tec project corresponds to a single system (i.e. without any other surrounding tracker), this study has to be extended to a large scale PV system.

For this, we account on the data from a large scale PV system installed in Wuhai, China, (coordinates 39.75°, 106.67°) provided by Canadian Solar inc.

The test field consists of two PV systems: a fixed 35° tilted south-facing system and a single axis tracking system, with both bifacial and monofacial 144 half-cells based modules each.

Thanks to lower resistive losses due to a reduced current and a better shading behaviour under certain conditions as mentioned in section 2.4.2, half-cell based modules are of great interest for an optimized production of electricity in large scale PV systems.

The monitored tracking system consists of 12 rows of trackers designed to support 18 modules in 1P configuration, i.e. one portrait module, as shown in Figure 4.14. The 12 rows are distributed to form 4 strings of 54 modules in series each. Both of bifacial and monofacial modules are made of polycrystalline half cells, and have a bifaciality factor of 70%. Power, V_{mpp} and I_{mpp} are measured every minute. An expanded uncertainty of 5% is estimated. The ground beneath both systems is natural sand, whereby a mean albedo of 26% was measured over 9 months by an albedometer installed on-site. For rear irradiance monitoring, five pyranometers are placed at three different positions along the width of the array and in two centered additional positions close to the edge of the tracker. Table 4.5 summarizes the parameters of the test field. We analyzed the data recorded from December 2018 to August 2019.

(a) Photograph of the PV tracking system installed at Wuhai, China. Photograph courtesy of Canadian Solar

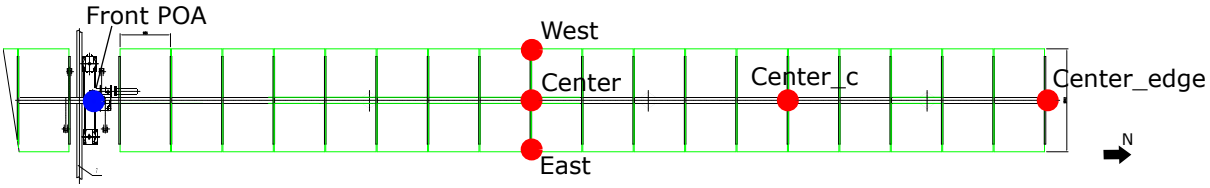

(b) Schematic of the position of each irradiance sensor installed on the tracking system for front and rear measurements. Courtesy: Canadian Solar

Figure 4.14: Large scale PV plant HSAT installed by Canadian Solar at Wuhai, China.

Table 4.5: Summary of geometrical configuration of HSAT system mounted in Wuhai,China.

HSAT PV system		Module	
Parameter	Value	Parameter	Value
Hub height	1.75	Module width (m)	1
Pitch	5.5	Module length (m)	2.12
Tracking angle range	55	Power bifaciality	0.7
Collector width (m)	2.12	Effciency front	17.54
GCR(%)	38		

Figure 4.15 shows the correlation plot of simulation for each position at the rear side of the tracking system.

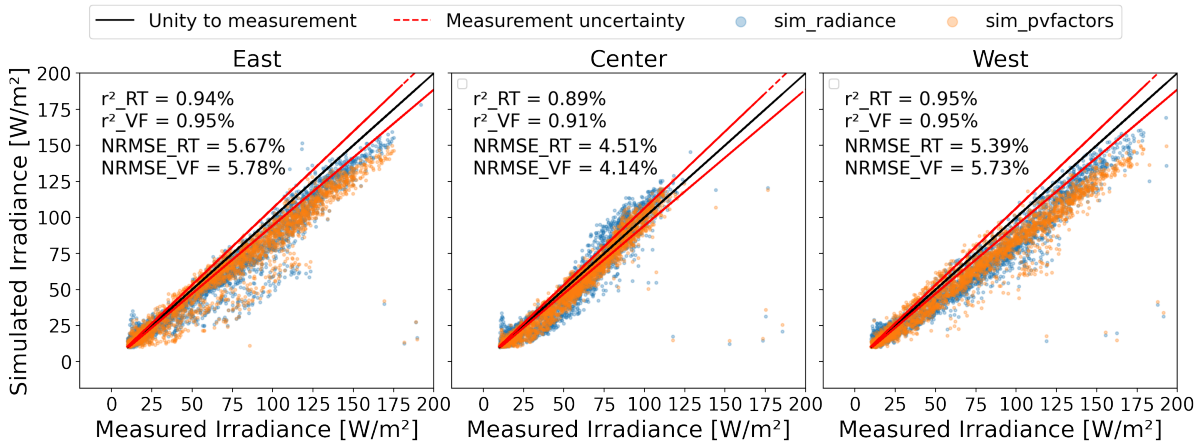

Figure 4.15: Correlation of the hourly measured and modeled irradiance at the three different positions (east, west, middle) in the center of the tracking at Wuhai, China, according to Figure 4.14.

It is possible to observe a greater dispersion of irradiance up to over 150 W/m² for the east and west positions. On the other hand, for the central position the values are below 125 W/m², which shows the inhomogeneity of the backside irradiance in spite of being a large system with adjacent arrays. For both, east and west, a overstimation of the irradiance is found by both methods. Nonetheless, the values of RMSE are around the 5%.

The following figure shows that the two modelling approaches are close and accurate regarding front side irradiance:

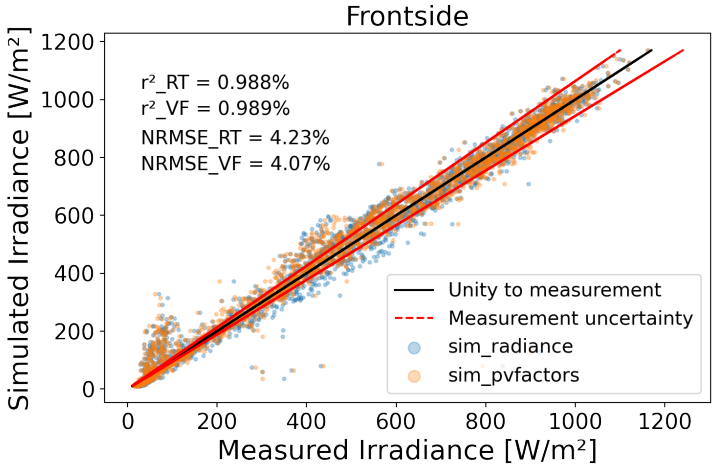

Figure 4.16: Correlation of the hourly measured and modeled irradiance for the front side incident irradiance of the tracking system at Wuhai, China.

If we look at integrated variables, like the monthly irradiations, we can generate the following graph:

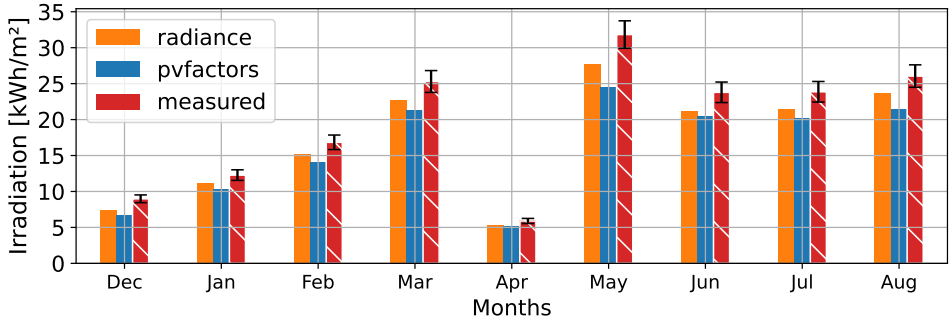

Figure 4.17: Monthly simulated and measured backside incident irradiations in the POA of the tracking system at Wuhai, China.

Summary of the optical model validation

Performance analysis and validation of optical back irradiance models were carried out for the small-sized and large-scale tracking bifacial PV systems. These validations and analyses were performed by comparing the irradiance measured in the POA in the field.

The results of the localized irradiance simulation demonstrate that RT and 2DVF are suitable for modeling small-size bifacial PV arrays, eight modules in 2L(i.e., landscape configuration). Furthermore, the lower deviations were found for the top and middle positions for all the approaches. However, the error increases rapidly while heading to the reference cell closer to the ground. According to the used metrics, all the tools tend to overestimate the measured irradiance.

The analysis of the backside irradiance of the six reference cells at the POA tracking system has shown that the cells located at the west and east border receive more irradiance than the one in the middle. Similarly, the reference cell placed at the north extreme of the tracker showed a 20% difference for summer midday. The inhomogeneity in the module located at this border position can be linked to the power loss of a string and should be further studied in the future.

On the other hand, the front irradiance is simulated with good agreement by both models (2DVF and RT). Nonetheless, higher deviations were found for the HSAT system at the PSDA with no surrounding rows. But, a better agreement was found for the localized irradiance validation at the large-scale PV tracking system. However, there was a tendency to overestimate the back irradiance.

CHAPTER 5

Bifacial PV system energy modeling

In this chapter the previous described models including the analyzed optical models are combined together for validation of the energy yield and bifacial gain. We validate the calculation of the energy yield. These validations are carried out based on the PV systems located at the PSDA (Chile) and the large scale PV plant located in China. Thus, different bifacial technologies under real conditions of operation are evaluated. Thereby, the performance of the sub models and mainly the impact on the estimation of the rear irradiance from each method analyzed in the previous chapter is evaluated, allowing us for determining the range of usefulness of each optical approach as view factor(VF) and ray tracing (RT). The energy yield of three small size bifacial PV systems made up of different PV technologies on a fixed tilt configuration are modeled and compared to measured data. The performance of the monitored bifacial PV systems is also discussed.

5.1 Energy yield experiment

The modeled output from the previous experiment is input to the calculation of the energy yield of fixed and tracking systems configurations and locations to be compared to the measured data.

The figure 5.1 describes the connection of modules at the fixed tilt test bench installed at the PSDA. The measurements are performed at module level by connecting two modules placed at a inner location (yellowed module) of each PV string to an IV tracer. For the string level assessment, 4 of the 8 modules are connected in series to form a string of each technology (one technology per row).

For the calculation of the electrical DC production, the irradiance calculated at each module mesh element by the 2D and 3D VF was averaged as well as the irradiance calculated along the center of the module by the RT approach. The figure 5.2 shows the simulation of irradiance at each module during the year 2020. As can be seen the deviation between each modeled result is higher at the edge of the test bench. The trend from the 2D VF approach is expected to be constant since no border effect can be reproduced. This way the modules

at the center of the test bench can be better addressed by this method.

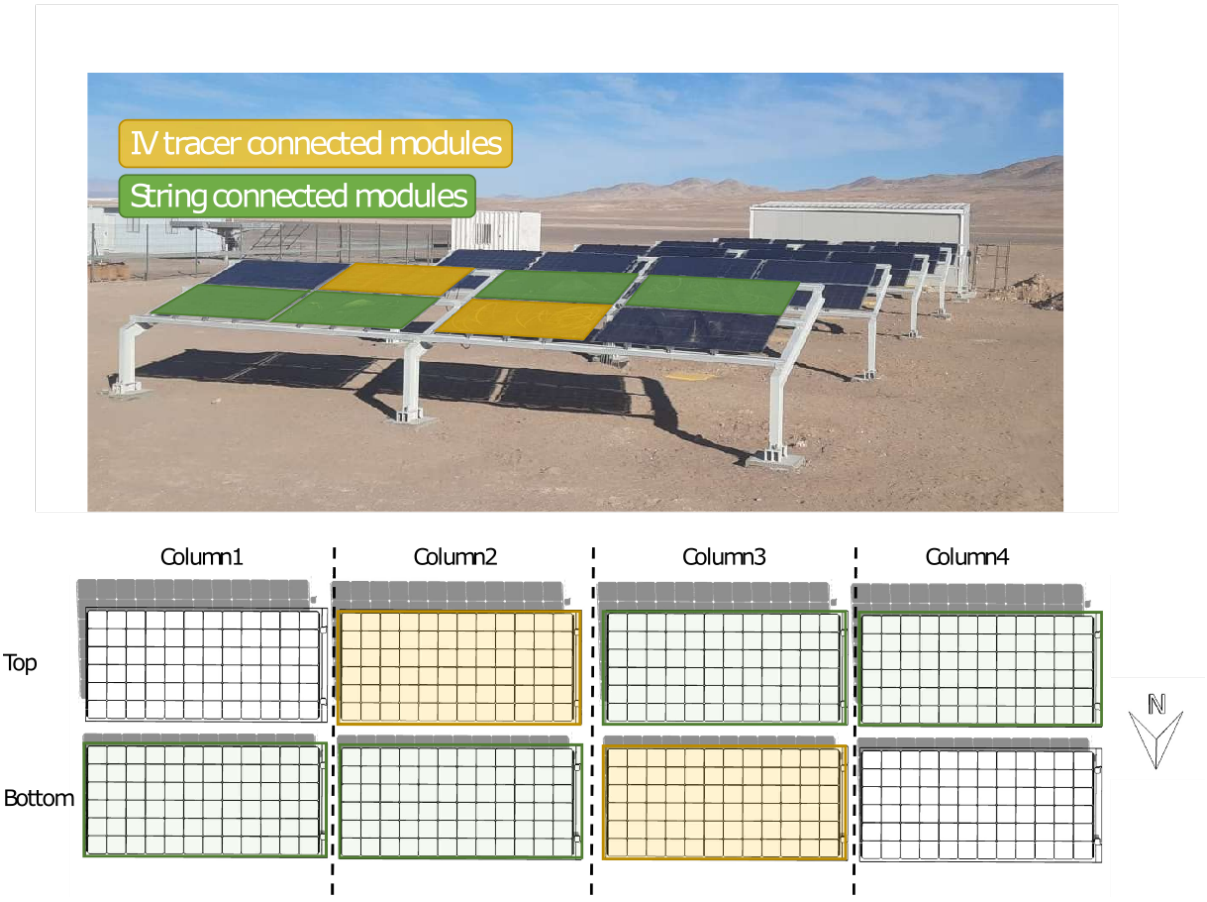

Figure 5.1: Image of the bifacial fixed tilt PV installation and layout of the test array. Modules connected to the IV curve tracer are highlighted in yellow. The PV string is made up of four modules, highlighted in green. Others are dummy modules.

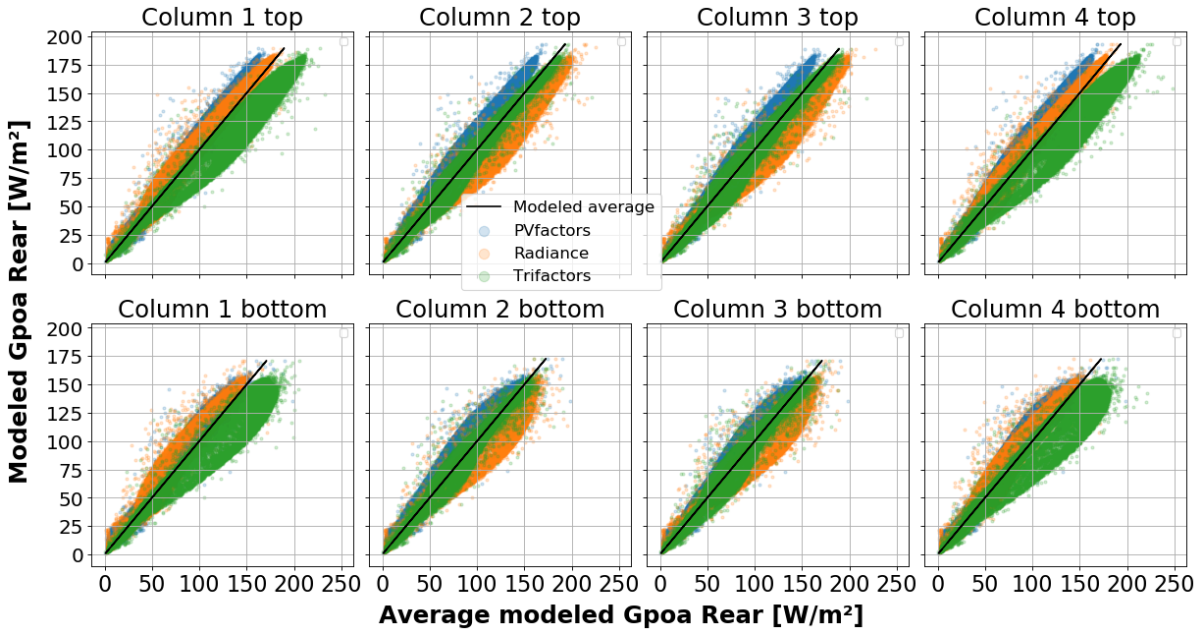

Figure 5.2: Simulated rear POA irradiance as a function of the average of the three simulations tools for the fixed tilt test bench. Solid black line is the unity to average.

The bifacial fixed tilt PV system located at the PSDA was described in the previous section. The outputs from this set up are used to validate the energy yield and the module temperature simulation results by using as input the modeled irradiance from the RT and VF irradiance models.

As mentioned in the previous section, the rear irradiance measured at the center of the fixed tilt test bench vary strongly between winter and summer, along the width of the the PV system i.e., the hierarchy between the most and the less irradiated positions is flipped. This affects the rear irradiance distribution and certainly the amount of produced energy by a module, respect to the position above the ground within the mounting rack. This is consistent given that the clearance height plays an important role on bifacial gain. In Figure 5.3 one can observe the relative difference in energy between the bottom and top modules per technology. A positive difference is observed for the fall-winter-spring period (i.e. March to October) and negative percentage of difference for the summer period. This suggests a higher rear reflected incident irradiance during winter time onto the bottom module and lower during summer time, i.e., higher rear irradiance on the top module. This behaviour is a consequence of the variation of the solar tilt angle between summer and winter, and therefore on the displacement of the cast shadow by the PV system. A maximum of 4% of energy difference is found for a HET technology (BF=0.90) during winter and a difference of the half during summer (-2%). A similar tendency is found for the nPERT and PERC+ technologies with the scaling factor due to the bifaciality. Accordingly, the following evaluations of results are considering the position of the modules, top and bottom along the test bench.

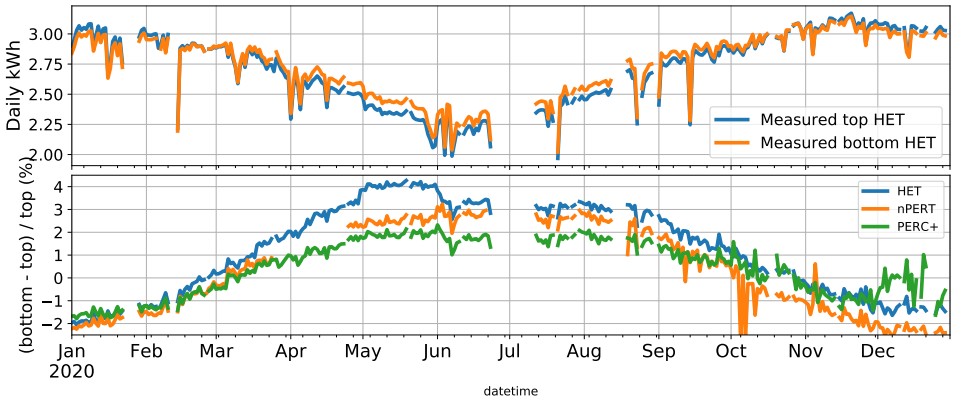

Figure 5.3: Seasonal variation of the measured energy by technology at the fixed tilt test bench along the year 2020.

The bar plot in Figure 5.4 shows a comparison between measured and modeled monthly specific energy yield of the bifacial modules located in the center top and bottom positions mounted on the 2X4 test bench as shown in the layout in Figure 5.1. It is important to mention that these first results are obtained using the in field measured temperature of each module in order to evaluate purely the influence of the optical and electrical model on the accuracy of the output energy simulation. The difference in the results using the modeled temperature as described in section 5.2, are mentioned. It is observed that despite the slight overestimation mainly during the winter months, the trend is well modeled by the simulation. The seasonal variation, i.e. higher energy yield during summer than winter, is well addressed. The higher deviations were found for the months between May and August i.e. at the beginning and ending of winter. During these months the angle of incidence of irradiance (the angle between the solar vector and the surface normal) during midday tends towards the maximum, since the sun's elevation is the lowest for the south hemisphere. In this regard, the deviations remain below the uncertainty of the measurements, during all the period for RT and 2DVF, for both the upper and lower module. For the latter, a clear difference is observed between the summer and winter months. The results obtained by the 3D VF are particularly high during May, June and July. This overestimation is thought to be due to the fact that this version of TriFactors does not include the effect of the supporting structure on the shadow cast by the system, thus there is a higher non shadowed component ($GHI \times VF_{nonShaded}$) in the rear incident irradiance. The dc power results calculated from the 2DVF simulated irradiance showed the lowest deviation, approximately a mean value of 1.53% and 1.5% for the top and bottom position, respectively. Lowest differences between modeled and simulated energy yields for the bottom position. The mean deviations for the bottom module can be reduced by 1.8%, 21.4% and 13.9% respect to the mean deviations found for the top module, for the pvfactors, radiance and Trifactors respectively.This is driven by the higher accuracy during summer months for the bottom module. When the sun is the higher in the sky during summer the PV array cast a shorter shadow on the ground.

The correlation between measured and modeled power output of the bifacial HET PV module in the fixed tilt test bench for the 2020 with hourly timestamps is depicted in Figure 5.5. A high correlation ($r^2 > 95\%$) and a low spread is found for both top and bottom modules, however a slight difference is found on the NRMSE between these two positions. A lower NRMSE is found for dc values simulated for the bottom position by using RT irradiance,

and on the contrary a lower NRMSE is calculated for the top position when using the 2DVF irradiance. This suggests a better performance by RT to take into account near shadowing.

In general, the modeled long term specific energy yield of bifacial PV modules results show a good agreement with the measured values in both positions, with an accumulated overall deviation around + 1.5%, +3.0%, + 4.8% by using a 2DVF, RT and 3DVF. A better performance of a 2DVF approach over a 3DVF might be due to the reduction of the incident back irradiance on the modules due to the assumption of the infinite long PV array by the 2DVF and because the analysis is made with modules that are in the middle of the test bench.

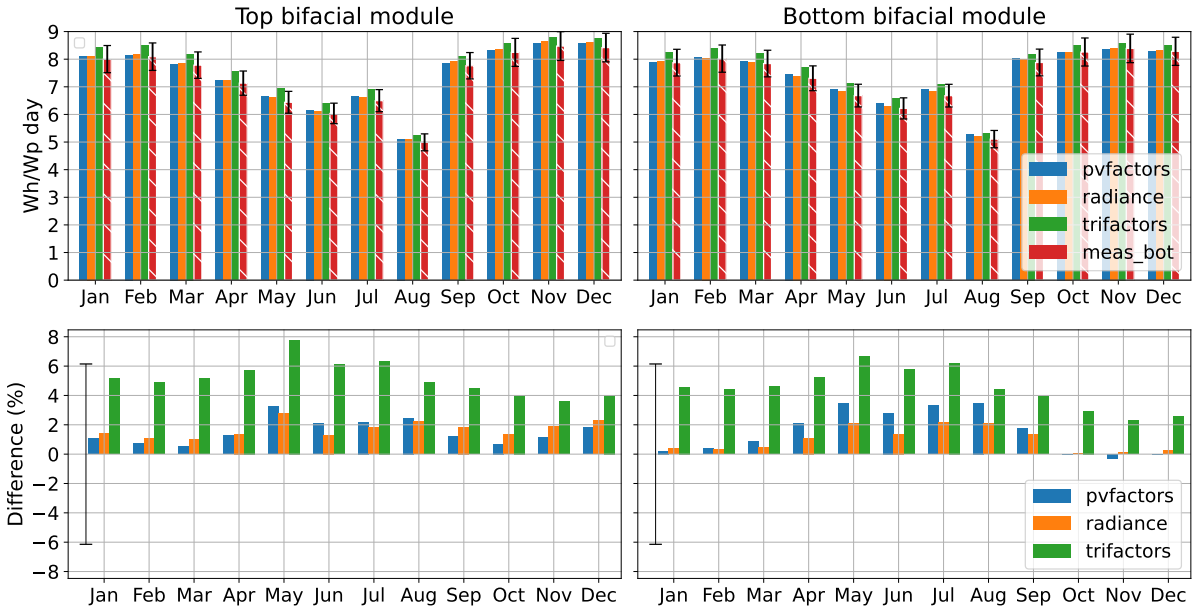

Figure 5.4: Validation of monthly average of daily specific yield for bifacial HET PV technology located in the upper center and bottom center locations of the fixed test bench of 8 modules at the PSDA.

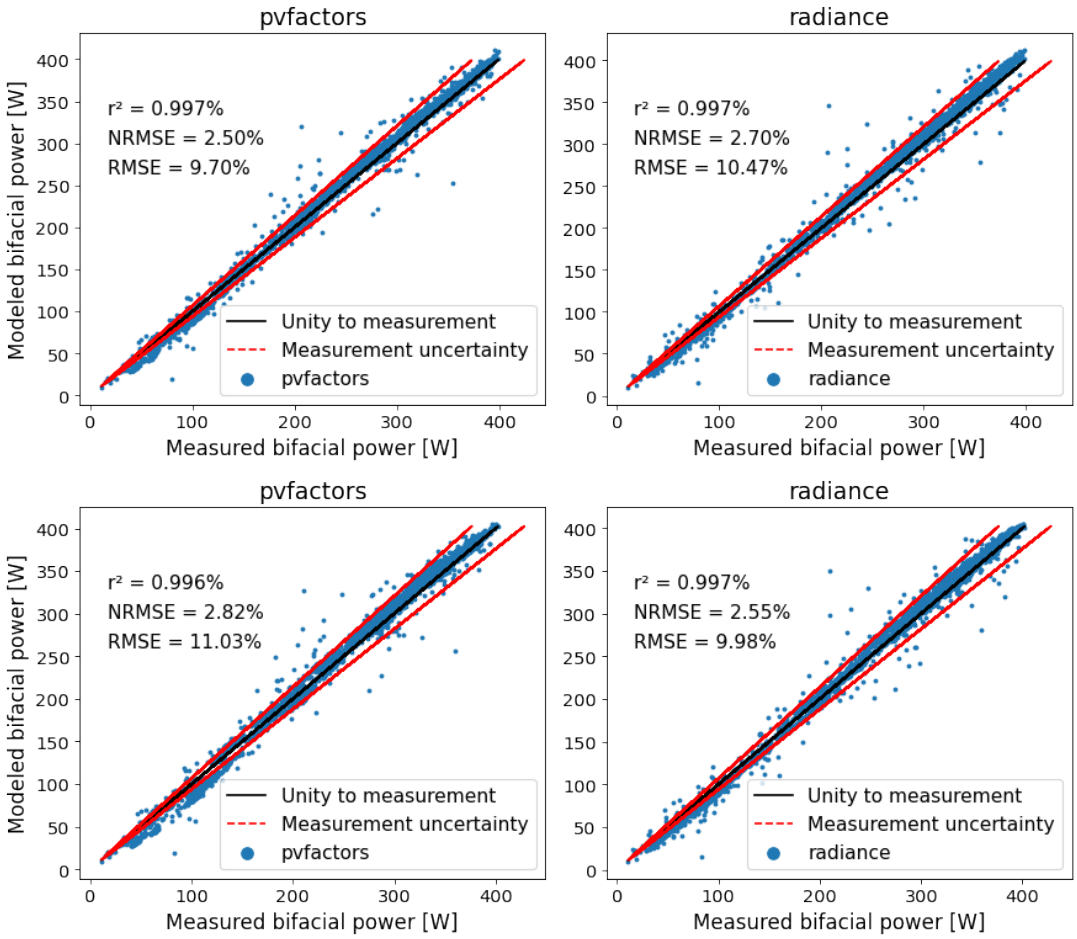

Figure 5.5: Correlation of the hourly measured and modeled output of the bifacial HET module located in the upper (top) center and the bottom (bottom) center locations of the test bench of 8 modules.

The annual average of of daily energy yield for all the module technologies on the fixed tilt test bench was obtained from the daily energy yield calculation. The Figure 5.6 shows the comparison of the simulation results for each technology and position over the fixed tilt test bench along the year 2020. Consistently with the monthly results observed previously, the deviations in the estimation of the annual mean energy yield remain below 3% for RT and 2DVF and above 3% for the 3DVF for all the simulated bifacial technologies. This means it is possible to have an estimation for the energy yield of a bifacial module within a string with a deviation of less than 3%. It should be emphasized that these results are calculated for the modules placed in the center of the PV array. This position is less exposed to back radiation than the modules placed at the edges.

As for this study case there are no measurements of modules located at the edges of the string, it is not possible to make a direct comparison with the simulation at this location. However, the result of the simulation of the modules forming the string is analyzed in the 5.7.

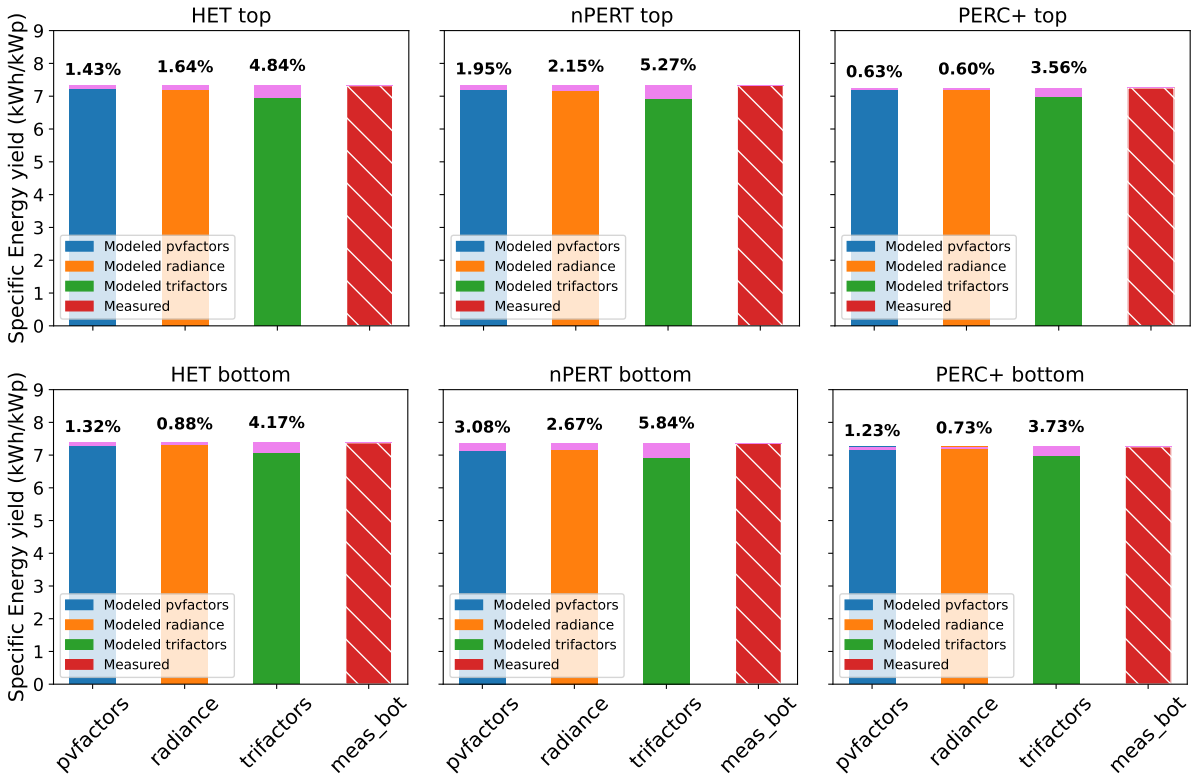

Figure 5.6: Simulated and measured (red bar) mean annual energy yield and the differences (magenta at the top of bars) respect to measurement, for the modules at the fixed tilt test bench at top and bottom center positions.

The Figure 5.7 shows the simulation of the monthly mean energy yield of the string made up by 4 modules mounted in the fixed tilt test bench at the PSDA (green highlighted modules in Figure 5.1). The energy yield is simulated by input the irradiance incident on each module of the HET string. The results show very good agreement with the measured values with a similar accuracy as for the simulation of a single centered module shown previously in Figure 5.4. In general both RT and 2DVF methods tend to slightly overestimate although below 4%, i.e. within the uncertainty range. Nonetheless, it is possible to observe a higher overestimation by RT, this may be due to the overestimation of the backside irradiance at the edge of the string that is possible through RT and not by 2DVF.

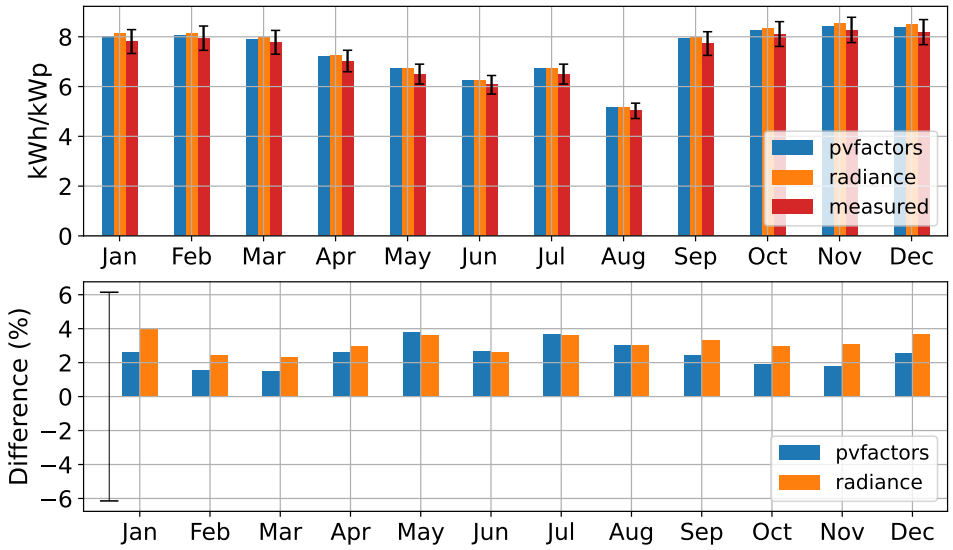

Figure 5.7: Simulation of the monthly mean energy yield of the by input the irradiance results by RT and VF over each module of the HET string mounted at the fixed tilt test bench at the PSDA.

The validation in terms of bifacial gain (BG) is very important as it is a crucial parameter for benchmarking bifacial PV technology against other conventional PV systems. The Figure 5.8 shows the annual BG for the year 2020 measured and simulated by RT as well as for 2DF and 3DV. This results are obtained under the conditions of operation of the Atacama desert for the fixed tilt bifacial test bench with a mean albedo of 0.32 (desert sand), using bifacial modules with a bifacial factor from 60% to 88% and a ground coverage ratio of 30% and a clearance height of 0.7 m. These results have been well modeled by the 2DVF approach.

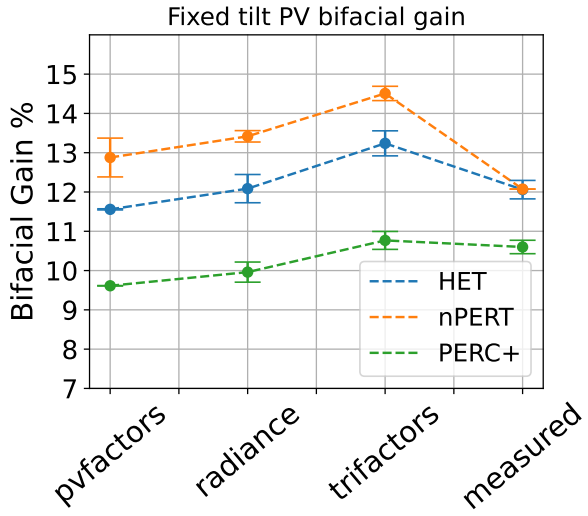

Figure 5.8: Simulated bifacial gain for fixed tilt modules installed at the PSDA, Chile.

5.2 Temperature analysis

A further comparison made based on the PV systems at the PSDA was the modeled temperature using the Fainman model described in section 3.2. The temperature of the modules at the PSDA is measured every minute by two PT100 sensors attached to the surface of each monitored module. The monthly mean of daily mean measured and modeled temperature is plotted in a bar chart for each month and bifacial technology shown in Figure 5.9. As this Figures shows, there is a good agreement in terms of trend between the modeled and measured temperature, i.e, both modeled and measured shows an almost constant value of the monthly mean temperature from January to May, from where it decreases to the coldest temperature in June. Particularly, the mean monthly modeled temperature tends to be overestimated in comparison to the measured temperature of the HET technology and on the contrary, underestimates for the nPERT and PERC+ modules. These differences can be seen from the deviations in the bar chart plot and similar deviations can be also seen in the correlation plots between measured and modeled temperature. The fainman coefficents (U_0, U_1) obtained by fitting the experimental data to the equation 3.19 presented in section 3.2 are quite similar as can be seen in table 5.1. A mean RMSE about 3.62 °C (4.98% NRMSE) from the simulation and measurement comparison for all the modules is found by using this method.

Table 5.1: Experimental coeffients (U_0, U_1) obtained by fitting the fainman equation to the experimental data at the PSDA for the estimation of the module temperature.

	HET	nPERT	PERC+	Unit
uo	23.631	23.572	22.571	W/m^2K
u1	2.131	2.284	2.259	$W.s/m^3K$

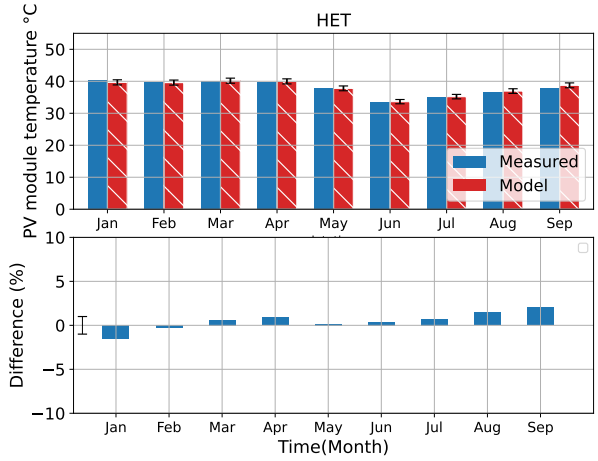

(a) Monthly mean measured and modeled HET module temperatures.

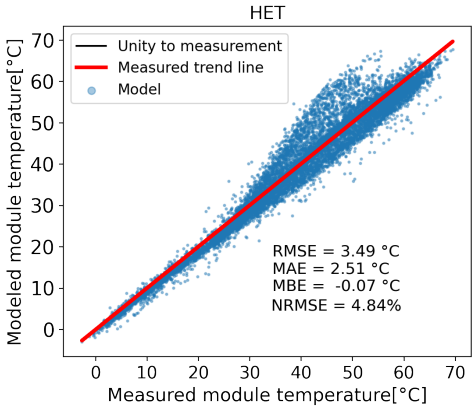

(b) Correlation between measured and modeled module temperatures for the HET PV module at the PSDA

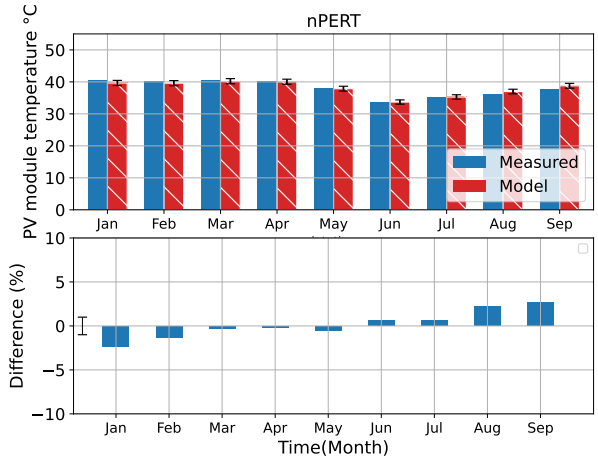

(c) Monthly mean measured and modeled nPERT module temperatures.

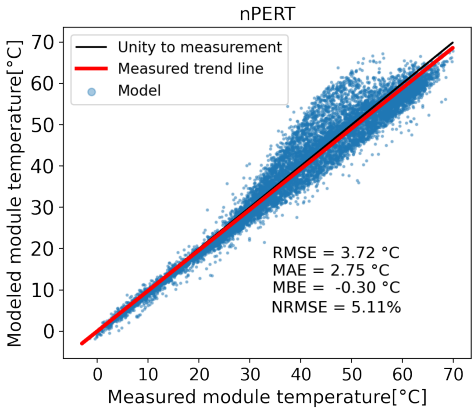

(d) Correlation between measured and modeled module temperatures for the nPERT PV module at the PSDA

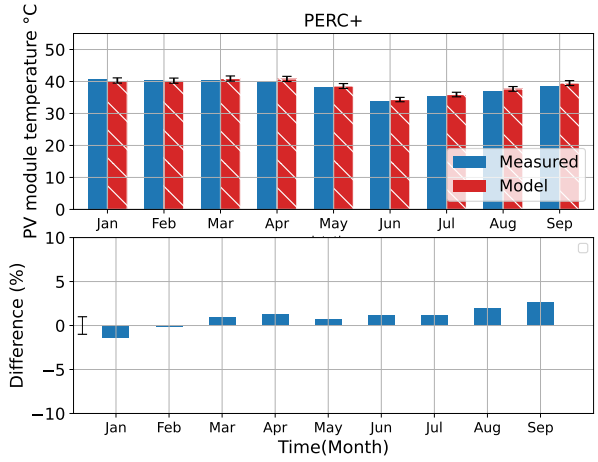

(e) Monthly mean measured and modeled PERC+ module temperatures.

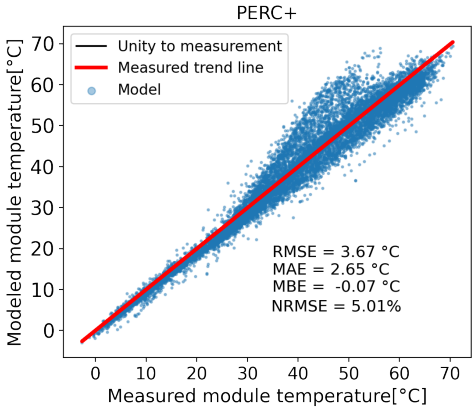

(f) Correlation between measured and modeled module temperatures for the PERC+ PV module at the PSDA

Figure 5.9: The bar charts in (a),(c) and (e) show the comparison of measured and modeled monthly average module temperature values over time. The scatter plots in (b),(d) and (f) compares the measured and modeled hourly module temperature values.

In the previous section, the results of the simulation were presented in order to evaluate the accuracy in the estimation of the energy produced by coupling the optical and electrical models. The Figure 5.10 shows a comparison of the energy simulation for the HET module installed at the fixed tilt test bench by considering the results of the thermal model in the calculation. As can be seen, the results show a very good agreement with respect to the measurement, similarly to the results obtained previously for the same module by input of the measured module temperature. In general these results point out that there is an average overestimation of about 1.4% from the model chain when inputing the estimated module temperature with respect to the results using the measured temperature.

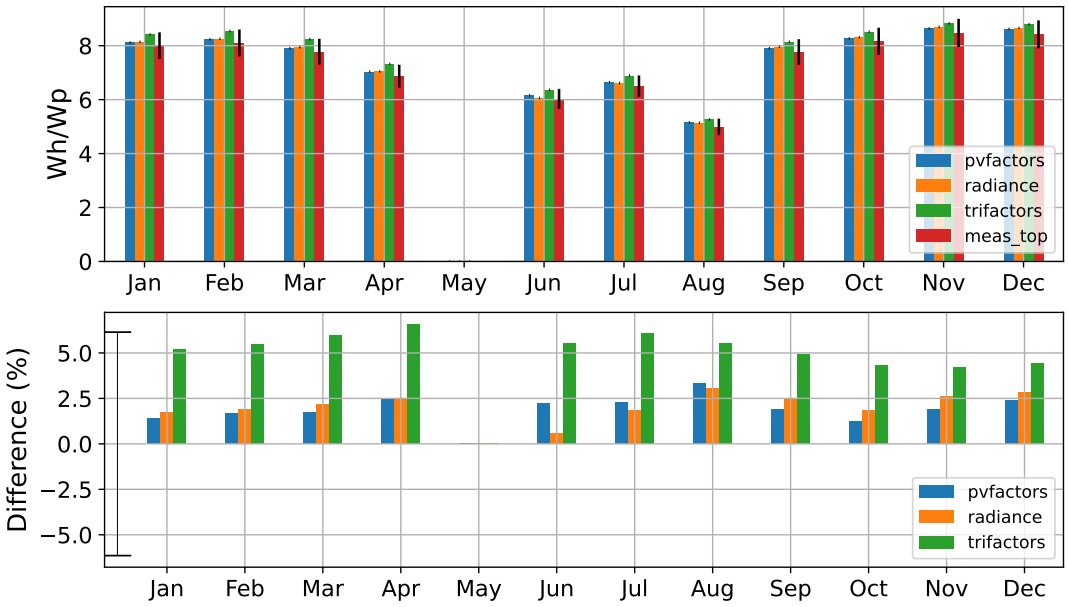

Figure 5.10: Validation of the monthly average specific energy yield obtained by adding the model for the estimation of the module temperature for the bifacial HET module at the top position on the fixed test bench at the PSDA.

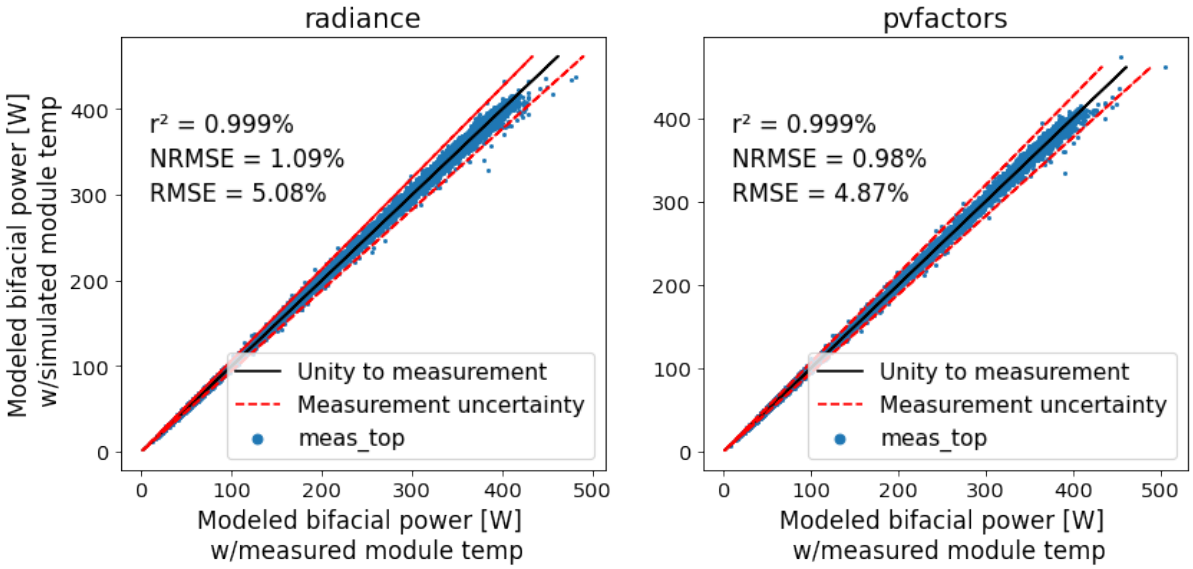

Figure 5.11: Correlation plots of the hourly simulated bifacial power calculated with the simulation results of the module temperature against the results of simulation by using the measured temperature of the HET module at the top position on the fixed test bench at the PSDA. Simulation results during the year 2020.

Figure 5.12: (a) show the measured and modeled monthly energy yield of bifacial HET module installed at the top position at the PSDA. (b) plots the correlation of simulated DC power with estimated and measured temperature of the module.

The modules installed at the PSDA consist of laminated modules in a glass-glass configuration. It has been reported that bifacial modules with this configuration tend to have a higher operating temperature than a standard monofacial glass/backsheet module. The monofacial (PERC) modules installed at the PSDA have the same structure as the bifacial modules, which allows a comparison to be made under similar module dissipation capacity, attributing the differences mainly to the behavior of the cell according to its physical structure. The measured module temperature data available for ten months of these modules were used to find out the difference between the bifacial and monofacial module temperature, and also between bifacial modules. The linear correlation between measured bifacial and monofacial module temperatures installed at the fixed tilt test bench at the PSDA are shown in Figure 5.13

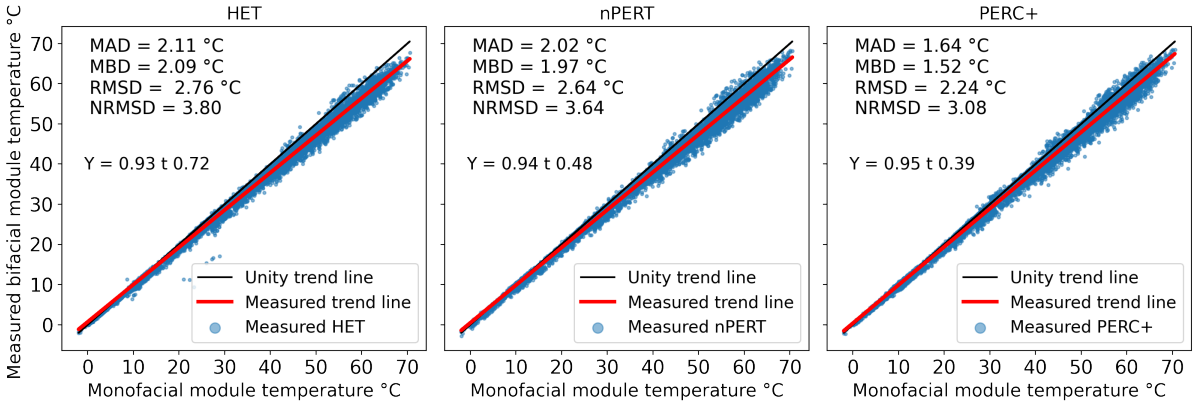

Figure 5.13: Measured bifacial module temperature compared to the monofacial PERC module measured temperature at the PSDA fixed tilt test bench.

As can be seen in the Figure 5.13, both the bifacial and monofacial modules show a very similar behavior in the temperature of operation, although slightly lower for the bifacial modules. From the slope analysis of each plot it is possible to identify which module operates at a higher temperature. In particular, the HET module tends to heat up ∼7% less than the monofacial module similarly as the nPERT module (∼6%), and the PERC+ (∼(5%) technology based module.

As described in section 2.4 each bifacial technology counts on a different PV cell structure and thus cell surface metallization. A previous study has shown that due to the open rear side, bifacial solar cells absorb less infrared light and therefore operate at lower operating temperatures compared to monofacial aluminum back surface field (Al-BSF) solar cells [51]. The Figure 5.14 shows a comparison between bifacial module temperature technologies. It can be observed that there is a high correlation between the temperature of the nPERT and HET modules and a slight difference between the latter and the PERC+ module. This suggests that the behavior of the bifacial technologies in terms of operating temperature is very similar under real operating conditions. These results are obtained in outdoor conditions in the Atacama desert.

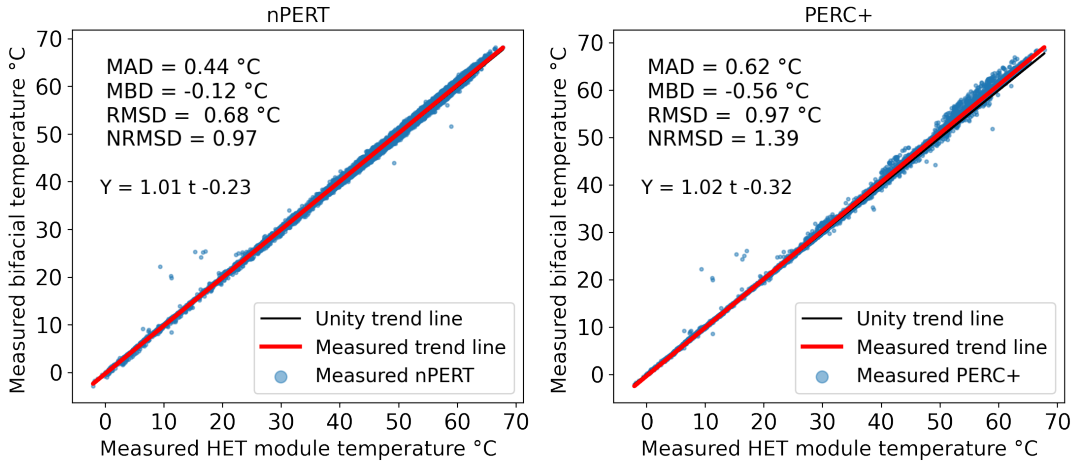

Figure 5.14: Measured bifacial nPERT and PERC+ module temperatures compared to the bifacial HET module measured temperature at the PSDA fixed tilt test bench.

The temperatures of the same based technology modules installed at the tracking system were also analyzed. Given the higher irradiance received by the modules in a tracking system, a higher operating temperature is expected with respect to the modules in a fixed system. Nonetheless, it is alleged that given the height of the modules above the ground, enabled by a tracking system (2m>), there are better convection conditions, compensating the effect on the temperature of a high incident radiation [52],[53]. As can be seen from the Figure 5.15, similar trends to those found for the fixed tilt installation are found for modules mounted in the tracking system, with a slightly lower temperature trend for the HET module. Thus, when comparing the HET and nPERT based technologies, the results show a slightly elevated temperature of the latter as shown in the Figure 5.16. These results may be related to the slight difference in the temperature coefficients of each technology presented in the table 3.1 in the section 3.2

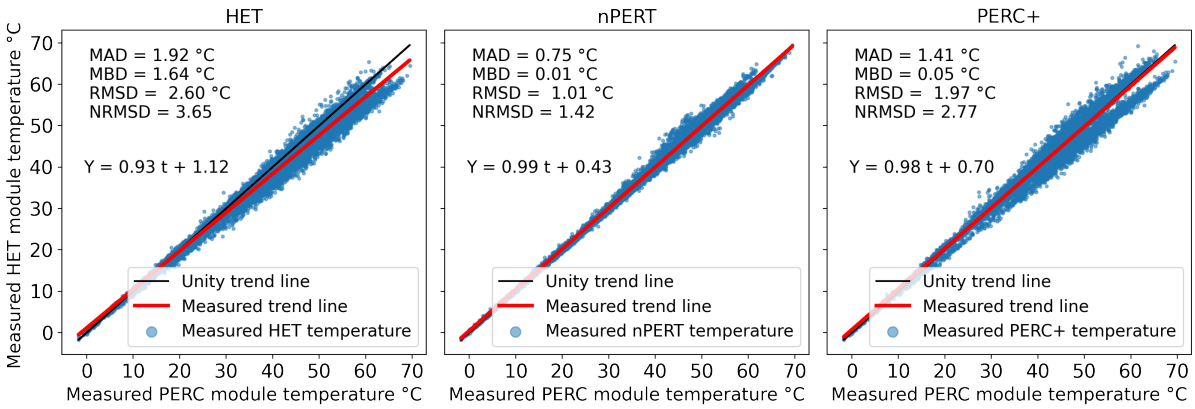

Figure 5.15: Measured bifacial module temperature compared to the monofacial PERC module measured temperature at the PSDA tracking system.

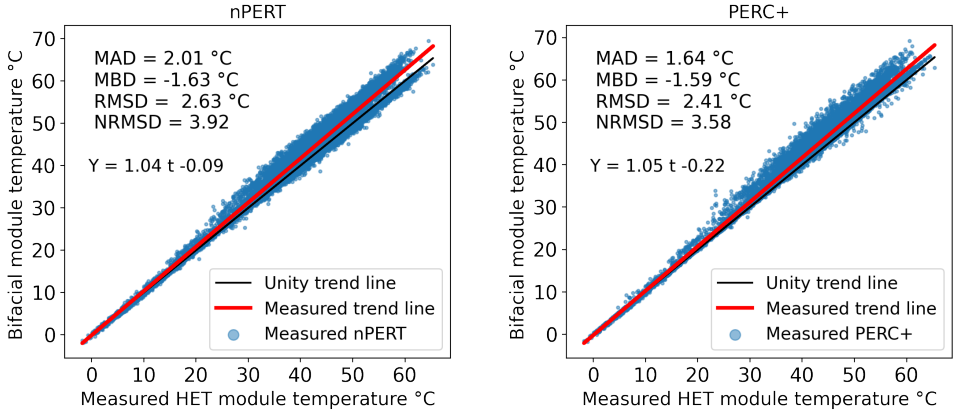

Figure 5.16: Measured bifacial nPERT and PERC+ module temperature compared to the bifacial HET module measured temperature at the PSDA tracking system.

These results demonstrate that the operating temperature of the bifacial modules under Atacama Desert operating conditions are similar to or lower than those achieved by the monofacial modules. These results are in accordance with the findings in recent studies

[54],[55], where it is stated that the operating temperature of the bifacial module can be similar or lower than the monofacial module and that it may depend on the location of operation and to the fraction of rear irradiance absorbed by the module in comparison to the front irradiance. Also, it depends on the mounting configuration and the bill of material (glass/glass or glass/backsheet) of the PV module.

5.3 Large scale PV system

The validation from the tracking PV power plant (installed by Canadian Solar Inc.) data will be discussed in the following paragraphs. These systems are increasingly becoming the most convenient alternative for the use of bifacial technology due to their potential for high energy efficiency compared to other types of installations. The validation of the energy yield calculated from VF and RT irradiance results for this large scale bifacial system is shown in Figure 5.17, the description of the bifacial PV system is reported in section 4.3. The validation is based on the data from 3 strings connected to a central inverter. The PV arrays are depicted in Figure A.3.3. A good approximation is found between the measured and modeled energy yields of monofacial PV system. The trend has been well modeled by both models RT and 2DVF across the months, nonetheless, the 2DVF approach tends to overestimate the energy yield more than RT for the monofacial system. Both approaches have predicted the peak of specific energy yield of monofacial and bifacial systems in May. It has to be mentioned that there was a tracking system malfunctioning during several weeks from the month of February to March resulting in a reduction in power generation during these months. A lower accuracy was obtained for the case of the bifacial system. There is an overestimation slightly above the upper limit of the uncertainty of the measurement. It is also observed that both 2DVF and RT showed very similar monthly absolute deviations.

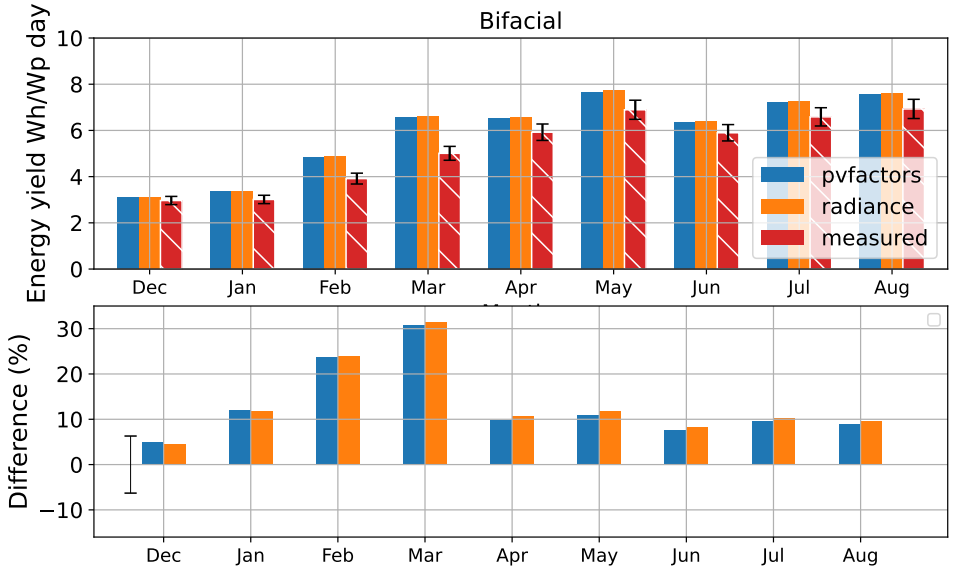

(a) Monthly validation of specific energy yields of the bifacial tracking system at Wuhai,China.

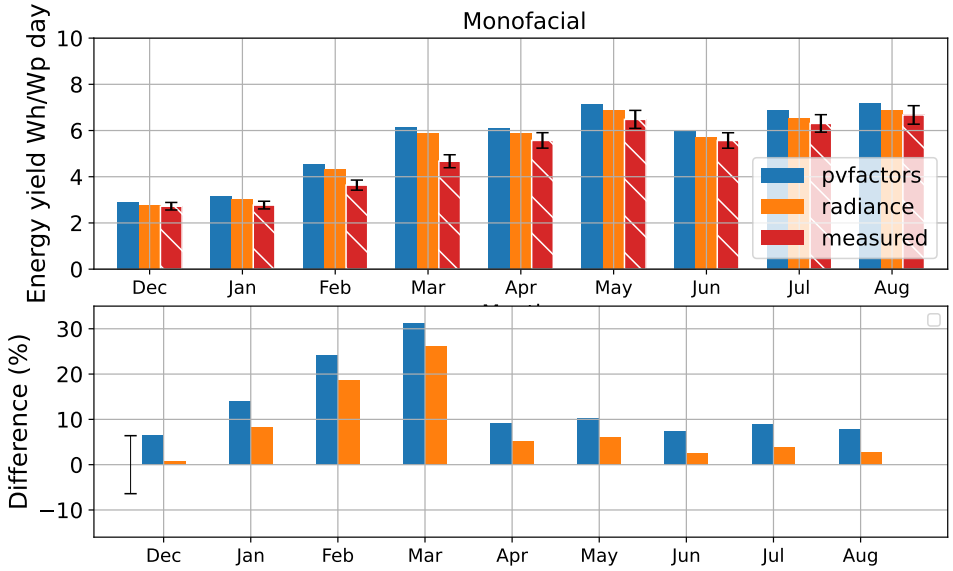

(b) Monthly validation of specific energy yield of the monofacial tracking system at Wuhai,China.

Figure 5.17: (a) and (b) show the measured and modeled monthly energy yield of bifacial and monofacial PV systems in Wuhai, China respectively, plus the modeling deviation along 9 months in 2019.

5.4 Uncertainty Analysis

The irradiance sensors installed in the POA of test benches at the PSDA are Ingenieurbüro GmbH reference cells [56]. The measurement uncertainty stated by the manufacturer datasheet is ± 5 W/m² $\pm 2.5\%$ of reading. In figure 5.18 this uncertainty is represented for several irradiance values.

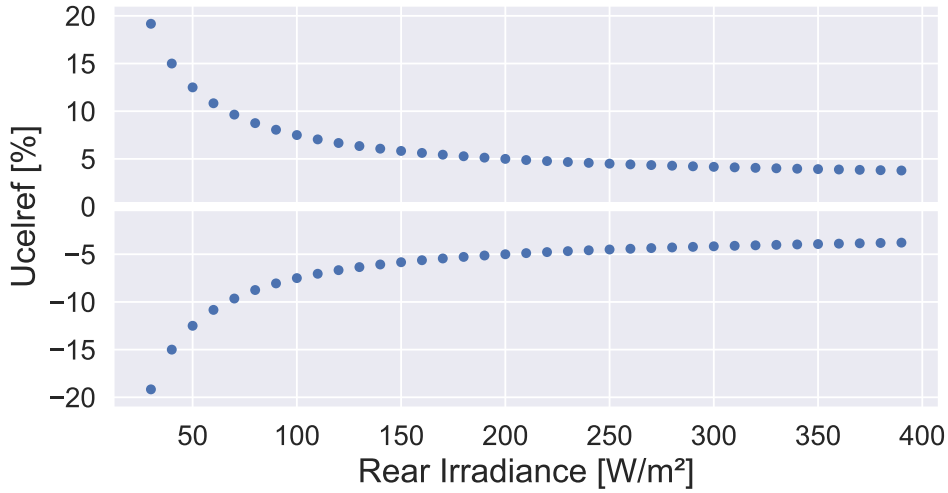

Figure 5.18: Uncertainty calculated for different values of irradiance according to reference cells manufacturer datasheet.

It means that under a rear irradiance of 200 W/m², the uncertainty is 5% and for the lowest irradiance of 15 W/m² $U_{refcell} = 35.8\%$. This reference cells offer a technically and economically convenient solution considering its operation under the Atacama desert conditions; moreover, they can be commonly found in PV plants for irradiance monitoring.

The standard uncertainty is defined by U_x as,

$$U_x = \frac{a}{\sqrt{3}} \tag{5.1}$$

Similarly to the uncertainty study in [37], the expanded uncertainty of rear irradiance measurement may be dependent on the following parameters,

- Uncertainty of the reference cell (according to the specification sheet) ($U_{refcell}$)
- Uncertainty in the measurement of collection unit ($U_{datalogger}$)
- Uncertainty of the tracker angle ($U_{trackingAngle}$)
- Uncertainty in the albedo measurement (U_{albedo})
- Uncertainty in the installed location of the sensor (U_{height})

Nonetheless, we consider only the $U_{refcell}$, U_{albedo} and the U_{height} in this study, the other uncertainties are considered as negligible. Thus, assuming a coverage factor of 2, the combined total uncertainty is calculated as the square root of the sum of the squares of the standard uncertainties as in equation 5.2.

$$U_x = \sqrt{(\frac{U_{refcell}}{\sqrt{3}})^2 + (\frac{U_{albedo}}{\sqrt{3}})^2 + (\frac{U_{height}}{\sqrt{3}})^2} \tag{5.2}$$

There is indeed an uncertainty associated to the estimated position of the reference cell in the backside of the array, U_{height}. Its value can be calculated considering the gradient

of measured rear irradiance. For this, the distance and the highest difference of measured irradiance between the reference cells (top to middle or bottom to middle) are considered along the entire period of measurement as the worst scenario case. Once these values are obtained, the distribution of gradient of the irradiance on the backside is calculated along the distance between the cells. Thus, at the clearance height of the fixed tilt installation, the maximum difference of 119 W/m² was found between the top and middle reference cells. This translates to approximately a 1% change in irradiance for each cm of distance between the two positions.

The albedo from the test PV fields used in this work is measured by an albedometer from Kipp & Zonen along the period of study. Therefore, the standard uncertainty is given by the manufacturer datasheet, and is assumed to be the same as for a pyranometer around.

5.4.1 Uncertainty due to input data

Regardless of the accuracy of mathematical modeling, the results of the simulations will be influenced by the uncertainty of the input data such as the GHI, DHI or DNI and the measured albedo. Since in this work the optical model results are based on the measured irradiance, an evaluation of these sources of uncertainty is made. This way, the uncertainties due to the input data of the simulation tool are added to the mathematical formulation and presented in the validation section. Similarly to the methodology presented in [55], the uncertainty on the ground reflected incident irradiance in the backside POA can be propagated from the uncertainty of the measured GHI, DHI and albedo. From the equation 3.13, it can be rewritten as function of three variables since the VF are considered to not influence the calculation of uncertainty.

$$E_{back,POA} = \rho \times (GHI + DHI) \tag{5.3}$$

From the relative uncertainty of the sensors, we can formulate the relative uncertainty as $\delta E_{back,POA}/E_{back,POA}$. Assuming a normal distribution of the backside POA irradiance, the differential of $E_{back,POA}$ can be expressed as follows:

$$\delta E_{back,POA} = \delta[\rho \times (GHI + DHI)] \tag{5.4}$$

$$\delta E_{back,POA} = \delta\rho \times (GHI + DHI) + \rho \times \delta GHI + \rho \times \delta DHI \tag{5.5}$$

According to the definition [reference book], the uncertainty propagation for a multi-variable function is given by the squared root of the squared relative uncertainties of its variables.Thus, factoring the term $\rho \times (GHI + DHI)$, it is possible to express the relative uncertainty of $E_{back,POA}$ as,

$$\frac{\delta E_{back,POA}}{\rho \times (GHI + DHI)} = \sqrt{\left(\frac{\delta\rho}{\rho}\right)^2 + \left(\frac{\delta GHI}{GHI + DHI}\right)^2 + \left(\frac{\delta DHI}{GHI + DHI}\right)^2} \tag{5.6}$$

As the GHI, and DHI are measured by pyranometers, the same relative uncertainty can be considered, and thus the above equation can be reduced as follows,

$$\frac{\delta E_{back,POA}}{E_{back,POA}} = \sqrt{\left(\frac{\delta\rho}{\rho}\right)^2 + 2 \times \left(\frac{\delta GHI}{GHI + DHI}\right)^2} \tag{5.7}$$

The above equation depends on the level of irradiance of GHI, DNI and of the relative uncertainty of the albedo.

Summary of system energy validation

The modeled power obtained by simulation of the irradiance by using the VF and RT was compared to the measured power of three different bifacial technologies, HET (heterojunction), nPERT, and PERC+. The measurements were made on arrays and modules placed in the center of the fixed tilt array surrounded by neighboring rows and modules operating under natural operation conditions. The results have shown good agreement with the measured data for RT and 2DVF. Nonetheless, an overestimation of over +5% is found when calculating the annual energy yield from the irradiance obtained using the 3DVF approach. These results highlight the importance of incorporating the effect of the support structure on the array backside incident irradiance.

Although the sub-estimation of the localized back incident irradiance modeling validation in the previous chapter, an overestimation was found for the monthly energy yield at the large-scale PV plant in Wuhai, China. This may be due to soiling conditions since it is a desertic zone with regular high wind speeds. Controversially, the results show a lower deviation when estimating using the RT calculated irradiance.

CHAPTER 6

Default Diagnostic on Bifacial PV systems

The I-V characteristic of a PV field provides information on its operating state for given conditions of irradiance and temperature when it is available. A modified shape of the I-V curve may be indeed a signature of a particular defect or a category of defects. To exploit this potential, it is essential to count on the knowledge of the behaviors of the PV field under different defects. The direct method to obtain these characteristics under defective operation, consists in physically creating the considered defects in a real PV field and recording the resulting field behavior. This method is not economically feasible, not very reproducible and requires a lot of effort and materials. An alternative solution is to use a simulation tool. The use of data from highly accurate models has been increasingly employed for algorithm training due to its low cost compared to the installation of expensive test platforms.

The objective of this chapter is to model a failed bifacial PV array, thus obtaining the I-V characteristic at a given operating condition for any fault and for any configuration of the PV system. Based on the assembled modeling chain presented in the previous chapters, we obtain the I-V characteristic of a PV field. based on this, we are going to present the modeling approach proposed in our study. This way, we are going to describe the modeling of a PV field in healthy operation and then in fault.

6.1 Proposed modeling approach

The objective of modeling for diagnostic purposes is not to obtain a generic model representing a PV array in faulty operation, but to obtain the I-V characteristic of a PV array for any determined fault.

The PV cells are the elementary components of the PV array and some defects can occur at the level of these cells, therefore we start our approach to obtain the I-V characteristic of the array from the cell characteristic. According to the architecture of the components constituting a PV array, the calculation of the total IV curve will be obtained by the combination of the elementary components IV curves.

The passage of the I-V characteristic of the components from cell level to module level, or

from module to array, is carried out by making the simple arithmetic sums of the appropriate quantities, current or voltage, according to the configuration (series or parallel connection) of the components. Before moving from one level to another, the I-V characteristic of the previous level must be modified by taking into account the defects that occur. This process is developed through the manipulation of the electrical model described previously in section 3.3 of chapter 3.

6.2 Modeling of a PV field under faulty operation

Establishing a data base of the faulty behavior of a PV array involves establishing a causal relationship between faults and symptoms obtained from the I-V characteristic of the array itself. To do this, a series of simulations must be performed for an exhaustive list of fault scenarios considered. In each simulation, a single fault is considered and the I-V characteristic from this simulation is examined with the goal of identifying potential symptoms that can be traced back to the nature of the fault. This simulation is repeated for all other defects considered in the study case scenario.

We have seen in the previous sections the modeling approach of a PV field in healthy operation, starting from the I-V characteristic of a cell, retrieved from the modules datasheet. First, the idea is to identify among the considered faults (see table XX) those which affect each component of the array. Then we analyze the effect of these identified defects in the determination of the I-V characteristic of the corresponding component. In this section, we first present the identification of the different classes of defects occurring in different components of the PV array. Then, we detail the modeling of these defects.

6.2.1 Defect classification for modeling

As presented in IEA PVPS Task 13 [57], the faults in a PV plant can be classified on one hand according to the location of their occurrence in a PV installation. On the other hand, according to the modeling approach, we can simulate the faults according to the level at which they occur and if they can modify the behavior of the component of this level (group of cells, modules, strings). Taking into account this hierarchy, and as a first application case for the modeling algorithm, we limited the study to the most important faults among them. The classification of the faults used are shown in Table 6.1. The first column shows the succession of components considered in the approach. The second column gives the nature of the different defects involved. And the last column gives the name of each category of defects for the modeling.

Table 6.1: Fault class, nature and component of source

Component	Nature of the defects	Name of defects
Cell	Broken cell Polution, sand, snow. Degradation of interconnections Cracking Corrosion due to reaction of module encapsulant	Mismatch and shading
Module	Penetration of moisture Destruction of diodes Absence of diodes Reverse polarity of diodes Diode short-circuited	Bypass diode fault
String	Break in the electrical circuit Destruction of the connection Corrosion of connections Short circuit of the electrical circuit Module disconnected	Faulty connections

6.3 Modeling of the different defects

we detail hereafter the categories of faults that are retained for the study. First it is necessary to establish a relationship between the defined defects above and the symptoms that occur on the IV curve of the PV system. The next step is to is to analytically generate the identified potential symptoms. Here we show the relationship between the PV system behaviour and the default above described.

6.3.1 Mismatch and shading defect

The mismatch fault is caused by the assembly of cells with a non-identical I-V characteristic. Any change in one of the parameters of the equation $I = f(V)$ will lead to the dissimilarity of their characteristics. The change in these parameters can be due to the intrinsic properties of the cells, since they could have different physical properties due to manufacturing tolerances or because of the degradation of cells in operating conditions. In fact, extreme changes in module temperature, from operating conditions, can lead to the degradation of the module components and in turn allow moisture ingress, or lead to cracking from thermal stress or corrosion from interaction with the polymers inside the module. These failures can be modeled through the variation of one or several parameters such as the series resistance. The shading defect is a special case of the mismatch defect because its presence leads to a reduction of the sunlight received by cells, represented as a variation of I_{ph}.

According to the aforementioned facts, the mismatch and shading defect can be modeled by the variation of the different parameters of the cell. Due to this disparity of cell parameters, the equation $I = f(V)$ must be solved at a cell level and reproduce the IV curve for the group of cells. In a series of components, the voltage produced by each component is no longer

equal for the same current. And when the components are put in parallel, the current supplied by each component is no longer identical for the same voltage.

In the case of mismatch, for a given current, the voltage produced by the cells is not necessarily identical because their parameters are not the same. To illustrate this, let's consider a cell, which is 50% shaded, within a cells substring of 20 cells as in the case of a 60 cell module. In the case of a group of cells, the sum of the voltage of all the cells in the group may be negative. This is because one or more cells in the group produce a high negative voltage (V1‘) when a current greater than their short-circuit current reversely flows through them. It is in this situation that the bypass diode plays its role by turning on when the sum of the cell voltages becomes negative and thus prevents the passage of current through the shaded cell as shown in figure 6.1. Here we can observe the resulting IV curve of the substring (blue solid line) when having a shadowed cell (green solid line) at 50% of the irradiance received by the others. The resulting curve would rather be represented by the dotted blue line if no bypass diode would be accounted for the cells substring.

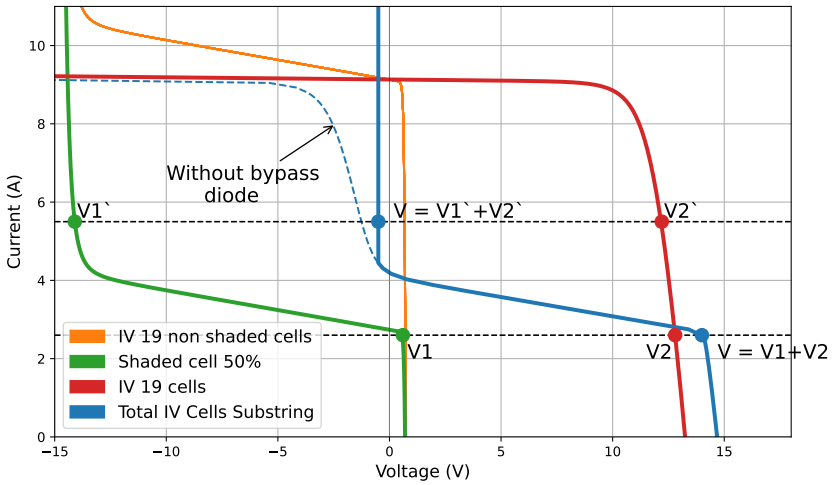

Figure 6.1: Characteristic IV curves of 19 PV cells non shaded within a string. IV curve of the assembled cells (string cells) without perturbation (red solid line). Substring with shaded cell (blue solid line) and activation of bypass diode and without by pass diode (blue dashed line). Single shaded cell (green solid line).

The following figure shows the appearance of a substring of cells without shading and two strings with a shaded cell.

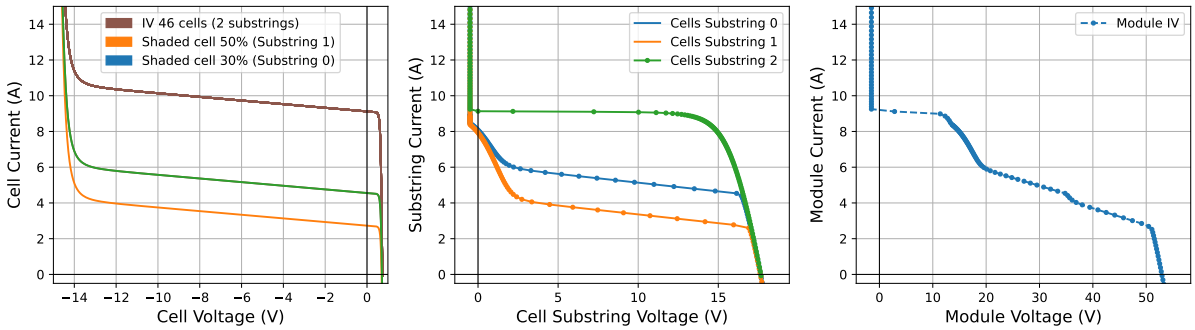

Figure 6.2: Characteristic IV curve of a cell in a cells substring in a module

The penetration of moisture, potential induced degradation (PID), cracking of cells and oxidation processes at cell level due to the degradation of the materials under real conditions of operation could lead to leakage currents. This, will be identified by the decrease of the parallel resistance of a PV cell as shown in Figure 6.3. For a given voltage, the current loss is greater as the parallel resistance is smaller. If the parallel resistance is small enough, it can absorb almost all the current produced by the cell.

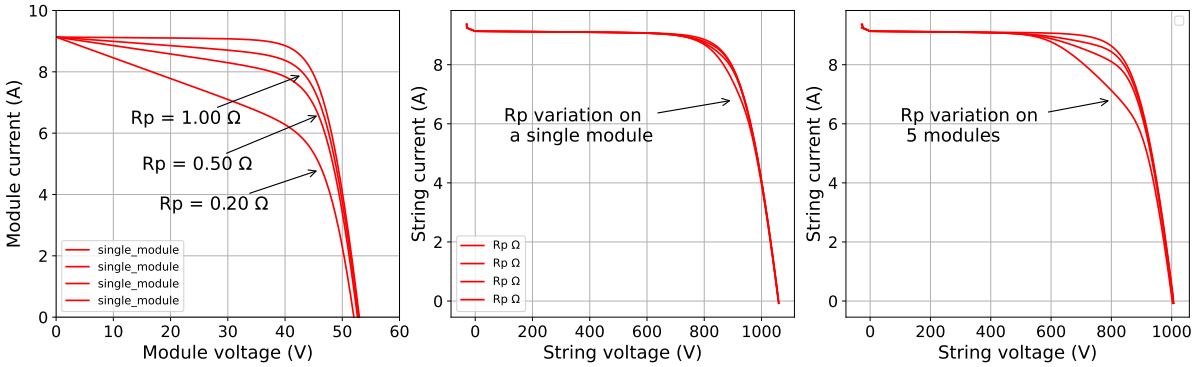

Figure 6.3: Variation of shunt resistance in PV cells in a single module, its impact on a PV string and when considering 5 modules in series connection.

It can be observed also that a reduction in short-circuit current that appears at the module level turns into an inflection point in the string. The reduction of the open circuit voltage remains unchanged during this transition.

6.3.2 Bypass diode fault

In its good state, the bypass diode is on when the sum of the voltage of the cells it protects is negative and it is blocked in the opposite case. In its faulty state, this protective role is no longer assured. According to Table 6.1, the electrical defects associated with such a diode are: short-circuited diode, disconnected diode and inverted diode. In addition to these electrical faults, this diode could possibly be broken down during operation and behave as an impedance. A similar behaviour of the PV system is observed when a didode is activated. So for simplicity we consider the activation of the diode as a fault since the IV curve symptom is similar. Figure 6.4 shows a schematic of a group of cells (jth group) in which the bypass

diode is replaced by an element that can, at each time, take one of the diode's failed states: Short circuit, open circuit, any impedance, and inverted diode.

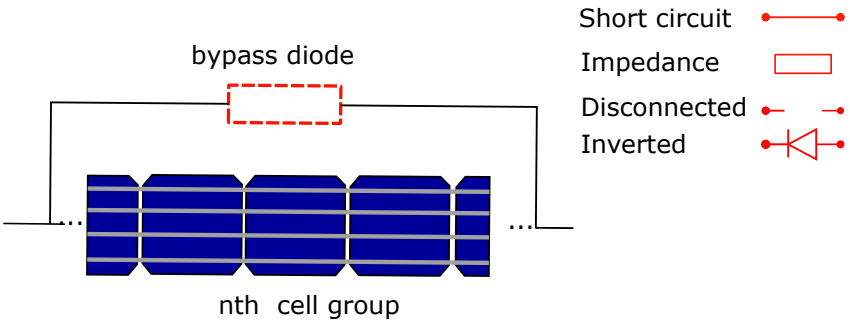

Figure 6.4: String PV cells connected to a bypass diode

6.3.3 Faulty connectors

The connection fault is related to an increasing connection resistance between two PV modules and is represented by the variation of the series resistance (Rs). In normal operation, this resistance is almost zero. The value of this resistance can be increased in several abnormal cases (corrosion of the connector, badly tightened screw, mechanical stress etc) but it can also represent the degradation within a PV module due to aging. In the extreme case, an infinite resistance can be used to represent a module that is disconnected from the PV string. The connection fault only comes into play at the stage of determining the characteristic of the string. Nonetheless, the representation of a degradated module can be obtained by the same variation of the Rs parameter.

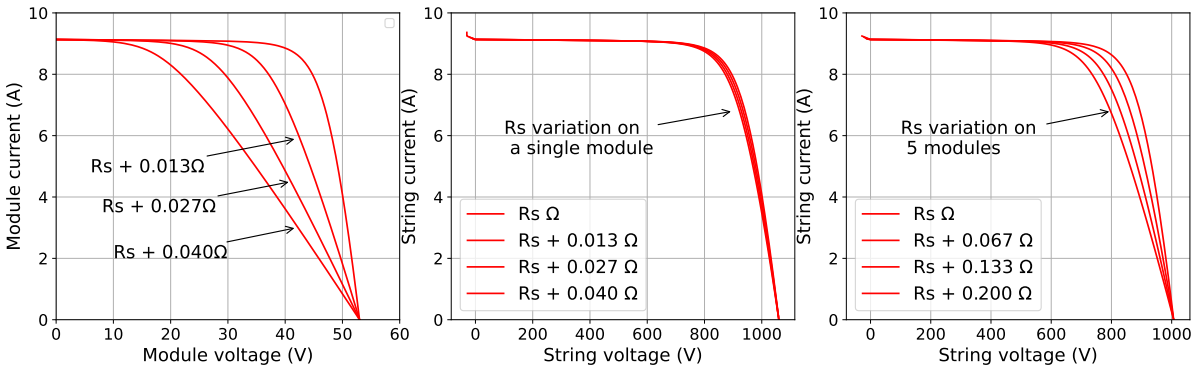

Figure 6.5

In Figure 6.5 the effect of the variation of the Rs parameter in a single module is modeled as well as the impact when connected to a string of 20 modules. The higher the connection resistance is, the more the string voltage drops for a given current. In fact it can be observed that an increase of the series resistance of 0.004 (7%) on a single module means a module power loss of 48% and a string power loss of 2.8%, but when having up to 5 modules with the same increased series resistance the string power loss will rise up to 14.5% .

6.4 Algorithm for Detection and classification of faults in a Photovoltaic Field

The ability to identify failures requires complex data analysis and decision making algorithms. Some parameterized algorithms are based on the knowledge from PV experts acquired by dealing with the system behavior contained in real PV data sets. In [58], a diagnostic method based on fuzzy logic detects faults such as shading, faulty series resistance, inverted bypass diode. In [59], a threshold-based method is used to diagnose photovoltaic modules. The ability of computers to replace humans in this task is a primary goal of fault detection systems to increase the speed and accuracy of fault identification.

The statistical performance monitoring based on artificial intelligence (AI) principles is becoming more convenient while the new generation of hardware and data storage systems become more affordable.The field of machine learning allows to identify and predict faults through a variety of computational processes provided. In the development of PV fault detection systems, various machine learning principles are explored to identify the algorithm that provides the best results for predicting PV faults[60][61].

In the previous section we have shown the possible symptoms that can be used to trace the nature of the defects. These symptoms are identified using the classification algorithm by training with the IV curves of a PV field under fault conditions and their respective label. As study case scenario, a system consisting of 20 bifacial modules is simulated, which generally corresponds to the case of a string in a conventional large-scale PV system. For the fault generation, the cases mentioned in the previous sections are simulated under different conditions of irradiance and temperature.

6.4.1 Methodology: Constructing a synthetic dataset of PV modules string failure

The dataset contains 3,000 individual IV curves. Each failure type is represented by 600 individual samples. To avoid over-fitting and having a robust model, we follow the best practices on training neural networks by splitting the dataset in training, validation and test sets (with 70%, 20%, 10% respectively). The simulated irradiance and temperature were input to simulation chain (combined electrical,thermal submodels) to obtain the IV curve of the PV system simulated. To obtained the faulty IV curve some cells were input to a zero value of irradiance to effectively activate the bypass diode. Also the parameters of Rs, Rp where modified as follows:

1. For simulation the symptom of reduction of the parallel resistance (Rp) the value of Rp was decreased up to 2% of its initial value. Four values within this range were considered.

2. To modify the the series resistance an incremental was added to the healthy curve rs value up to 7% of its initial value.

3. For the analysis of the defective diode the modules PV cells were shadowed in order to activate from 1 to 3 by pass diode. This way different curves are obtained for each failure case.

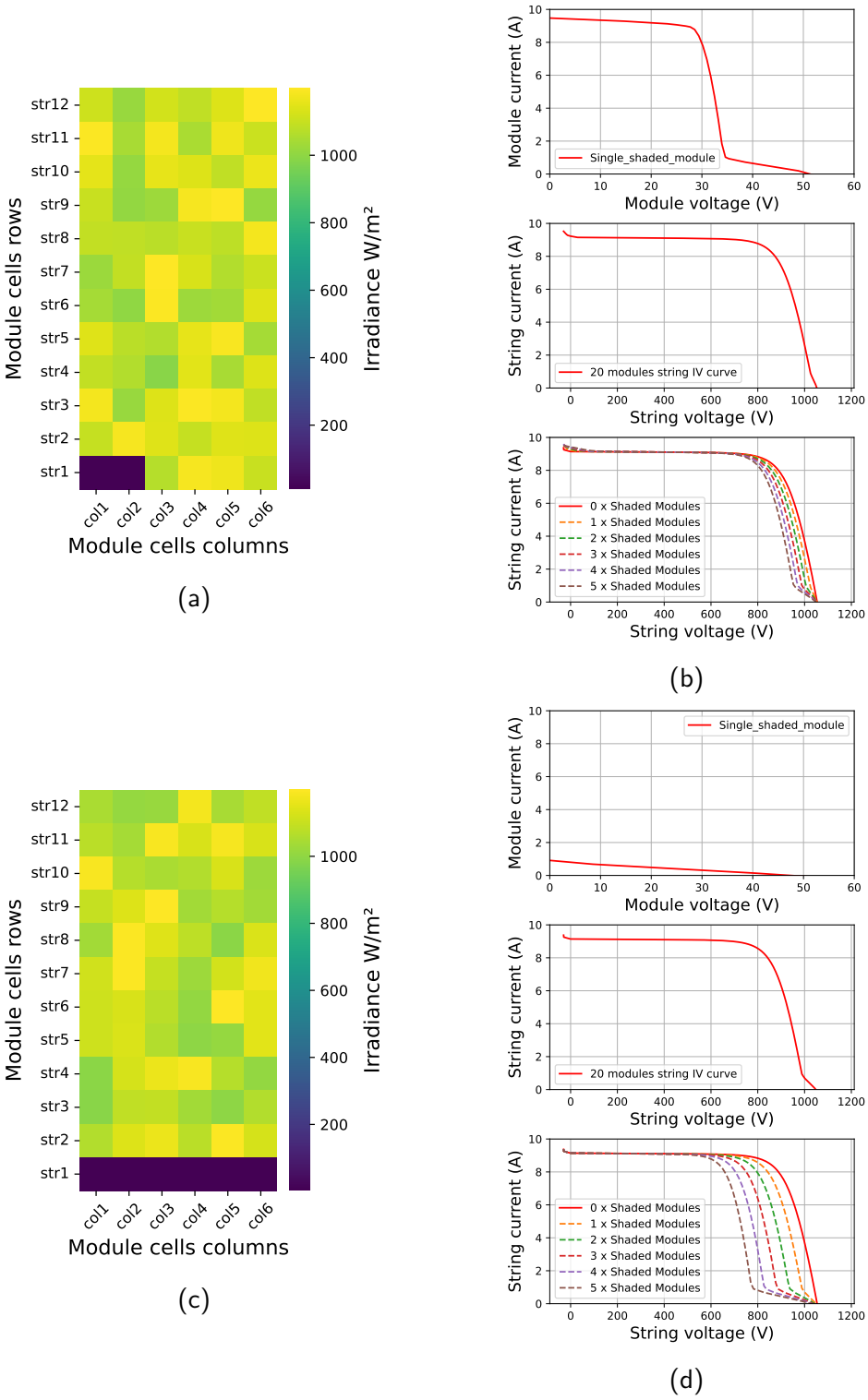

Figure 6.6: Figures (a) and (c) show the distribution of the incident (front) irradiance on the cells modules when 2 and 6 cells are shaded and the bypass diodes are activated. Figures (b) and (d) show the effect of the corresponding activated diodes on the IV curve of a single module and on the IV curve of the string of 20 modules when up to 5 modules are under the same condition of shadowing.

6.4.2 Training a neural network to automatically detect string failure

Neural networks have been taking almost all classification problems in recent years, from Alexnet [62] in computer vision to Transformers [63] in natural language processing. For time series data, the adoption of neural networks to solve classification problems has been in development since the early 90's and has made steady progress in the recent years. This has been tied to the enormous amounts of time series data that industry produces: healthcare, activity recognition, security, energy [64]. Specifically in the renewable energy sector, neural networks are used for almost any imaginable application, from forecasting, to classification and regression.

For our use case, there has been various attempts at detecting failures using machine learning, mostly based on real datasets from PV installations.

In this work we present a novel approach where the data comes from a physical end-2-end simulation.

As our particular problem of detecting failures on PV strings is relatively small, we will use a simple neural network proposed by [64], which offers a good compromise between complexity and speed.

The model

The neural network is of the type called Convolutional Neural Network (CNN) where we pass the input timeseries through a series of convolutional kernels (some citation here) that reduces the features of the signal progressively. We also interleave batch norm layers to make training more stable and not have to deal with exploding gradients. This is a standard best-practice on modern neural networks. Finally we attach a pooling layer and a dense classifier head. This type of models is very effective and has good results on standard time series benchmarks like UCR [65][66].

To train the model we use the Adam optimizer and cross entropy loss for 100 epochs using a reduce learning rate on plateau (we progressively reduce the learning rate when stale) and early stopping (we stop the training if the validation loss doesn't decrease anymore). As this is a classification task, we monitor the validation accuracy (percentage of corrected classified samples). The model is trained using the framework Keras with common best practices, the training script can be found here[1].

[1] `https://colab.research.google.com/drive/1OZkdaFU9Pkol_cfuCFm3Cgo0eas1FM7j?usp=sharing`

Table 6.2: Detailed model description: Layers, Number of parameters and tensor shapes.

Layer Type	Parameter count	Tensor shapes
Conv1D	448	199, 64
BatchNormalization	256	199, 64
ReLU	0	199, 64
Conv1D	12352	199, 64
BatchNormalization	256	199, 64
ReLU	0	199, 64
Conv1D	12352	199, 64
BatchNormalization	256	199, 64
ReLU	0	199, 64
GlobalAveragePooling1D	0	64
Dense	130	2

6.4.3 Results

We performed the experiment multiple times and used industry standard experiment tracking tools Weights and Biases to manage our project, an interactive view of the different runs can be seen here[2]). Relevant training/validation metrics are present on Figure (6.7)

Figure 6.7: Summary of the relevant training/validation metrics. Average of multiple runs.

From Table 6.8 we can observe that the network has no problem in identifying correctly the three types of failure (**rs**, **rp** and **diode**), achieving and amazing 100%, but it is not capable of separating between the three cases of diode failure. The later is a reasonable outcome, as CNN have a hard time counting objects/events, this is probably more suitable for an object detection architecture.

[2] `https://wandb.ai/capecape/ts_failure_detection`

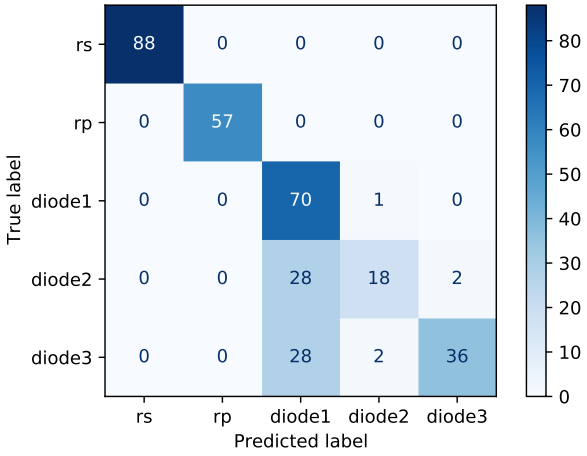

Figure 6.8: Confusion matrix on the trained model. Each row of the matrix represents the instances in an actual class while each column represents the instances in a predicted class.

..

CHAPTER 7

Conclusions and perspectives

In recent years, the increased interest in in the pursuit of new sources of sustainable and renewable energy has led to a faster development of photovoltaic energies, particularly of new more efficient technologies. In this context, the bifacial technology, has been driven to a rapid growth of its market share, and is now expected to become one of the leading photovoltaic technologies in the world. The present work helps to overcome some of the challenges faced by bifacial technology to get the confidence of investors.

This work contributes to the ongoing task of performance modeling and validation of bifacial PV systems models, whether fixed or tracking by the implementation of a simulation framework for bifacial PV systems based on a combination of existing optical, thermal and electrical models. It is crucial for the energy performance optimization and LCOE determination of bifacial PV systems.

Throughout the thesis, the validation of these sub-models is shown for different geographical locations, module layouts and cell concepts. Two main optical models based on view factors and ray tracing are considered when modeling the irradiance in bifacial PV systems. The thesis validates the developed models and shows a benchmarking between the main models developed by research institutes. The validations were performed through the setup made up of different bifacial technologies, and specialized high accuracy equipment for measuring the output power along with irradiance sensors placed in the plane of the array.

Within this work the validations were made by comparing localized measured irradiance and also by comparing the dc power and energy yield from both PV modules and strings. It has been found a corresponding correlation on the deviations between measured and modeled rear irradiance data, and the deviations in terms of the energy yield and bifacial gain of the bifacial PV systems.

A long-term validation of the thermal model with measured data from three bifacial technologies has shown good agreement with a very slight tendency to overestimate the operating temperature of the bifacial module. From the measurements of the modules under real con-

ditions of operation, the difference between the operating temperature of monofacial and the three different bifacial modules placed at the same location were compared for several months. The results have shown that bifacial modules can operate at the same temperature as the monofacial module or even lower. On the other hand, it has not been found any significant difference between the operating temperature of bifacial technologies, either installed in a tracking system or in a fixed tilt installation. It means, first that even having different temperature coefficients the differences in the operating temperature of bifacial technologies were not significant. Secondly, the additional back irradiation on the bifacial module will not necessarily cause the bifacial module to operate at a higher temperature than the monofacial module.

The measured power of three different bifacial technologies, HET (heterojunction), nPERT and PERC+, placed in the center of the fixed tilt array surrounded by rows and neighboring modules under real conditions of operation, was compared to the modeled power by input of the modeled irradiance by RT and VF. The results have shown good agreement with the measured data for RT, 2DVF, nonetheless an overestimation over +5% was found when calculating the annual energy yield by input of the irradiance from 3DVF approach. This highlights the importance of incorporating the effect of the support structure on the array backside incident irradiance. As an interesting result it was found that the power calculated by using the 2DVF approach results in a good agreement with the measured energy yield even though it involves a small test bench. This indicates that a simulation of 8 modules in a 2L landscape configuration is adequate to achieve good results using 2DVF. These results are in agreement with those of other authors where they compare installations of similar dimensions.

As an application of modeling chain, a synthetic data base was generated in order to explore the use for PV plant faults classification and detection. The simulation of a faulty string shows that the impact of three types of failures can reduce the power by 20%. The implementation of an algorithm based on neuronal networks results a good approach for the classification of symptom, an important step for further determination of the failure type in a PV plant.

The results of this dissertation reveal the potential areas for development in the task of simulation of the performance of bifacial systems. The validation of large bifacial PV systems under different distributions and at high albedo values is needed as in this scenario, the rear irradiance has a very high impact on the overall energy production of the bifacial PV systems. As the investors are being convinced of the potential of bifacial technologies, the affordable application range is getting wider and this is how the vertical mounting of bifacial modules are gaining relevance. Further validation with different orientations, and ground albedos should be considered. Large linear PV plans are implementing vertical installations, which have the advantage of widening the generation profile. Also different ground shapes and angles for optimized back reflected irradiance in combination with vertical installations could be an interesting subject to be further explored.

APPENDIX A

Appendix

A.1 Electrical modeling

A 72 PV cells laminated bifacial HJT module was fabricated at CEA-INES for outdoor and indoor characterization purposes. The indoor measurements for validation of methodology presented in section 3.3 were performed by a $PasanMeyerBurgerHighLight3$ solar simulator under different irradiances of 1000,700,200 as shown in Table A.1. The single side indoor measurements from front and rear side are input to the algorithm presented in section 3.3 for the estimation of the module electrical parameters.

The indoor measurements values used for the calculation of the electrical output parameters will lead to a certain level of accuracy for a given incident irradiance and module temperature. The choice of the front and rear indoor measurement leading to the lowest error is evaluated by calculating the RMSE of the curve fit to the measured Pmpp (and Voc) and the simulated results.

Table A.1: Indoor measurements performed for front and rear side of HET dedicated module for validation of Mpp calculation.

Side	G (W/m^2)	Isc (A)	FF %	Voc (V)	Rs Ω	Rsh Ω	Pmpp (W)	Vmpp (V)	Impp (A)	Tcell (°C)
frontside	1002.02	9.14	75.71	53.01	0.63	399.10	366.82	43.08	8.52	24.77
	202.49	1.83	55.63	69.64	26.68	1581.71	70.72	41.56	1.70	24.77
	703.23	6.37	76.92	52.43	0.81	763.99	257.07	43.06	5.97	24.68
rearside	1002.66	8.13	76.00	52.82	0.67	324.20	326.23	43.07	7.57	24.86
	203.27	1.63	56.25	68.35	29.05	1818.10	62.70	41.30	1.52	24.95
	704.00	5.67	76.85	52.27	0.92	772.70	227.62	43.00	5.29	24.86

Since at indoor conditions only single sided measurements are possible at a time, the simulated electrical output results of the module are calculated considering the front G_f or

rear G_r side incident irradiance as zero at a time in order to compare the simulation output with the measured output. The Figure A.1.1 shows the simulation results of the output electrical parameters considering an incident irradiance $G_r = 0$ and $G_f = 0$.

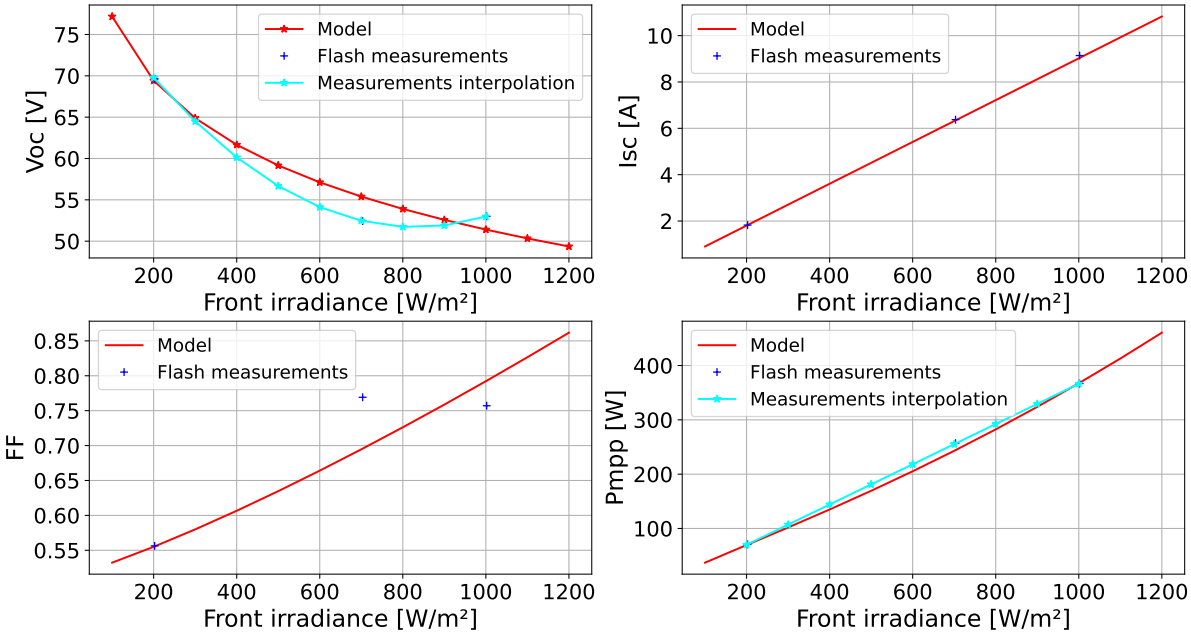

(a) Electrical parameters calculated for an incident irradiance G_f =[100,1200] and $G_r = 0$

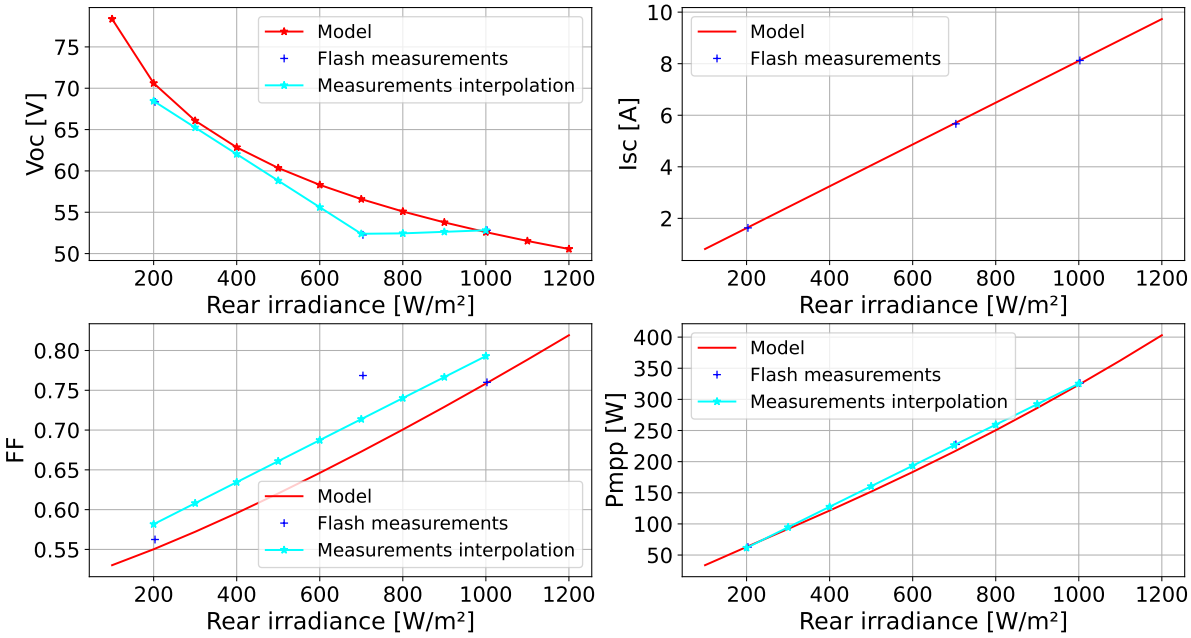

(b) Electrical parameters calculated for an incident irradiance G_r =[100,1200] and $G_f = 0$

Figure A.1.1: Simulated electrical parameters obtained by the method presented in section 3.3 for an incident irradiance from 100 to 1200 W/m² on the front side (a) and rear side (b)

The measured rear and front POA irradiance at the fixed tilted test bench installed at the Plataforma Solar del Desierto de Atacama (PSDA), Chile, are used for the evaluation of

the bifacial output DC power $Pmpp, bi$. The single sided measurements at STC of the PV module installed are used required by the algorithm.

The results of the validations for a five minutes time interval simulations are compared with measured outdoor $Pmpp, bi$ in Figure A.1.2 and A.1.3.

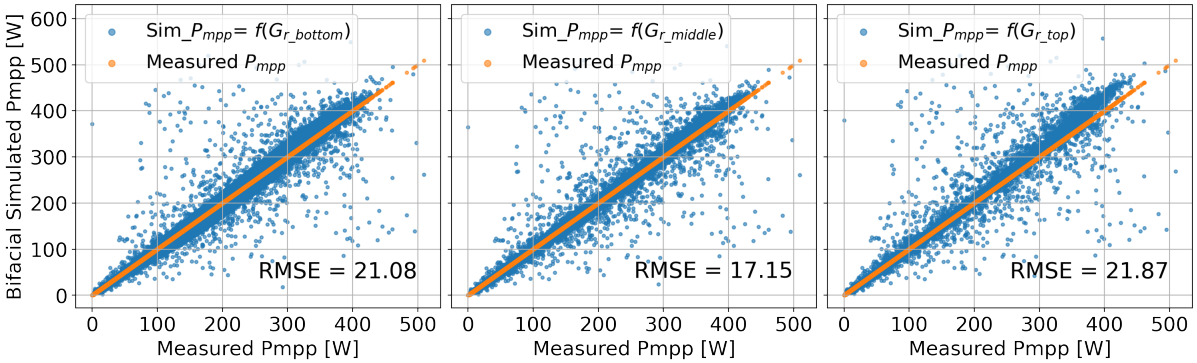

Figure A.1.2: Annual simulation of $Pmpp, bi$ for a fixed tilt bifacial module at the PSDA using as input the measured irradiance by the reference cells located at the top, middle and bottom of the test bench.

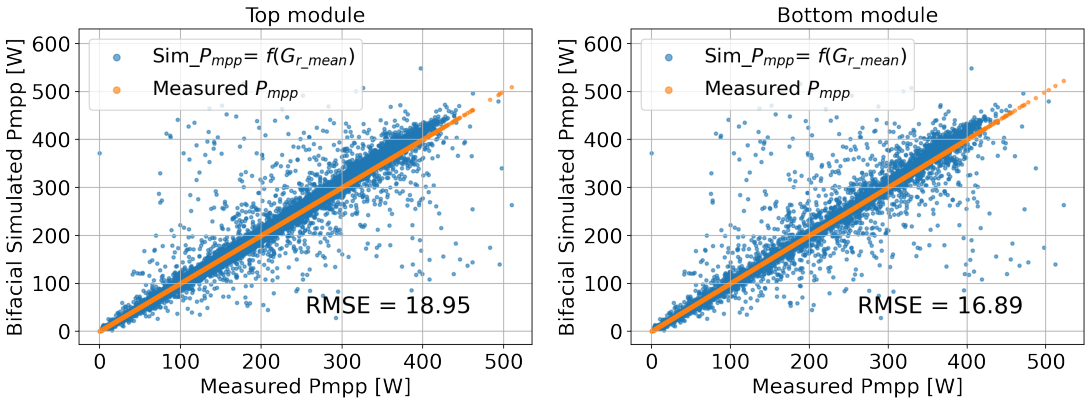

(a) Top module (b) Bottom module

Figure A.1.3: Annual simulation results of $Pmpp, bi$ for top and bottom module at the fixed tilt test bench by input the POA mean measured rear irradiance

A.2 Rear irradiance measurements

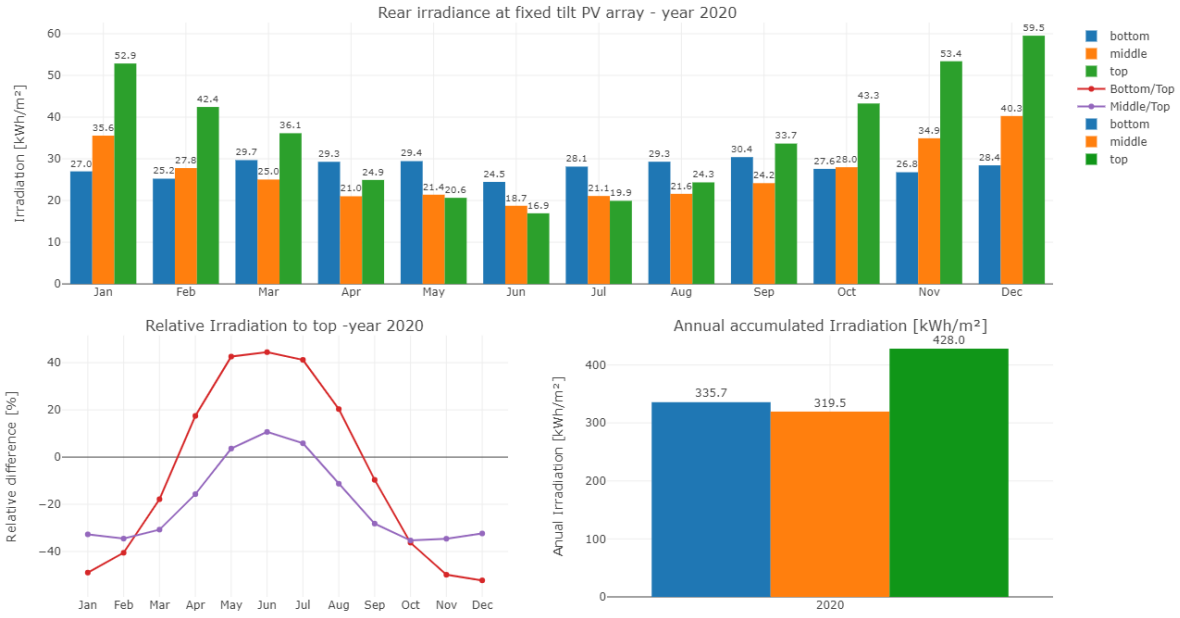

Figure A.2.1: Measured rear irradiance throughout the year 2020 for the top, middle and bottom position at the fixed test bench at the PSDA in the Atacama desert.

A.3 Large Scale PV plant Layout

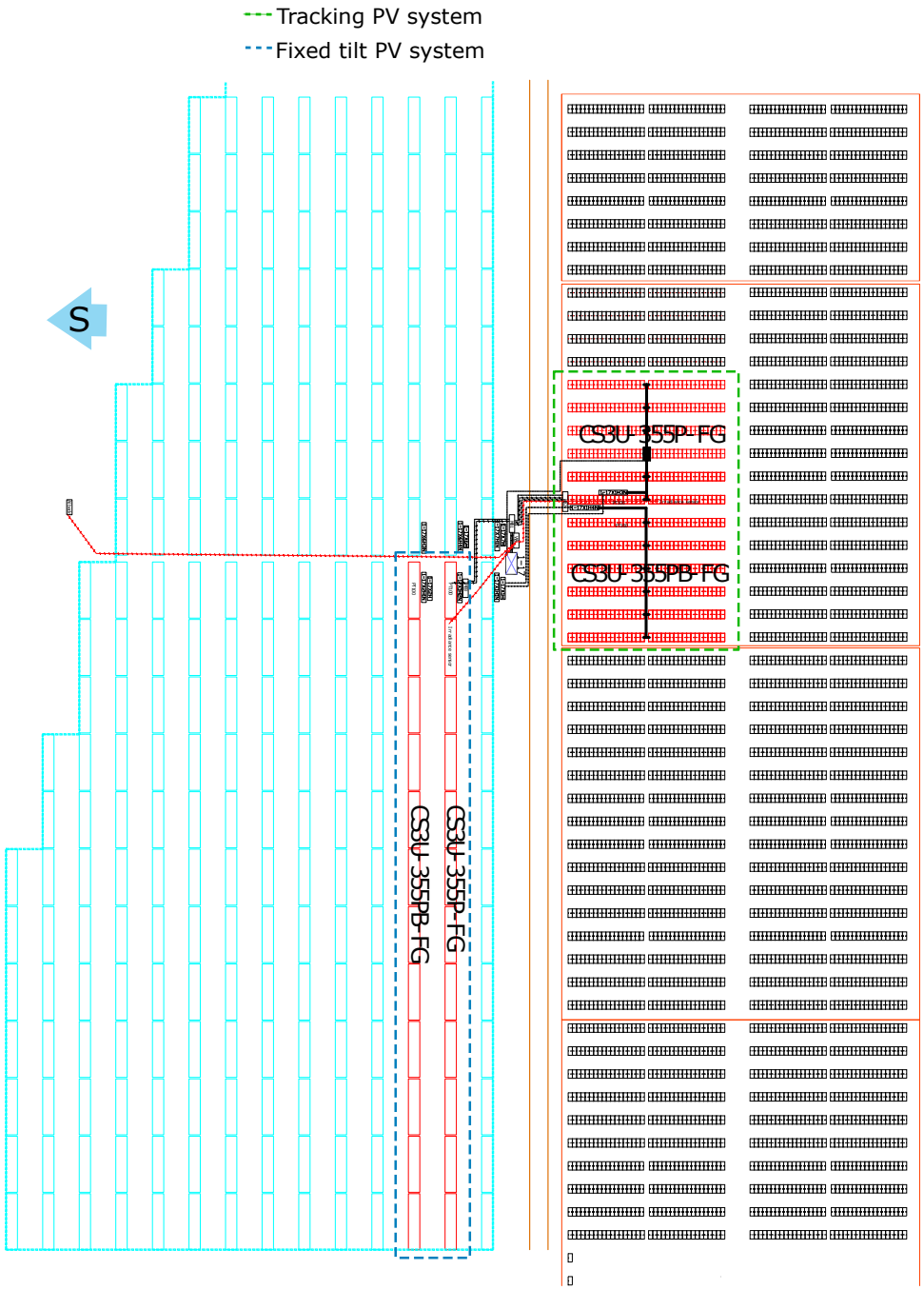

Figure A.3.2: Large scale PV plant installed at Wuhai, Chine. Courtesy: Canadian Solar.

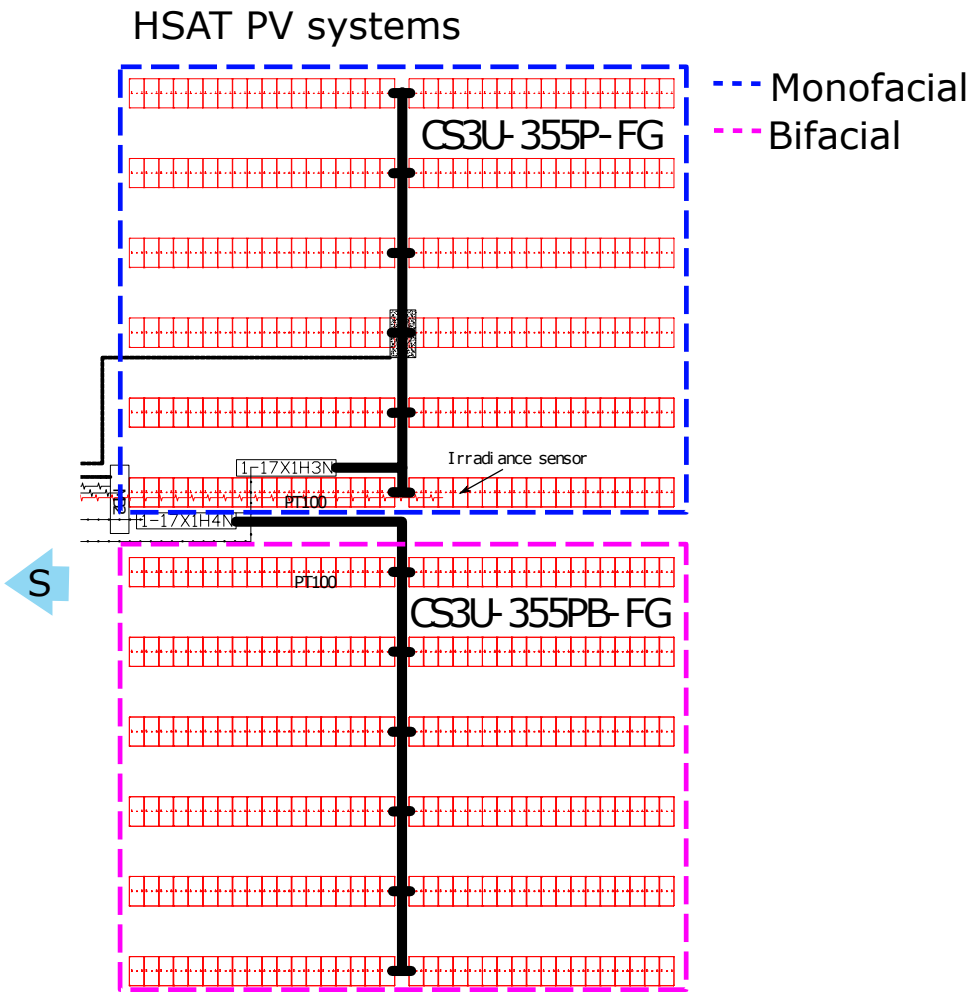

Figure A.3.3: Layout of the tracking system of the large scale PV plant installed at Wuhai, Chine. Courtesy: Canadian Solar.

A.4 Uncertainty calculation

Accordingly to the manufacturer, the irradiance value (E in Wm^{-2}) can be calculated by simply dividing the output signal (U_{emf} in V) of the pyranometer by its sensitivity ($VW^{-1}m^2$) as follows,

$$E = \frac{U_{emf}}{Sensitivity} \tag{A.1}$$

The GUM states that the input quantities are inferred from the statistical analysis of several observations or by means of scientific judgement (type B). Since no information is given by the manufacturers regarding the quantities presented in the specifications sheet, all the inputs are considered as type B. For a type B evaluation of uncertainty,the GUM recommends to use a rectangular or uniform probability distribution when the only information is specified in a range interval as is the case of the datasheet for a Kipp&Zonnen pyranometer. In addition, the uncertainty sources of the model in equation A.1 are applied to both the input, output parameters. The uncertainty sources related to each parameter are presented in the table A.2

The considered uncertainty sources to include are described as follows.

The voltage output of the pyranometer is measured with a data logger. The accuracy is specified for a range of temperature of operation and for our case of 12 μV.

For the sensitivity, the value is specified by the manufacturer as 14.00 μV/W/m². The sensitivity is established under reference conditions i.e., 20 °C instrument temperature, normal incidence solar radiation, horizontal mounting and an irradiance level of 500 W/m². In practice, because all data points deviate from the reference conditions, the instrument characteristics have to be included in the uncertainty calculation. From the list of characteristics specified by the manufacturers, the following apply to the input quantity sensitivity S,

- non-stability, the percentage change in sensitivity per year, relevant if the instrument has not been recalibrated recently.
- non-linearity, the change in sensitivity of the instrument for irradiance levels other than the reference condition (500 W/m²) between 100 and 1000 W/m².
- temperature response, the change in sensitivity of the instrument for temperatures other than the reference condition (20 °C).
- tilt response, the change in sensitivity of the instrument for mounting orientations other than the reference condition (horizontal).

Considering the regular daily cleaning of the sensor used for the analysis (installed at the PSDA), we follow the estimation of the uncertainty related to the maintenance in [reference], where a maximum contribution of 0.5% is estimated. For the contribution of the output global horizontal irradiance the following sources are considered,

- zero off-set a, the response to net thermal radiation.
- zero off-set b, the response to temperature gradients.
- directional response, the error caused by assuming the sensitivity to a normal incidence beam of irradiance is valid when measuring beams coming from any direction.

According to the GUM [Reference GUM] the standard uncertainty of a quantity is the square root of the sum of the squares of all uncertainty sources of that measurand. As proposed in [reference Jorgen Konnings], the one-sided specification limits are treated as symmetric.

$$u_c(E) = \sqrt{\sum_{i=1}^{N} \left(\frac{\delta f}{\delta x_i}\right) \times u^2(x_i)} \tag{A.2}$$

Therefore the sensitivity coefficients C_V, C_S and C_E are combined by the above equation,

$$u_c(E) = \sqrt{C_V^2 \times u^2(V) + C_S^2 \times u^2(S) + C_E^2 \times u^2(E)} \tag{A.3}$$

Table A.2: Uncertainty sources, specification limits and probability distribution. From[reference Kipp&Zonnen]

Uncertainty source	Parameter	Specification limit	Type	Distribution	Shape
Data logger accuracy[1]	V	12μ V	B	Rectangular	symmetric
calibration uncertainty	S	1.5%	B	normal (k=2)	symmetric
non-stability	S	0.5%	B	rectangular	one-sided (negative)
non-linearity	S	0.2%	B	rectangular	symmetric
temperature response	S	1%	B	rectangular	symmetric
maintenance	S	0.5%	B	rectangular	symmetric
zero off-set a	E	7 W/m²	B	rectangular	one-sided (negative)
zero off-set b	E	2 W/m²	B	rectangular	symmetric
directional response	E	10 W/m²	B	rectangular	symmetric

A.5 Default diagnostic on bifacial PV systems

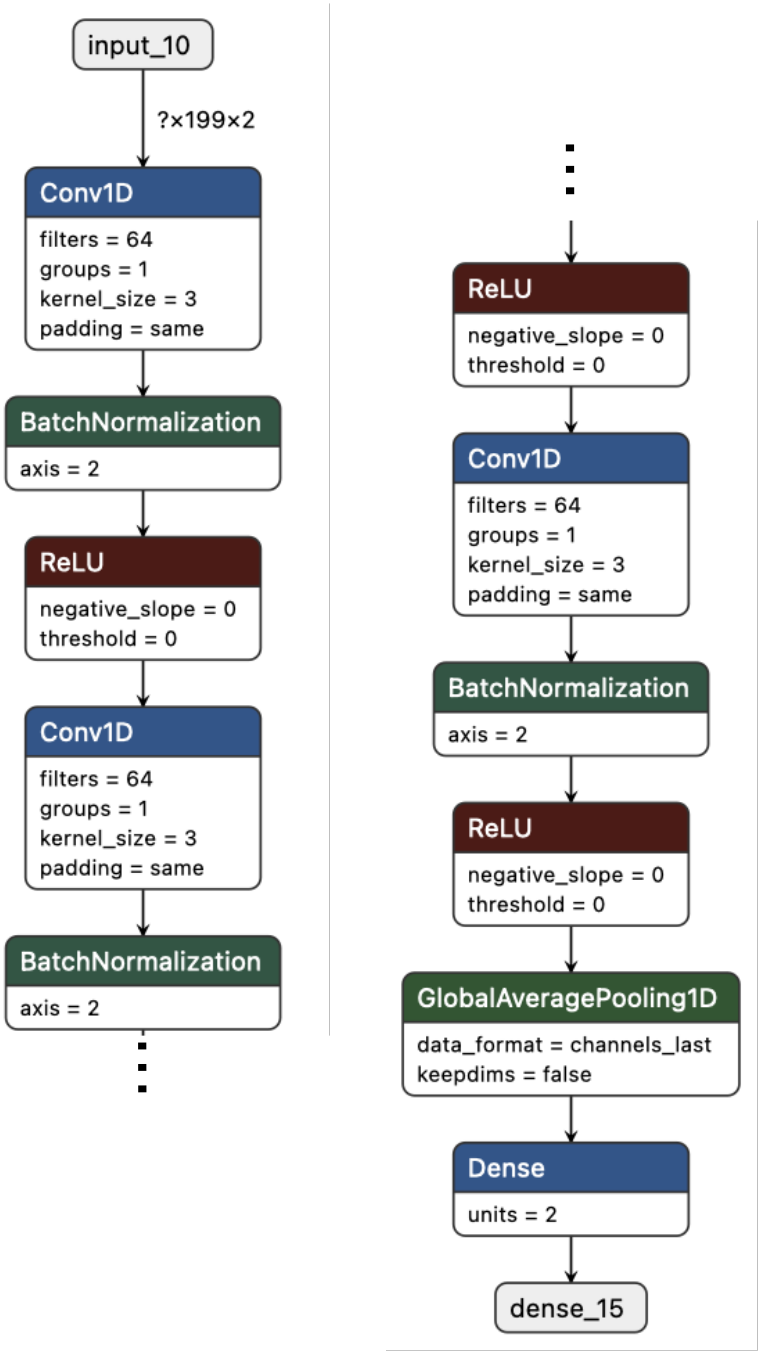

Figure A.5.1: A diagram of the CNN model used to detect failures.

Bibliography

[1] Myles R Allen et al. *Framing and Context. In: Global Warming of 1.5°C. An IPCC Special Report on the impacts of global warming of 1.5°C above pre-industrial levels and related global greenhouse gas emission pathways, in the context of strengthening the global response to the threat of climate change, sustainable development, and efforts to eradicate poverty*.

[2] globalcarbonproject. *globalcarbonproject*. URL: https://www.globalcarbonproject.org/. (accessed: 04.02.2022).

[3] International Renewable Energy Agency. *World Energy Transitions Outlook 2022: 1.5°C Pathway*. 2022. ISBN: 9789292604295. URL: www.irena.org.

[4] International Energy Agency. *Net Zero by 2050 - A Roadmap for the Global Energy Sector*. 2050. URL: www.iea.org/t&c/.

[5] IEC TS 60904-1-2:2019. *"Photovoltaic devices - part 1-2: Measurement of current-voltage characteristics of bifacial photovoltaic (pv) devices."*. URL: https://webstore.iec.ch/publication/34357&preview.

[6] International Renewable Energy Agency. *Termografía de alta temperatura en el contexto de radiación solar concentrada*. 2013. ISBN: 978-84-7834-691-2.

[7] Kreith Frank Kreider F. Yogi Goswami. *Goswami, D. Y. (2000) Principles of Solar Engineering.pdf*.

[8] John A Duffie and W A Beckman. *Solar Engineering of Thermal Processes*. Vol. 53. 2006, p. 908. ISBN: 0471698679. DOI: 10.1119/1.14178. URL: http://link.aip.org/link/?AJP/53/382/1&Agg=doi.

[9] Michael Gostein, Bill Marion, and Bill Stueve. "Spectral Effects in Albedo and Rearside Irradiance Measurement for Bifacial Performance Estimation". In: *Conference Record of the IEEE Photovoltaic Specialists Conference* 2020-June (2020), pp. 0515–0519. ISSN: 01608371. DOI: 10.1109/PVSC45281.2020.9300518.

[10] Raghu Vamsi Krishna Chavali, Stefaan De Wolf, and Muhammad Alam. "Device physics underlying silicon heterojunction and passivating-contact solar cells: A topical review". In: *Progress in Photovoltaics: Research and Applications* 26 (Jan. 2018). DOI: 10.1002/pip.2959.

[11] Keiichiro Masuko et al. "Achievement of More Than 25% Conversion Efficiency With Crystalline Silicon Heterojunction Solar Cell". In: *IEEE Journal of Photovoltaics* 4 (Nov. 2014), pp. 1433–1435. DOI: 10.1109/JPHOTOV.2014.2352151.

[12] Martin A. Green et al. "Solar cell efficiency tables (version 59)". In: *Progress in Photovoltaics: Research and Applications* 30.1 (Nov. 2021), pp. 3–12. DOI: 10.1002/pip.3506. URL: https://doi.org/10.1002/pip.3506.

[13] Radovan Kopecek and Joris Libal. "Summary and outlook". In: (2018), pp. 293–297.

[14] Raghu Vamsi Krishna Chavali et al. "Multiprobe Characterization of Inversion Charge for Self-Consistent Parameterization of HIT Cells". In: *Photovoltaics, IEEE Journal of* 5 (May 2015), pp. 725–735. DOI: 10.1109/JPHOTOV.2014.2388072.

[15] VDMA. "Internaternational Technology Roadmap for Phothotovoltaic (ITRPV)". In: (). URL: https://www.vdma.org/viewer/-/v2article/render/50902381.

[16] Radovan Kopecek and Joris Libal. *Bifacial photovoltaics 2021: Status, opportunities and challenges*. Apr. 2021. DOI: 10.3390/en14082076.

[17] Jorge Rabanal-Arabach. *Development of a c-Si Photovoltaic Module for Desert Climates*. 2019. URL: http://nbn-resolving.de/urn:nbn:de:bsz:352-2-l3mvyvipnwzl6.

[18] W. De Soto, S. A. Klein, and W. A. Beckman. "Improvement and validation of a model for photovoltaic array performance". In: *Solar Energy* 80 (1 2006), pp. 78–88. ISSN: 0038092X. DOI: 10.1016/j.solener.2005.06.010.

[19] Jorge Rabanal-Arabach. *Photovoltaic devices - Part 1: Measurement of photovoltaic current-voltage characteristics*. 2006, (cited on page 12).

[20] Christian Gueymard. "An anisotropic solar irradiance model for tilted surfaces and its comparison with selected engineering algorithms". In: *Solar Energy* 38 (5 1987), pp. 367–386. ISSN: 0038092X. DOI: 10.1016/0038-092X(87)90009-0.

[21] Christian A. Gueymard. "Cloud and albedo enhancement impacts on solar irradiance using high-frequency measurements from thermopile and photodiode radiometers. Part 2: Performance of separation and transposition models for global tilted irradiance". In: *Solar Energy* 153 (2017), pp. 766–779. ISSN: 0038092X. DOI: 10.1016/j.solener.2017.04.068. URL: http://dx.doi.org/10.1016/j.solener.2017.04.068.

[22] Matthew Lave et al. "Evaluation of GHI to POA Models at Locations across the United States". In: *IEEE Journal of Photovoltaics* 5 (2 2015), pp. 597–606. DOI: 10.1109/JPHOTOV.2015.2392938. URL: https://ieeexplore.ieee.org/abstract/document/7035020.

[23] R. Perez, R. Seals, and J. Michalsky. "All-weather model for sky luminance distribution-Preliminary configuration and validation". In: *Solar Energy* 50 (3 1993), pp. 235–245. ISSN: 0038092X. DOI: 10.1016/0038-092X(93)90017-I.

[24] Richard Perez et al. "Modeling daylight availability and irradiance components from direct and global irradiance". In: *Solar Energy* 44 (5 1990), pp. 271–289. ISSN: 0038092X. DOI: 10.1016/0038-092X(90)90055-H.

[25] T.L. Bergman et al. *Fundamentals of Heat and Mass Transfer*. Wiley, 2011. ISBN: 9780470501979. URL: https://books.google.fr/books?id=vvyIoXEywMoC.

[26] "Analysis of irradiance models for bifacial PV modules". In: *2017 IEEE 44th Photovoltaic Specialist Conference, PVSC 2017* (2017), pp. 1–6. DOI: 10.1109/PVSC.2017.8366322.

[27] Sara MacAlpine et al. "A Practical Irradiance Model for Bifacial PV Modules". In: (June 2018), pp. 1537–1542. DOI: 10.1109/pvsc.2017.8366263.

[28] Marc Abou Anoma et al. "View Factor Model and Validation for Bifacial PV and Diffuse Shade on Single-Axis Trackers". In: *2017 IEEE 44th Photovoltaic Specialist Conference, PVSC 2017* (2017), pp. 1549–1554. DOI: 10.1109/PVSC.2017.8366704.

[29] André Mermoud, Bruno Wittmer BrunoWittmer, and pvsyst com. *PVSYST SA-Route du Bifacial shed simulations with PVsyst*. URL: www.pvsyst.com.

[30] Ufuk Alper Yusufoglu et al. "Simulation of energy production by bifacial modules with revision of ground reflection". In: *Energy Procedia* 55 (2014), pp. 389–395. ISSN: 18766102. DOI: 10.1016/j.egypro.2014.08.111.

[31] ARNO KRENZINGER and EDUARDO LORENZO. "Estimation of Radiation Incident on Bifacial Albedo-Collecting Panels". In: *International Journal of Solar Energy* 4.5 (Jan. 1986), pp. 297–319. DOI: 10.1080/01425918608909865. URL: https://doi.org/10.1080/01425918608909865.

[32] Bill Marion et al. "A Practical Irradiance Model for Bifacial PV Modules". In: *2017 IEEE 44th Photovoltaic Specialist Conference (PVSC)*. IEEE, June 2017. DOI: 10.1109/pvsc.2017.8366263. URL: https://doi.org/10.1109/pvsc.2017.8366263.

[33] PVlighthouse. *Sunsolve*. URL: https://www.pvlighthouse.com.au/sunsolve. (accessed: 12.01.2022).

[34] Matthieu Chiodetti and Patrick Dupeyrat. "A ray-tracing based 3D tool for accurate prediction of PV plants yield". In: (September 2019), pp. 2–3. DOI: 10.13140/RG.2.2.28162.02249.

[35] Gregory J. Ward Larson. "Rendering with Radiance : A Practical Tool for Global Illumination". In: (1998), p. 129. URL: http://radsite.lbl.gov/radiance/refer/s98c33.pdf.

[36] Simone Crone. "Radiance users manual". In: *Glass* (November 1992).

[37] Silvana Ayala Peláez. "Bifacial Solar Panels System Design, Modeling, and Performance". In: (2019). URL: https://search-proquest-com.liverpool.idm.oclc.org/docview/2166890580.

[38] Amir Asgharzadeh Shishavan. "Bifacial photovoltaic (PV) system performance modeling utilizing ray tracing". In: (2019). URL: https://ir.uiowa.edu/etd/6911%5C%0Ahttps://iro.uiowa.edu/discovery/fulldisplay/alma9983777087002771/01IOWA_INST:ResearchRepository.

[39] R.G. Jnr. Ross and M.I. Smokler. "Flat-Plate Solar Array Project Final Report". In: (1986). ¡br /¿, pp. 86–31.

[40] Sandia. *Sandia module temperature model.* URL: https://pvpmc.sandia.gov/modeling-steps/2-dc-module-iv/module-temperature/sandia-module-temperature-model/. (accessed: 01.02.2020).

[41] David Faiman. "Assessing the Outdoor Operating Temperature of Photovoltaic Modules". In: *Progress in Photovoltaics: Research and Applications* 16 (June 2008), pp. 307–315. DOI: 10.1002/pip.813.

[42] A. Pandiyan. "Automated data evaluation and performance modelling of bifacial solar modules". MA thesis. 2017.

[43] Yong Sheng Khoo et al. "Method for quantifying optical parasitic absorptance loss of glass and encapsulant materials of silicon wafer based photovoltaic modules". In: *Solar Energy Materials and Solar Cells* 102 (2012). Organic, Dye sensitized and Innovative approaches for Photovoltaic Applications, pp. 153–158. ISSN: 0927-0248. DOI: https://doi.org/10.1016/j.solmat.2012.03.008. URL: https://www.sciencedirect.com/science/article/pii/S0927024812001146.

[44] Soteris A. Kalogirou. "Chapter 9 - Photovoltaic Systems". In: *Solar Energy Engineering (Second Edition)*. Ed. by Soteris A. Kalogirou. Second Edition. Boston: Academic Press, 2014, pp. 481–540. ISBN: 978-0-12-397270-5. DOI: https://doi.org/10.1016/B978-0-12-397270-5.00009-1. URL: https://www.sciencedirect.com/science/article/pii/B9780123972705000091.

[45] J. W. Bishop. "Computer simulation of the effects of electrical mismatches in photovoltaic cell interconnection circuits". In: *Solar Cells* 25 (1 1988), pp. 73–89. ISSN: 03796787. DOI: 10.1016/0379-6787(88)90059-2.

[46] Jai Prakash Singh, Armin G. Aberle, and Timothy M. Walsh. "Electrical characterization method for bifacial photovoltaic modules". In: *Solar Energy Materials and Solar Cells* 127 (2014), pp. 136–142. ISSN: 09270248. DOI: 10.1016/j.solmat.2014.04.017. URL: http://dx.doi.org/10.1016/j.solmat.2014.04.017.

[47] Giovanni Petrone, Carlos Ramos-Paja, and Giovanni Spagnuolo. *Photovoltaic Sources Modeling*. Mar. 2017. ISBN: 978-1-118-67903-6.

[48] Bennet Meyers, Mark Mikofski, and Mike Anderson. "A fast parameterized model for predicting PV system performance under partial shade conditions". In: *Conference Record of the IEEE Photovoltaic Specialists Conference* 2016-Novem (1 2016), pp. 3173–3178. ISSN: 01608371. DOI: 10.1109/PVSC.2016.7750251.

[49] Bennet Meyers and Mark Mikofski. "Accurate modeling of partially shaded PV arrays". In: *2017 IEEE 44th Photovoltaic Specialist Conference, PVSC 2017* 2017-June (2017), pp. 3354–3359. DOI: 10.1109/PVSC.2017.8521559.

[50] Joshua S. Stein et al. *Bifacial PV modules & systems Experience and Results from International Research and Pilot Applications*. 2021, p. 168. ISBN: 9783907281031.

[51] A. Aberle A. Hubner and R. Hezel. "Temperature behavior of monofacial and bifacial silicon solar cells". In: *Conferenc Twenty Sixth IEEE Photovoltaic Specialists Conference-1997* (1997), pp. 223–226. ISSN: 09270248. DOI: 10.1016/j.solmat.2018.05.033.

[52] Keith R. McIntosh et al. "Irradiance on the upper and lower modules of a two-high bifacial tracking system". In: *Conference Record of the IEEE Photovoltaic Specialists Conference* 2020-June (2020), pp. 1916–1923. ISSN: 01608371. DOI: 10.1109/PVSC45281.2020.9300838.

[53] Javier Guerrero Perez and Jose. Navarro Berbel. "BiTEC: How to simulate bifacial trackers". In: ().

[54] M. W.P.E. Lamers et al. "Temperature effects of bifacial modules: Hotter or cooler?" In: *Solar Energy Materials and Solar Cells* 185 (Oct. 2018), pp. 192–197. ISSN: 09270248. DOI: 10.1016/j.solmat.2018.05.033.

[55] Djaber Berrian. "Accuracy of Ray Tracing and View Factor Optical Models For Energy Yield Prediction of Fixed Tilt and Tracked Bifacial PV Systems". 2020.

[56] imt-solar. *imt-solar*. URL: https://www.imt-solar.com/. (accessed: 04.02.2022).

[57] M. Köntges et al. *Performance and reliability of photovoltaic systems subtask 3.2: Review of failures of photovoltaic modules: IEA PVPS task 13: external final report IEA-PVPS*. 2014, pp. 1–140. ISBN: 9783906042169.

[58] B. Abdesslam. "Etude et diagnostic des défauts fréquents aux systèmes photovoltaïques (PV) par emploi de la caractéristique courant-tension". In: *UNIVERSITE – SETIF-1-(ALGERIE), SETIF (ALGERIE)* (2017).

[59] L. BUN. "Thèse Génie éléctrique : "Détection et Localisation de Défauts pour un Système PV". 2006.

[60] Y.-S. Chen C.-C. Hsu J.-L. Li. "Time Fault Detection in Massive Multi-Array PV Plants Based on Machine Learning Techniques". In: *36th European Photovoltaic Solar Energy Conference and Exhibition* (2019).

[61] A. El Hajjaji M. Hassan Ali A. Rabhi and G. M. Tina. "Real Time Fault Detection in Photovoltaic Systems". In: *Energy Procedia* vol. 111 (2017), pp. 914–923.

[62] Alex Krizhevsky. "One weird trick for parallelizing convolutional neural networks". In: *CoRR* abs/1404.5997 (2014). arXiv: 1404.5997. URL: http://arxiv.org/abs/1404.5997.

[63] Ashish Vaswani et al. "Attention is All you Need". In: *Advances in Neural Information Processing Systems*. Ed. by I. Guyon et al. Vol. 30. Curran Associates, Inc., 2017. URL: https://proceedings.neurips.cc/paper/2017/file/3f5ee243547dee91fbd053c1c4a845Paper.pdf.

[64] Hassan Ismail Fawaz et al. "InceptionTime: Finding AlexNet for time series classification". In: *Data Mining and Knowledge Discovery* 34.6 (Sept. 2020), pp. 1936–1962. DOI: 10.1007/s10618-020-00710-y. URL: https://doi.org/10.1007%5C%2Fs10618-020-00710-y.

[65] Fazle Karim, Somshubra Majumdar, and Houshang Darabi. "Insights into LSTM Fully Convolutional Networks for Time Series Classification". In: (Feb. 2019). DOI: 10.1109/ACCESS.2019.2916828. URL: http://arxiv.org/abs/1902.10756%20http://dx.doi.org/10.1109/ACCESS.2019.2916828.

[66] Lei Cheng et al. "Classification of Long Sequential Data using Circular Dilated Convolutional Neural Networks". In: (Jan. 2022). URL: http://arxiv.org/abs/2201.02143.

List of Figures

List of Tables

Dissertation Contributions

The research in this dissertation has resulted in the following scientific work :

Conference Proceedings and Presentations

- F. Araya, H. Colin, "Behaviour of half-cell modules regarding inhomogeneous irradiance on the rear-face", IEEE PVSC 2021.
- F. Haffner, D.Berrian, F. Araya, et al. The ATACAMA desert in Chile as a bifacial hotspot: yield modelling within the ATAMOSTEC project PV Tech Power, ed. september 2020.
- F. Araya, F. Haffner, T. Capelle, H Colin, "Bifacial Optical Model Validation and Performance of Static and Tracked Systems Installed in the Atacama Desert" 37th EUPVSEC 2020.
- T. Capelle, F. Araya, F. Haffner, J. Sayritupac, H. Colin, "A comparison of bifacial PV system modelling tools" Bifacial PV Workshop, Amsterdam 2019.

Acknowledgments

Firstly, I would like to express my appreciation and gratitude to Hervé Colin for his guidance and the time he dedicated to supervising my work, Dra. Delfina Guzman and Thomas Capelle and his family for giving me generous support and encouragement during these years in France. Also, I would like to express in this document my sincere gratitude to my friend and Dr. Aitor Marzo for his willingness, passion, and support, especially when things became tedious and unclear.

My sincere thanks to the people at CEA-INES, where this work was carried out, and to my Ph.D. director Quoc Tran for the opportunity to write this thesis.

I would like to express my gratitude to the Centro de Desarrollo Energético Antofagasta (CDEA) and the Atamos Tec project for their generous disposition; without their help and assistance in the field, this work would not have been possible.

Last but not least, I would like to dedicate this work to my family, especially my parents and brothers, who were always there, providing the peace of mind and support needed to carry this challenge.

My most sincere thanks to those who helped me along my Ph.D.

Francisco Araya Rojas
Chambéry, France, 2020